Primary wave of an air-water mixing layer : a numerical study

Cyril Bozonnet

▶ To cite this version:

Cyril Bozonnet. Primary wave of an air-water mixing layer : a numerical study. Materials Science [cond-mat.mtrl-sci]. Université Grenoble Alpes [2020-..], 2021. English. NNT : 2021GRALI056 . tel-03349210

HAL Id: tel-03349210

https://theses.hal.science/tel-03349210v1

Submitted on 20 Sep 2021

Université
Grenoble Alpes

THÈSE

Pour obtenir le grade de

DOCTEUR DE L’UNIVERSITÉ GRENOBLE ALPES

Spécialité : **Mécanique des fluides, Procédés, Énergétique**

Arrêté ministériel : 25 mai 2016

Présentée par

Cyril BOZONNET

Thèse dirigée par **Guillaume BALARAC**, Maître de conférences, Grenoble INP,
et co-dirigée par **Olivier DESJARDINS**, Professor, Cornell University

préparée au sein du **Laboratoire des Écoulements Géophysiques et Industriels (LEGI)**

et au sein du **Computational ThermoFluids Laboratory (CTFLab, Cornell University)**

dans **l'École Doctorale I-MEP2 – Ingénierie – Matériaux, Mécanique, Environnement, Énergétique , Procédés, Production**

Primary wave of an air-water mixing layer: a numerical study

Vague primaire d’une couche de mélange eau-air : une étude numérique

Thèse soutenue publiquement le **22 Juin 2021**,
devant le jury composé de :

M. Stéphane ZALESKI
Professeur des Universités, Université Pierre et Marie Curie, Rapporteur
M. Stéphane VINCENT
Professeur des Universités, Université Paris-Est Marne-la-Vallée, Rapporteur
M. Éric BLAYO
Professeur des Universités, Université Grenoble Alpes, Président du jury
M. Jean-Philippe MATAS
Professeur des Universités, Université Claude Bernard Lyon 1, Examinateur
M. Guillaume BALARAC
Maître de conférences, Grenoble INP, Examinateur, Directeur de thèse
M. Olivier DESJARDINS
Professor, Cornell University, Examinateur, Co-directeur de thèse

Abstract

The shear instability occuring at the interface between a slow water layer and a fast air stream is a complex phenomenon driven by momentum and viscosity differences across the interface, velocity gradients, as well as by injector geometries. Simulating such an instability in the conditions of experiments is numerically challenging and few studies exist in the literature. This work aims at filling a part of this gap by presenting a study of the convergence between two-dimensional simulations, linear theory, and experiments, in regimes where the instability is triggered by confinement, i.e., the finite thicknesses of the gas and liquid streams. Very good agreement between the three approaches is obtained. Moreover, using simulations and linear theory, we explore in details the effects of confinement on the stability of the flow and on the transition between absolute and convective instability regimes, which is shown to depend on the lengthscale of confinement as well as on dynamic pressure ratio. In the absolute regime under study, interfacial wave frequency is found to be inversely proportional to the smallest injector size (liquid or gas). We then study the transition between primary and secondary instability through wave acceleration. In additional, we explore the impact of three-dimensional effects on the flow. Finally, we present the development of an open boundary condition for turbulent multiphase flows and surface waves simulations. Initially thought as a way to improve accuracy and lower needed computational ressources of air-water mixing layer simulations, this work leads to improvements in the use of traction boundary conditions. Particularly, this novel boundary treatment couples Lagrangian traction estimation to backflow stabilization which provides stability, accuracy and non-reflectivity of artificial boundaries.

Remerciements

La formation à la recherche scientifique par la thèse est une expérience unique en son genre, “découverte” en est pour moi le maître mot. Découverte scientifique, bien sûr, par l'apprentissage continu de nouveaux concepts et nouvelles méthodes, puis - toujours trop rarement - par l'examen d'une idée nouvelle nous amenant à une meilleure compréhension du monde qui nous entoure. Découverte de soi-même, surtout, par l'expérience du doute quasi-permanent, de la frustration, de l'angoisse, parfois de la solitude et du désemparement, mais aussi expérience de l'excitation intellectuelle, de la joie de voir des zones d'ombre, petites ou grandes, s'illuminer enfin, et expérience d'une liberté quasi-permanente[1] ! Ma thèse aura, de plus, été marquée par une expérience internationale et multi-culturelle forte. Pour m'avoir permis de réaliser toutes ces découvertes, ainsi que pour leur patience bienveillante et leurs conseils éclairés, j'adresse ma sincère gratitude à Guillaume et Olivier.

Merci à Jean-Philippe Matas et Éric Blayo, le premier pour avoir été un collaborateur passioné et passionant, réactif et bienveillant, du début de ma thèse jusqu'à bien après la soutenance, le second pour m'avoir aiguillé sur les problèmes de condition de sortie et avoir accepté de présider le jury. Merci à Stéphane Zaleski et Stéphane Vincent, pour avoir accepté de rapporter sur mon manuscrit et pour leurs avis positifs qui m'ont permis d'effacer quelques doutes.

Merci à l'équipe MoST et aux collègues de Cornell pour leur solidarité, leur esprit d'équipe, pour les croissants et les troisièmes mi-temps.

La thèse n'étant pas le centre exclusif de la vie d'un thésard (et oui !), merci enfin aux amis musiciens, aux amis tout court, aux amours et à ma famille pour tout ce qu'ils m'ont donné au cours des dernières années.

Cyril

---

[1] Pour Descartes, la liberté de l'esprit est un fait attesté par notre capacité à douter ! [Descartes, *Les principes de la philosophie*]

Contents

Chapter 1

Fundamentals

1.1 Atomization: why and how?

Atomization is the process in which one wants to separate a bulk in a collection of small particles, or, in the context of liquid atomization, to separate a bulk of liquid into a cloud of droplets, or spray. Liquid sprays play a key role in many environmental flows (e.g., breaking waves, waterfall mists), engineering devices (e.g., food processing, coating, printing, cooling, fire safety, crop spraying), or everyday life (e.g., shower heads, body sprays). Controlling spray quality, i.e., controlling drop sizes and their spatial repartition is essential for many industrial applications.

In crop spraying, one need to avoid small droplets as they may be more sensible to meteorologial conditions and drift too far away, thus spreading chemicals away from their destination. In metalurgical processes, liquid sprays may be used to cool down liquid metal, and drop sizes must be controlled to ensure homogenous cooling and desired heat and mass transfer. In combustion devices, liquid fuel must be turned into the finest spray as possible, i.e., into the smallest droplets, as fuel combustion efficiency will be maximized by a high surface to volume ratio. In this last field of application, controlling spray quality has a direct impact on fuel consumption and pollutants emissions.

Separating a bulk of liquid into a cloud of droplets involves creating surface area, thus surface energy, as one can define the surface energy, E_S, as $E_S = \sigma S$, with σ, in $[N/m]$ or $[J/m^2]$, a material property called surface tension and S, the surface of the liquid parcel. E_S is also called the surface *in excess* energy as it results from an interfacial thermodynamic desequelibrium. As mechanical systems tend to minimize their total energy, at constant volume, liquid parcels will take a spherical shape, as it minimizes surface area. Thus, spray creation involves the injection of a sufficient

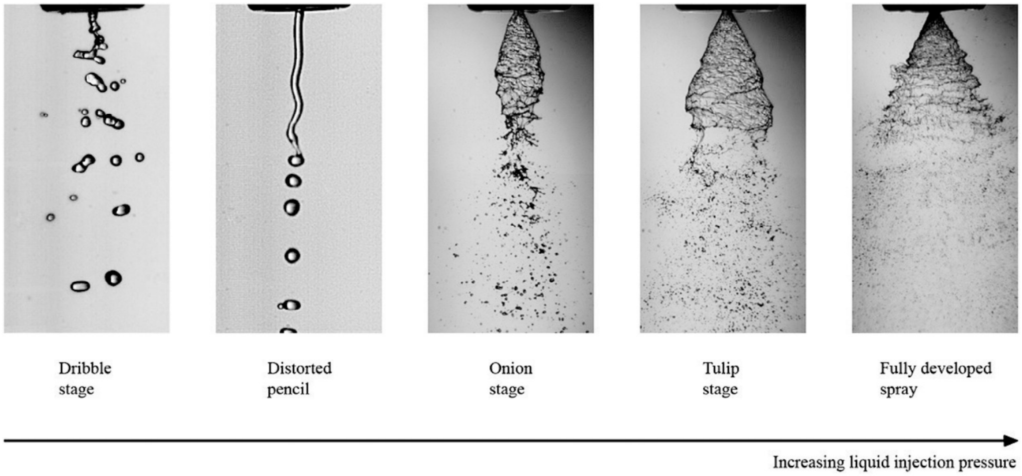

Fig. 1.1 – Photographs illustrating the effect of liquid pressure injection on a swirl atomizer, extracted from Lefebvre (1989).

amount of energy in order to induce the break up of the liquid into a large number of small droplets. The different methods of atomization correspond to different ways to inject this energy, see Lefebvre (1989) for an extensive review. We hereafter briefly present two ways to transform a liquid bulk into a spray.

Pressure atomizers

When a liquid is discharged through a small aperture under high applied pressure, pressure energy is converted into kinetic energy. Under a succesion of interfacial instabilities, kinetic energy will be progressively transformed into surface energy, thus resulting in droplets generation. Increasing or decreasing liquid injection pressure has an effect on the resulting spray, as shown on figure 1.1 for the case of a swirl pressure injector, i.e., when liquid is discharging into the gaseous atmosphere with a non-zero tangential velocity. For low injection pressure (left picture of figure 1.1), the flow is somehow similar to a dripping faucet: a succesion of large drops. For high injection pressure (right picture of figure 1.1), the liquid expands from the nozzle into a conical wavy liquid sheet that progressively transforms into a cloud of droplets.

Because of the complex, random nature of atomization process, many characteristics of the flow, from injection pressure effect to droplets clustering further downstream, need to be studied and understood in order to ensure maximal control of the process, as summarized on figure 1.2.

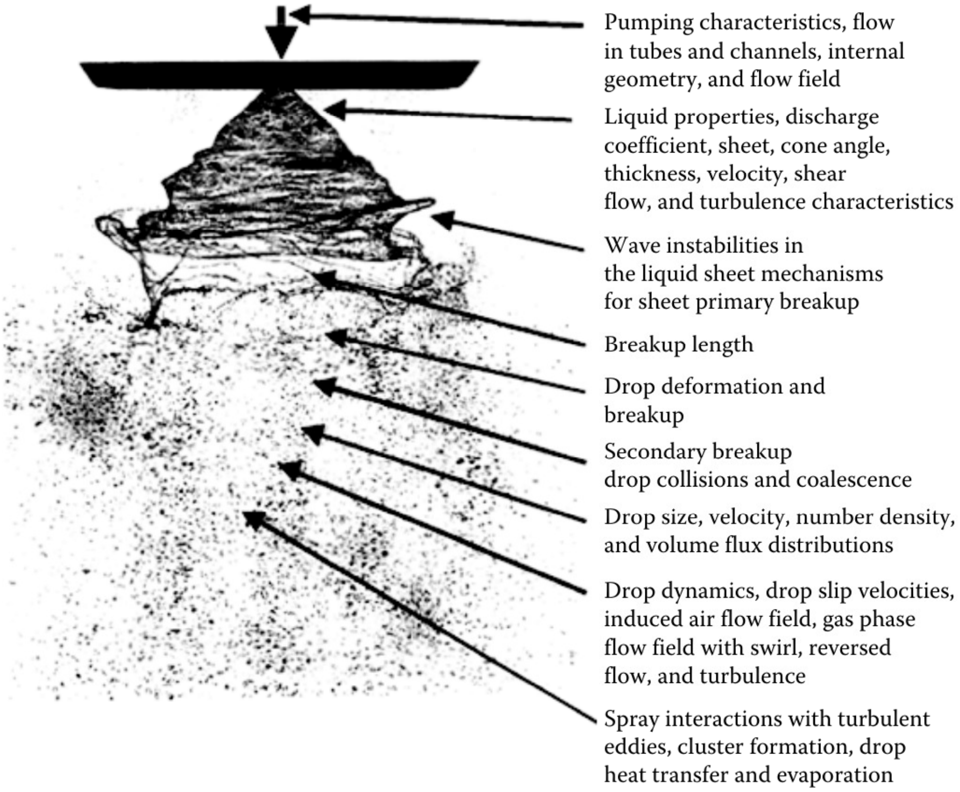

Fig. 1.2 – Illustration of the many features that need to be characterized and understood in order to control spray formation, extracted from Bachalo (2000).

Airblast atomizers

Another way to inject the energy needed to create a spray is to inject it via a medium other than the liquid. Namely, one can use a very high speed gas that will transfer its energy to the liquid phase and induce its deformations and break-up into droplets. Contrary to a pressure atomizer, such device does not require to operate under high pressure conditions which is why they are commonly used in aircraft propulsion systems. A classic configuration corresponds to the case of a cylindrical slow liquid jet surrounded by a fast annular air stream. Another configuration, called *prefilming atomizer*, corresponds to a case where the liquid is first spread onto a solid plate and then exposed to the fast gas stream. Increasing gas velocity will have an effect on the resulting spray, as illustrated on figure 1.3. When increasing gas velocity one can see that more and more small droplets are created downstream of the injector. One can also see, even for high gas velocity figure 1.3d), the detachment

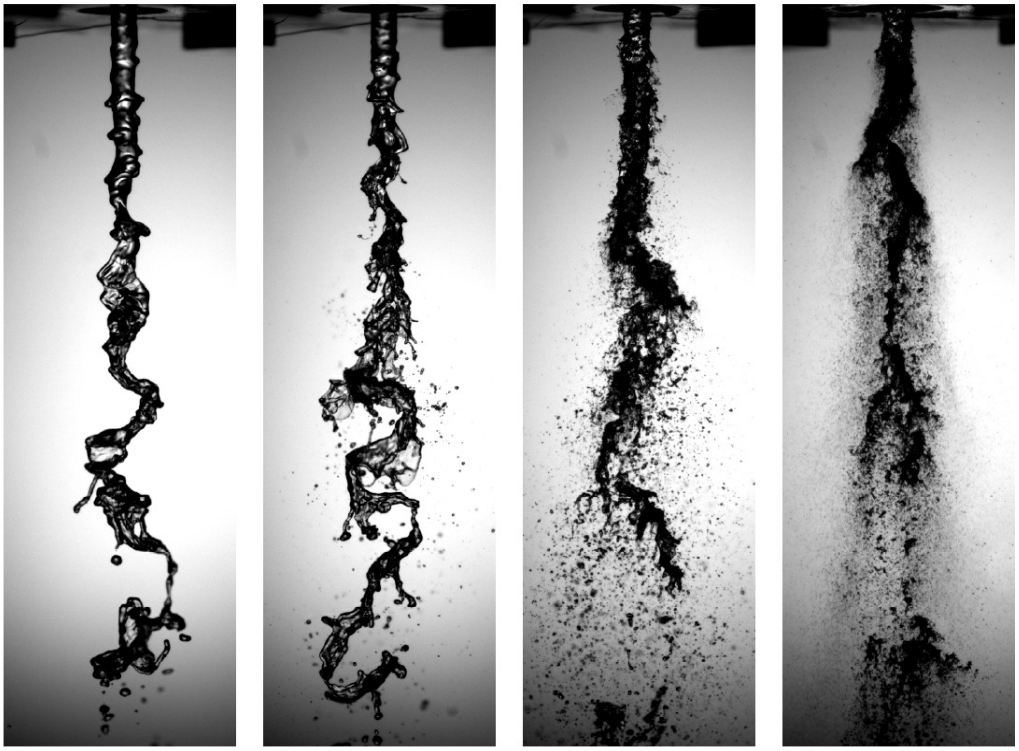

(a) $U_G = 30{,}8$ m/s (b) $U_G = 40$ m/s (c) $U_G = 70$ m/s (d) $U_G = 130$ m/s

Fig. 1.3 – Photographs illustrating the effect of gas velocity, U_G, at fixed liquid velocity, $U_l = 1.41$m/s, extracted from Delon (2016).

of large liquid structures into the downstream part of the spray, which must be avoided in combustion applications. This demonstrates that increasing gas velocity, therefore increasing kinetic energy injection, is not necessarily the only key to a fine spray. Again, the complexity of the phenomena shows that many elements need to be characterized in order to obtain a good understanding and control of spray creation, from axisymmetric wave creation near the injector (figure 1.3a), creation of thin films (middle part of figure 1.3b), to interactions between small droplets and large liquid parcels (downstream part of figure 1.3d).

In the following, we exclusively focus to what is happening in the *primary atomization* step, i.e., when liquid structures are still connected to the injector. What happens during *secondary atomization*, i.e., droplets-turbulence interactions or droplets clustering, is not in the scope of this work. In the next section, we qualitatively detail the different events leading to droplet creations in the context of airblast atomization.

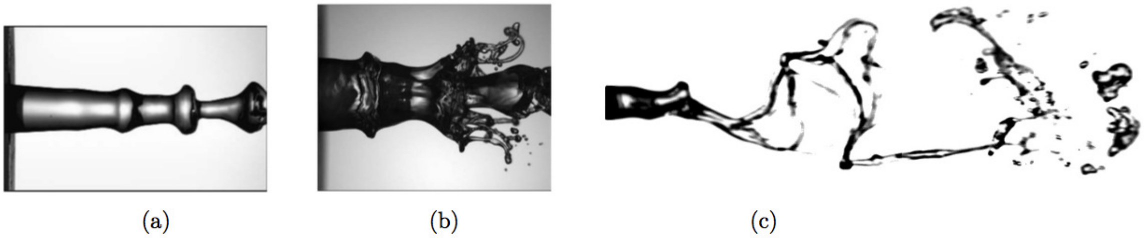
(a) (b) (c)

Fig. 1.4 – Instability cascade in a co-axial airblast atomizer. a) primary wave, b) ligaments ejection and droplets formations, c) flapping instability. a) and b) extracted from Marmottant and Villermaux (2004), c) extracted from Delon (2016).

Instability cascade in airblast atomizers

The succesion of events leading to droplet creation is often described using the concept of "instability cascade" (Marmottant and Villermaux, 2004), and is illustrated on figure 1.4. The different steps are usually refered to as: 1/ wave formation (or primary instability, see figure 1.4a), 2/ ligaments ejection (or secondary instability, see figure 1.4b), 3/ droplets creation. As seen on figure 1.4c, under some conditions, a large scale instability, called flapping instability, can lead to the creation of large liquid structures. We hereafter qualitatively describe the phenomena at play behind each step.

Wave formation

Two initially parallel streams (with zero viscosity and same densities) having different velocities are naturally unstable: this is the Kelvin-Helmholtz instability (see Charru (2012) for a review of hydrodynamic instabilities, including Kelvin-Helmholtz instability). This is the mechanism at play behind primary wave formation. In case of airblast atomization, the conditions for instability, its nature and characteristics, mains subjects of this thesis, are very complex and will be detailed in section 1.3.

Ligaments ejection

The primary wave is growing under linear, then non-linear, mechanisms until forming a thin liquid sheet that can undergo a secondary instability. A widely admitted mechanism for ligaments ejection is through a Rayleigh-Taylor instability (Varga et al., 2003). The thin formed liquid sheet is exposed to the high speed gas jet and becomes subject to an axial acceleration induced by aerodynamic effects. This acceleration from the heavy to the light phase can lead to the amplification of perturbations, similarly to a classical gravitational Rayleigh-Taylor instability (see Charru (2012)), and to wave crest deformation into liquid ligaments that are further stretched by the gas stream, see figure 1.4b). Some models for this acceleration have been proposed, based on aerodynamic forces balance (Varga et al., 2003; Marmottant and Villermaux, 2004), and are further included in theoretical models predicting the growth of a Rayleigh-Taylor instability. These models agree generally well with experimental measurements of transverse wavelength (Varga et al., 2003; Marmottant and Villermaux, 2004; Ben Rayana, 2007), except with the most recent experiments of Marty (2015). Note that transverse wavelength is often deduced from mean droplet size, as a Rayleigh-Plateau droplet formation mechanism involves a proportionallity between mean droplet and ligament sizes, with the latters proportionals to transverse wavelength (Marmottant and Villermaux, 2004).

On the other hand, some mechansims for ligaments ejection have been proposed based on hole formations. Indeed, it has been seen through experiments (Raynal, 1997; Villermaux, 2020) and simulations (Ling et al., 2017; Zandian et al., 2017), that when the liquid sheet becomes very thin, some holes may appear in this thin film and may further expand until inducing the rutpure of the wave crest into ligaments. Interactions between vorticity dynamics and ligaments have been studied by Zandian et al. (2019) in a configuration similar to a pressure injector (low external gas velocity). Other instabilities may play a role, see (Villermaux, 2020) for a review.

Droplets creation

Once ligaments are created, the mechanism by which droplets are created is widely accepted to be due to a Rayleigh-Plateau instability. This instability involves the creation of droplets from a ligament in order to minimize surface area, therefore surface energy (Charru, 2012). Surface tension is the destabilizing mechanism whereas inertia is stabilizing. The competition between both effects is known to be the source of the dripping/jetting transition observed for capillary jets (Clanet and Lasheras, 1999). As said previously, this mechanism involves a proportionality between ligament size and mean droplet size, which has been validated experimentally (Marmottant and Villermaux, 2004). The final drop size distribution is the result of many complex interactions between waves and ligaments, secondary break-up, disparities in ligament sizes, and other mechanisms of fragmentation, see Villermaux (2007) for a review.

Among these other mechanisms of fragmentation, one can cite the bag-breakup phenomena, which is usually occuring during secondary atomization at low gas velocity (Zhao et al., 2011). As observed on figure 1.3b), some liquid membranes can be formed by the blowing of the gas into the thin liquid sheet formed by primary wave growth. These membranes can further explode into a large collection of small droplets. This mechanism can thus also be part of the primary atomization mechanisms. Note that this mechanism is also involved in drop size distribution of raindrops (Villermaux and Bossa, 2009).

Another mechanism for droplet creation has been identified on prefilming airblast atomizers by Jerome et al. (2013), and is called the "droplet catapulting" mechanism. This mechanism, due to interactions between a wave and vortices detachment in its wake, induces a flapping motion of the ligament that can result in droplets ejection with large angle, as observed in the experiments of Raynal (1997).

Flapping instability

As shown on figure 1.3, in the downstream part of the spray, a large scale instability can appear and induce a global flapping motion of the liquid jet (Chigier and Farago, 1992), or the liquid sheet in case of plane jet (Lozano and Barreras, 2001). This flapping motion can result in the detachment of large liquid structures that can deteriorate the quality of the spray, thus deteriorate combustion efficiency in fuel injection systems. Recent experiments on a co-axial configuration show that two flapping regimes can be distinguished (Delon et al., 2018). In the first one, flapping is triggered by the wake downstream of nonaxisymmetric modes of the shear instability. In this regime, flapping frequency closely follows primary wave frequency (even though systematically smaller). In the second flapping regime, flapping frequency is not anymore connected to primary wave frequency.

Interactions between coherent turbulent structures and flapping motion have been evidenced (López-Pagés et al., 2004; Odier et al., 2015, 2018). In case of co-axial jets, by analogy with vortex rings pairing in single phase round jet (da Silva and Métais, 2002b), Odier et al. (2018) observe the flapping to be triggered by interfacial wave pairing.

1.2 Survival kit of linear stability analysis

Before focusing our study on primary wave creation, we provide the reader with a few fundamental notions of stability analysis. Indeed, the parallel, or quasi-parallel, nature of the flow before wave creation makes it an ideal framework for theoretical approaches like linear stability analysis. For a larger introduction to stability analysis we refer the reader to Charru (2012); Drazin and Reid (2004); Chandrasekhar (1961).

Objectives of stability analysis

The stability of a given system is refering to its response to a perturbation: if this perturbation is damped, the system is stable, if the perturbation is amplified, the system is unstable. In fluid mechanics the system is called a basic state. It represents a configuration where the variables of the problem (velocity, presure, temperature and density fields) satisfy the usual conservation equations (mass, momentum, energy) and boundary conditions. Stability studies are answering to the following questions:

- Is a basic state stable or unstable to a given perturbation?
- If it's unstable:
    - Under which conditions is it unstable?
    - Is there a threshold for instability?
    - What are the physical mechanisms behind instability?
    - At which rate does the pertubation grow?

Impulse response

In order to give some fundamentals notions of stability, we start by considering the response of a given one-dimensional linear system to an impulse perturbation, $S(x,t)$, of the form

$$S(x,t) = \delta(x)\delta(t), \tag{1.1}$$

where x is the spatial coordinate and t, the time. $\delta(x)$ and $\delta(t)$ are the impulse perturbations (Dirac functions) at $x = 0$ and $t = 0$, respectively. Depending on the asymptotic value of the impulse response, $G(x,t)$ (Green function), different behaviours are possible (see figure 1.5). If

$$\lim_{t\to\infty} G(x,t) = 0, \text{ along all lines } x/t = \text{cste}, \tag{1.2}$$

the perturbation is damped and the basic state is stable (figure 1.5a). If

$$\lim_{t\to\infty} G(x,t) = \infty, \text{ along at least one line } x/t = \text{cste}, \tag{1.3}$$

the perturbation is amplified and the basic state is unstable. Two possibilities are then appearing. If

$$\lim_{t\to\infty} G(x,t) = 0, \text{ along the line } x/t = 0, \tag{1.4}$$

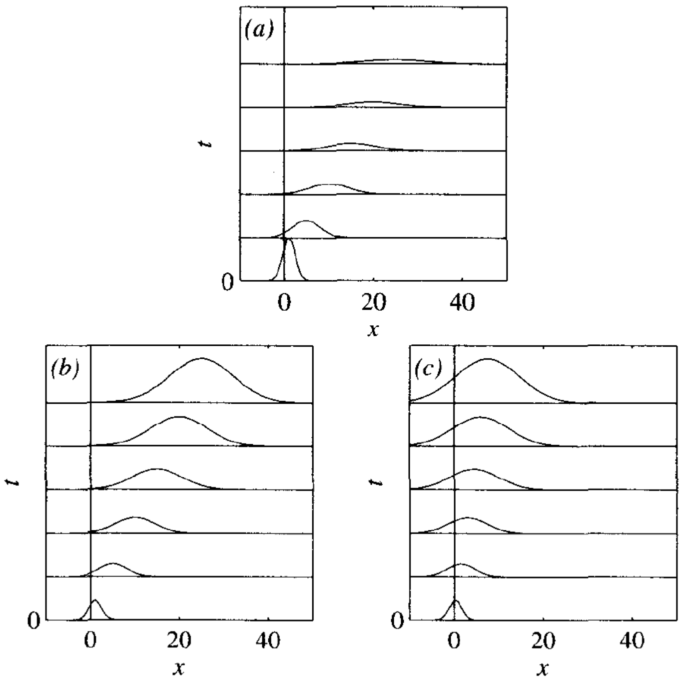

Fig. 1.5 – Impulse response of a given system leading to three different asymptotical behaviours: a) stable, b) convectively unstable, c) absolutely unstable. Extracted from Charru (2012).

the basic state is convectively unstable: the perturbation is amplified and convected away from where it has been generated (figure 1.5b). If

$$\lim_{t\to\infty} G(x,t) = \infty, \text{ along the line } x/t = 0, \tag{1.5}$$

the basic state is absolutely unstable: the perturbation is growing where it has been generated (figure 1.5c). This distinction between convectively and absolutely unstable basic state only makes sense in case of open flows. In closed flows a perturbation will be forced to pass where it has been generated. This first study also shows a difference between convective and absolute instability: without continuous forcing, the impulse response of a convective instability is decaying to zero (along the line $x/t = 0$), which means that this system behaves as a “noise amplificator”. On the other hand, an absolute instability will exhibit an intrisic dynamic and behaves as an “oscillator”. These notions are more widely covered in Huerre and Monkewitz (1990).

Local linear stability theory

The stability properties of a given basic state can be studied mathematically using linear stability analysis. The variables of the problem are described with the following expressions (neglecting thermal effects and density variations)

$$\mathbf{u} = \mathbf{u_0} + \mathbf{u}', \tag{1.6}$$

$$p = p_0 + p', \tag{1.7}$$

where $\mathbf{u_0}$ and p_0 are the velocity vector and pressure of the basic state, respectively, $\mathbf{u}'$ and p', the velocity vector pertubation and pressure perturbation, respectively, and $\mathbf{u}$ and p the velocity vector and pressure fields, respectively. Note that we are only considering two-dimensional steady base flows and that we do not consider the spatial evolution of the base flow in more than one direction, i.e., the analysis is local and stricly parallel. Velocity and pressure fields are expressed in the coordinates system and are then injected in the conservation equations (mass, momentum, energy) and boundary conditions. This will result in a coupled system of non-linear equations. For small perturbations, the system can be linearized around the basic state, i.e., we neglect the products of perturbations. We will then get a system of linearized equations, with constant coefficients.

We assume that the coordinate system is Cartesian and the base flow is only varying with the vertical coordinate, y, i.e., $\mathbf{u_0} = (u_0(y), 0, 0)$ and $p_0 = p_0(y)$. The linearized system admits solutions (for perturbations) in normal modes, which could be treated separately because each of them satisfies the system of equations, in the form

$$(u', v', w', p') = (\hat{u}, \hat{v}, \hat{w}, \hat{p})(k, y, \omega)e^{i(kx-\omega t)}, \tag{1.8}$$

where $(\hat{u}, \hat{v}, \hat{w}, \hat{p})$ are the eigenfunctions, ω and k are the complex frequency and complex wavenumber, respectively. Frequency and wavenumber can be decomposed in real and complex parts,

$$\omega = \omega_r + i\omega_i, \tag{1.9}$$

$$k = k_r + ik_i, \tag{1.10}$$

where $k_r = 2\pi/\lambda$ is the wavenumber, with λ the wavelength, k_i is the spatial growthrate, $\omega_r = 2\pi f$ is the pulsation, with f the frequency, ω_i is the temporal growth rate.

Introduction of these perturbations in the linearized system of equations and associated boundary conditions will lead to a dispersion relation of the form

$$D(\omega, k) = 0. \tag{1.11}$$

It will be solved differently depending on the nature of k and ω:

- temporal resolution: considering a real wavenumber ($k = k_r$), we are looking for the temporal branches of the instability, i.e., we want to find the values of the complex frequency $\omega = \omega_r + i\omega_i$ as a function of k_r,

- spatial resolution: considering a real frequency ($\omega = \omega_r$), we are looking for the spatial branches of the instability, i.e., we want to find thes value of the complex wavenumber $k = k_r + ik_i$ as a function of ω_r,

- spatio-temporal resolution: we are considering complex frequency as well as complex wavenumber. As we consider both spatial and temporal evolution of perturbations, this approach allows to distinguish between convective and absolute instabilities.

With wave-like perturbations, it is also useful to consider the phase velocity of a wave,

$$v_p = \frac{\omega_r}{k_r}, \tag{1.12}$$

and the group velocity of a wave paquet,

$$v_g = \frac{\partial \omega_r}{\partial k_r}. \tag{1.13}$$

Conditions for convective and absolute instabilities

Two types of instability have been described previously using the impulse response of a given system. We will now describe the conditions for these instabilities to occur using the elements introduced with linear stability analysis. Introducing (1.9) and (1.10) in (1.8), we get, for the axial velocity perturbation,

$$u' = \hat{u}(k, y, \omega) e^{i(k_r x - \omega_r t)} e^{\omega_i t - k_i x}. \tag{1.14}$$

In the previous equation, the exponential that contains the frequency and wavenumber real parts is related to the spatio-temporal propagation of the wave. The other exponential contains the informations about the spatio-temporal amplification of the wave. It simply follows that the conditions for instability of a base flow will depend on the type of resolution:

- for a temporal resolution ($k_i = 0$), the condition for instability is $\omega_i > 0$,

- for a spatial resolution ($\omega_i = 0$), the condition for instability is $k_i < 0$.

In a spatio-temporal resolution, the complex nature of wavenumber and frequency allows to distinguish between convective and absolute instabilities. The criteria introduced by Briggs (1964) are used to reveal absolute mechanisms:

- A "pinching" point is occuring between two spatial branches. These two spatial branches must lie in two opposite half-planes of the (k_r,k_i) plane when ω_i is large.
- The group velocity at the pinching point is equal to zero.
- The imaginary part of the frequency must be positive at the pinching point. It is often denoted ω_{0i} and called absolute growth rate.

The first and third criterions are represented on figure 1.6. L and F are the integration paths in the complex ω and k planes, respectively. As the path L is going down, the shape of the mode $\omega(k)$ is modified and the path F is deformed. Then a singularity can occur with the pinching of two spatial branches. The group velocity at this point tends to zero and if the absolute growth rate is positive the instability is absolute. When there is no pinching point, the criterions on the sign of ω_i and k_i are applied to detect a convective instability. Moreover, in convective as well as absolute modes, several wavenumbers or frequencies can be unstable. In this case, we use the value of the spatial or temporal growth rates to find the most amplified frequency or wavenumber.

These three criterions can be understood phenomenologically:

- The absolute instability is associated with a mechanism of resonance between two physical phenomena (usually a downstream/upstream resonance), which explains the pinching between two spatial branches, each of them being controlled by a different mechanism. The identification of the mechanisms controlling each branch is usually done by indentifying which parameters of the problem (e.g., flow speed, flow geometry, physical properties) control the position of each branch in the (k_r,k_i) plane.
- As seen previously with the study of the impulse response, an absolute instability is growing where it has been generated. For wavelike perturbations, the group velocity of an absolute instability is thus equal to zero.
- The final condition is that the perturbation will be amplified in time, thus requiring the absolute growth rate to be positive at the pinching point.

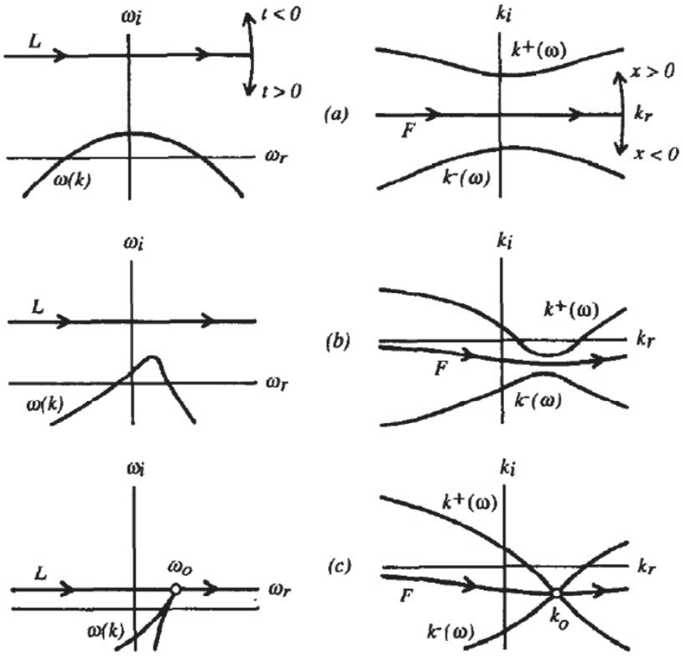

Fig. 1.6 – Mechanism for absolute instability, extracted from Huerre and Monkewitz (1990). As the integration path in complex ω-plane is going down (a), the integration path in complex k-plane and the relation $\omega(k)$ are modified (b), allowing for the emergence of a singularity named “pinching point” (c).

Extensions

The previous description is based on several strong hypothesis that can limit the range of validity of such approach. Here, we briefly describe some more advanced approaches that avoid one or several of the previous hypothesis. Note that, in the rest of the manuscript, we limit ourselves to the stability analysis presented above, but that it is important to keep in mind its limiting hypothesis.

Global linear stability

We assumed previously that the base flow was strictly parallel, therefore that the analysis was local. Taking into account spatial variations of the base flow is possible with two different methods, depending on the degree of variation of the base flow with spatial coordinates. The objective of such analysis is to find informations about the global response of the flow to some pertubations, and particularly to find informations about ω_G, the global resonance complex frequency. The informations we summarize here are extracted from Huerre and Monkewitz (1990) and Juniper et al. (2011).

One first way to obtain informations about global stability properties of a system is through the connection of several local linear analysis. This approach is only valid in case of weakly non-parallel flow (WKBJ hypothesis). The regroupment of informations about local stablity properties will be used to find global stability properties. Particularly, the global mode is deduced from the variation of the local absolute frequency, i.e., the complex part of ω at the pinching point, with downstream distance (see section 4.3 of Juniper et al. (2011) and Chomaz et al. (1991) for an explanation of the method).

The second method, which does not assume a weakly non-parallel behaviour of the flow, is by constructing a global linear stability analysis. Conservation equations are still linearized around the steady base flow, but the latter is fonction of more than one spatial coordinates, and the unsteady perturbations are assumed to be of the form, for example for the axial velocity components of a base flow varying along x and y, $u' = \hat{u}(x, y, \omega_G)e^{(-i\omega_G t)}$. The steady state base flow might be obtained by numerical simulations and the system of linearized equations is solved for ω_G by building a matrix eigenvalue problem (whose size is much bigger than the one obtained for a local analysis). We refer to the section 3 of Juniper et al. (2011) for more detailed explanations.

Once the informations about ω_G are obtained, they can be used to deduce informations on the global stability behaviour of the system. In the case where only one global mode is found, the criterion for global instability is that its imaginary part is positive, i.e.,

$$\omega_{G,i} > 0. \tag{1.15}$$

The distinction between convective and absolute instability can therefore be completed by the distinction between local and global instability. Particularly, a local convective mode will be globally stable, while a local absolute instability is a necessary, but not sufficient, condition for global instability.

An application of such global linear stability analysis can be found in the study of wakes (Monkewitz, 1988; Thiria and Wesfreid, 2007; Juniper et al., 2011). Particularly, the creation of the von Kármán vortex street above a critical Reynolds number is due to the creation of a global mode of instability. Such global mode is expected to contaminate all the flow (see section 3.2 of Huerre and Monkewitz (1990) for a description of stability properties evolution with Reynolds number for a flow around a cylinder).

Inclusion of turbulence

Even though the base flow is steady, one can include into a linear stability analysis the effects of fluctuations in the flow. One way to do so is by increasing viscosity in the turbulent part of the flow in order to account for turbulent diffusion, for example with a turbulent eddy viscosity model (Matas et al., 2015; Jiang and Ling, 2020; Dagaut et al., 2021).

Non-orthogonality, unsteady base flow, uncertainties, non-linearity

The previous approach is also based on several other strong hypothesis, such as orthogonality of perturbations, steadiness of base flow, or linearization of governing equations. For an introduction to methods of stability analysis that tackle one, or several, of these hypothesis, we refer the reader to the review of Schmid (2007).

1.3 Primary wave of an air-water mixing layer

In this chapter, we exclusively focus on describing the mechanisms behind primary wave formation (axisymmetric or not, depending on the configuration) at the interface between a slow liquid stream and a fast air stream. We show on figure 1.7 another example of such instability for the case of a prefilming airblast atomizer. The parallel, or quasi-parallel, nature of the flow just downstream of the injector makes it an idealized framework for linear stability analysis. As said previously, linear stability analysis (also refered to as LSA in the following) allows a comprehension of the mechanisms driving the instability. In the following we mainly focus on the comparison between experimental results and LSA in order to understand the mechanisms driving wave formation in airblast atomization. One interesting point of the comparison is to follow the evolution of base flows as well as methods of resolution, as we also describe in the following.

Comparison between inviscid studies and experiments

The instability occuring at the interface between two layer of fluids with different velocities is known as the shear instability. It has first been studied by Helmholtz (1868), with a localized perturbation, and by Kelvin (1871), with wave-like perturbations, both with a continuous density across the two phases. This instability is thus known as the Kelvin-Helmholtz instability and the inviscid mechanism behind its occurence in this configuration is simple to understand (see figure 1.8). A perturbation, ubiquitous in nature, deforms the interface, leading to the emergence of bumps

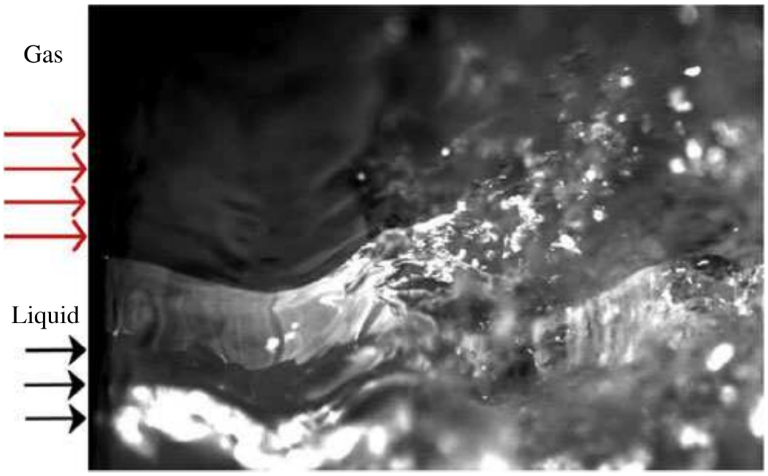

Fig. 1.7 – Primary wave of an air-water mixing layer. Extracted from Fuster et al. (2013).

and hollows. On top of bumps, fluid velocity is increasing while it is decreasing in hollows. This results in a difference of pressure between both fluids that enhances interface deformation.

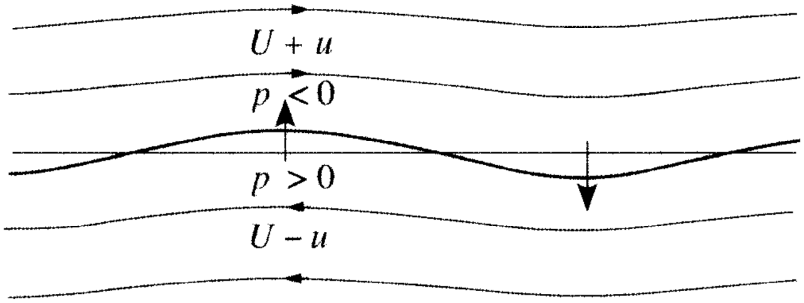

Fig. 1.8 – Inviscid mechanism of Kelvin-Helmholtz instability (extracted from Charru (2012)). U is the mean flow velocity, u and p are the velocity and pressure perturbations, respectively

While in first inviscid studies velocity profiles were discontinuous (figure 1.9a), Rayleigh (1879) adds an union between liquid and gas velocities through a gas vorticity layer thickness δ_g. Chandrasekhar (1961) adds a jump in density across interface. Combining both Chandrasekhar and Rayleigh approaches (resulting in the base flow presented figure 1.9b)), Raynal (1997) uses a linear stability analysis, with a temporal resolution, that is direclty compared to experimental results obtained on the prefilming airblast atomization configuration. The gas vorticity thickness is measured to vary as

$$\delta_g = 6H_g/\sqrt{H_g \rho_g U_g/\mu_g}, \tag{1.16}$$

where H_g, ρ_g and μ_g are the gas stream thickness, density and dynamic viscosity, respectively. One main stability result is the following trend for the most amplified wave frequency,

$$f \sim \frac{\rho_g}{\rho_l}\frac{U_g}{\delta_g} \sim U_g^{3/2}, \tag{1.17}$$

with ρ_l, the liquid density. This scaling is valid in case of large dynamic pressure ratio, i.e., $M = \rho_g U_g^2/\rho_l U_l^2 >> 1$, with U_l the liquid velocity, and ρ_l the liquid density. An experimental observation is that wave velocity is in close agreement with (Dimotakis, 1986),

$$U_D = \frac{\sqrt{\rho_g}.U_g + \sqrt{\rho_l}.U_l}{\sqrt{\rho_g} + \sqrt{\rho_l}}, \tag{1.18}$$

which is the velocity of the moving frame in which liquid and gas dynamic pressure are at equilibrium. Frequency and wavenumber are related through

$$f = U_D/\lambda. \tag{1.19}$$

The relation (1.17) has been validated by many authors, as it is shown in figure 1.10: all measured wave frequencies are following the same trend with gas velocity but pre-factors are not the same. It is interesting to note that the scaling law of equation (1.17) can be recovered, as in Matas (2015), by an energy budget that draws a direct link between Reynolds stress in gas phase and kinetic energy of the perturbation. The later point combined with the fact that wave velocity is well estimated by Dimotakis relation (1.18) are strong arguments in favor of an inviscid mechanism of instability.

The base flow has then been complexified with the addition of a liquid vorticity thickness δ_l (Raynal, 1997), as in figure 1.9c), but it did not improve the comparison between predictions and measurements.

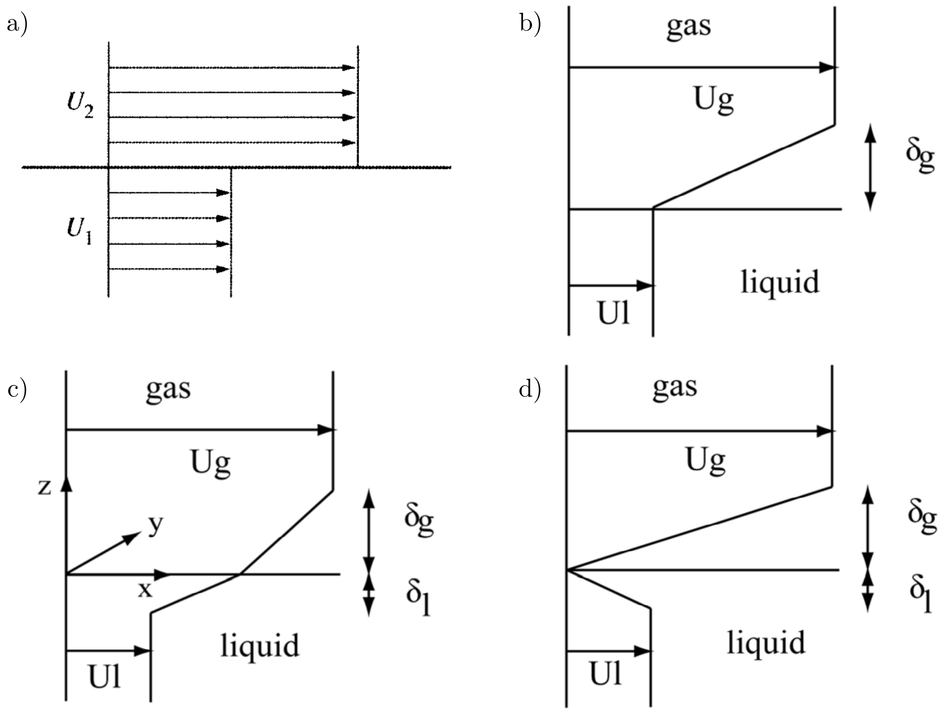

Fig. 1.9 – Velocity profiles used in the different inviscid LSA studies. a) discontinuous profile (Extracted from Charru (2012)). b) introduction of a gas vorticity thickness. c) introduction of a liquid vorticity thickness. d) introduction of a zero interfacial velocity. b-c-d) are extracted from Matas et al. (2011).

One element that was not considered in the analysis so far was the influence of splitter plate between gas and liquid streams on base flow. Indeed, in the wake of the splitter plate, the exact shape and the spatial evolution of the velocity profiles is not known. One can, as shown in figure 1.11, naturally think that sufficiently far away from the splitter plate, the boundary layer on both sides of the liquid/gas interface would have developped up to result in the velocity profile on the right of figure 1.11. Close to the splitter plate, the presence of a zero interfacial velocity also seems natural. Note that, to the best of our knowledge, there is no result in the litterature that presents the evolution of the velocity profiles downstream of a splitter plate in airblast atomization conditions that would confirm, or not, the picture of figure 1.11.

Following the previous remark, the base flow used in local stability analysis has

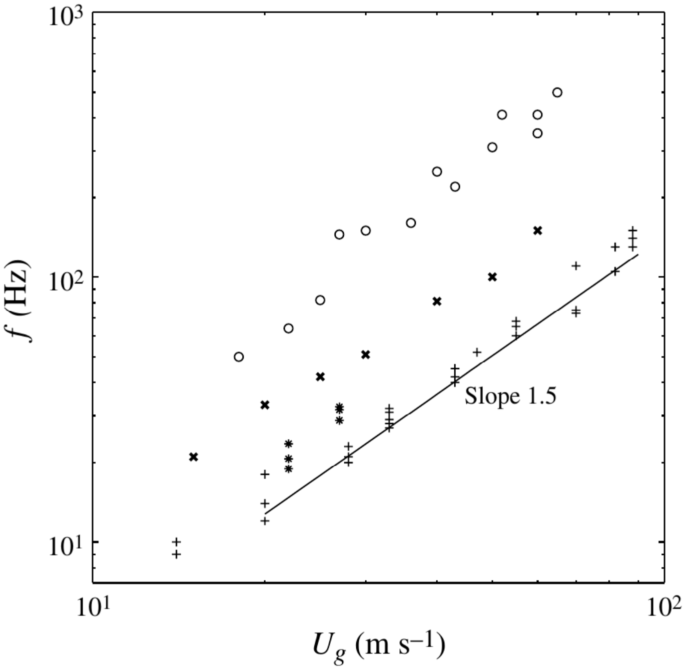

Fig. 1.10 – Comparison of instability fequency for different sets of experiments with $M > 4$. $+$: results of Raynal (1997) ; $\circ$: results of Marmottant and Villermaux (2004) (co-axial configuration) ; $\times$: results of Ben Rayana (2007); $*$: results of Matas et al. (2011). All data are following the same trend with U_g but with differents pre-factors. Figure extracted from Fuster et al. (2013).

thus been modified in Matas et al. (2011) to account for zero interfacial velocity (see figure 1.9d), which improved wave frequency prediction and in particular the prediction of the role of liquid velocity. Marty (2015) shows that this theory finds its limits in the prediction of the role of H_l, the liquid stream thickness, and in the prediction of k_i, the spatial growth rate of the waves. Based on the results of Ben Rayana (2007), it is observed in Matas et al. (2011), that the gas stream thickness, H_g, has no other effect than through its effect on δ_g (Eq. (1.16)).

Inclusion of viscosity

In the previous section, we have presented the inviscid mechanism that leads to Kelvin-Helmhotz instability and how it has been applied to airblast atomization pro-

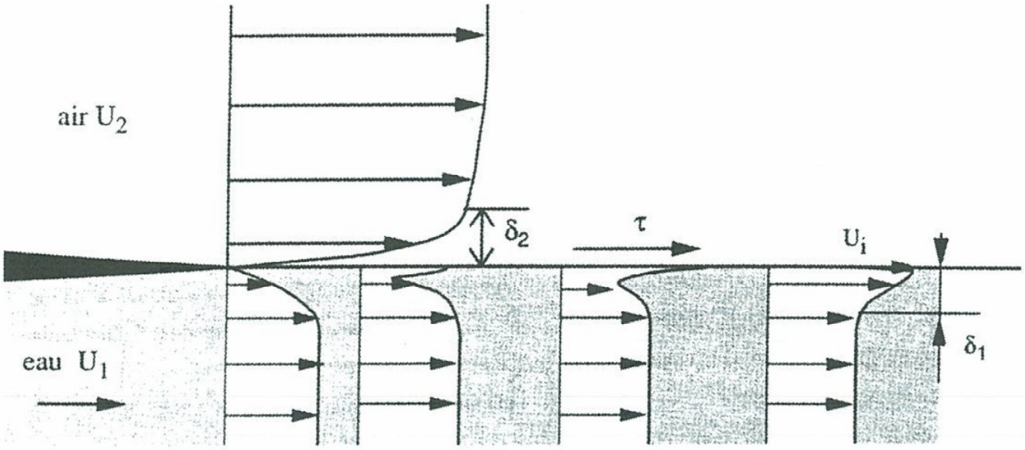

Fig. 1.11 – Representation of the expected spatial variations of the flow in the wake of the splitter plate, from Raynal (1997). It is also shown that the development of the liquid boundary layer is longer than that of the gas.

cess. Another mechanism is likely to appear, driven by viscosity difference between gas and liquid. This mechanism has been evidenced by Yih (1967) and is now usually refered as the "H-mode", following the work of Hooper and Boyd (1983). This instability has been described phenomenologically by Hinch (1984). Starting from the base flow represented in figure 1.12a), a vertical perturbation $y = \eta(x)$ is applied to the interface (see figure 1.12b). At the peak A, the undisturbed velocity (continuous line) of the more viscous fluid (upper fluid in this case) is lower than that of the lower fluid. Thus, due to continuity of tangential velocity, the upper fluid must speed up while the lower fluid must slow down (final velocity profiles are in dashed line in figure 1.12b)

At a fluid-fluid interface, viscosities of both fluids are linked by the continuity of tangential stresses,

$$\mu_1 \left(\frac{\partial u_1}{\partial y} \right) = \mu_2 \left(\frac{\partial u_2}{\partial y} \right), \tag{1.20}$$

where the subscripts refer to both fluids. Then, the magnitude of the speed up, or slow down, in each fluid will depend on the viscosity contrast between both fluids. These disturbances in velocity profiles will result in disturbances in vorticity which are positive in peaks, and negative in throughs, as it is indicated on figure 1.12b). Due to continuity of tangential stresses, vorticity will be larger in the less viscous fluid. Finally, advection of this disturbance vorticity will result in an induced motion of the interface that enhances instability.

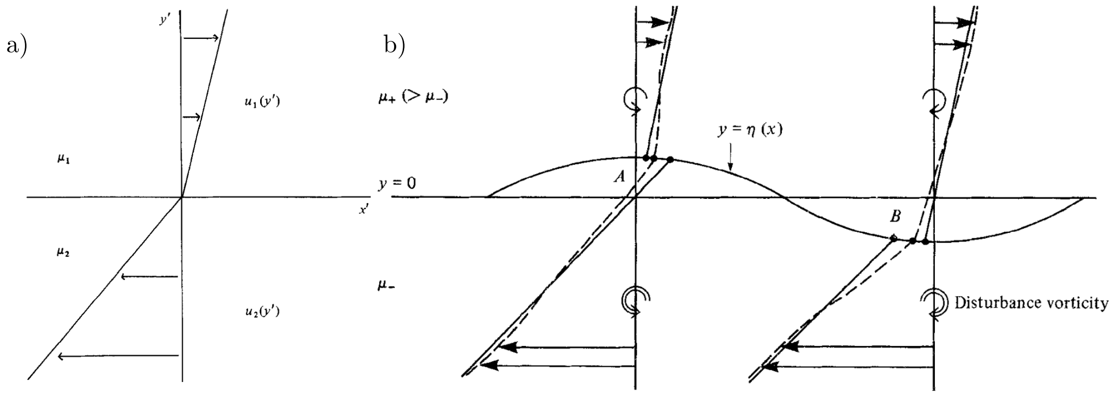

Fig. 1.12 – Viscous instability of the mixing layer. a) : base flow profile (from Hooper and Boyd (1983)), b) description of the mechanism (from Hinch (1984)).

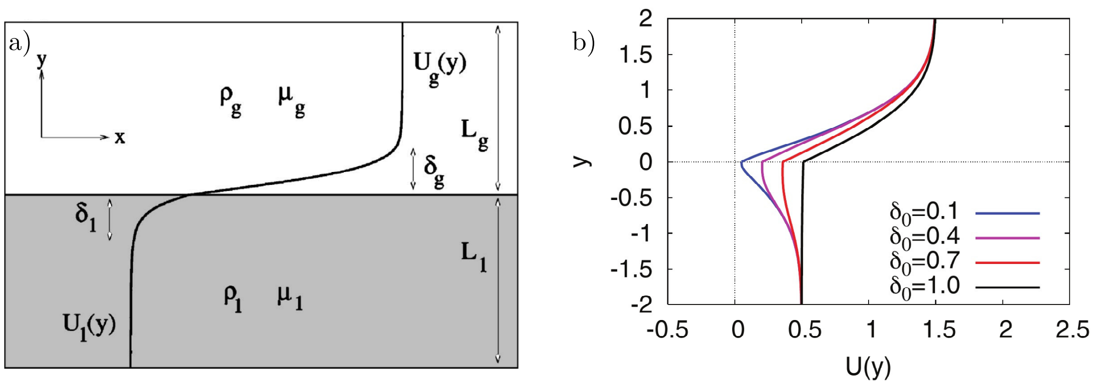

Fig. 1.13 – Base flows used in viscous linear studies. a) base flow used by Boeck and Zaleski (2005). b) base flow used for the spatio-temporal resolution of Otto et al. (2013) in which the interface velocity is controlled by a deficit parameter, δ_0 which is the same as the parameter δ_d we use in the manuscript.

The study of the viscous modes of the planar air-water mixing layer has been performed by Boeck and Zaleski (2005) with a temporal resolution. Their base flow is shown on figure 1.13a). They have shown that the "H-mode" was likely to appear in a configuration and in a range of parameters representative of atomization conditions, and that it was stronger than the inviscid mode (higher growth rate). Even if the predicted growth rate was closer to experimental results than the one obtained with inviscid studies, predicted frequencies strongly overestimate experimental ones.

Transition from convective to absolute instability

It has been shown in previous sections that inviscid studies were able to predict the experimental trend in wave frequencies with the gas velocity and, providing that a zero interfacial velocity is included, predict the role of liquid velocity. Results of the viscous study were surprisingly less satisfying. To solve this paradox, Otto et al. (2013) carried a spatio-temporal analysis, including viscosity. Their base flow is shown on figure 1.13b). It is defined with error-functions as in Boeck and Zaleski (2005), but the interface velocity can be adjusted using a new parameter δ_d to mimic the effect of the splitter plate, similarly to what is shown on figure 1.11. The reduction of the interfacial velocity is also refered to as the inclusion of a velocity deficit. Without deficit, the control parameter δ_d is equal to 1. The interfacial velocity U_i is computed as

$$U_i = \frac{(U_g\mu_g/\delta_g + U_l\mu_l/\delta_l)}{(\mu_l + \mu_g)}\delta_d\delta_l, \tag{1.21}$$

where μ_l is the liquid dynamic viscosity. The expression for U_i ensures equality of tangential stresses whatever the value of δ_d.

Otto et al. (2013) have shown that a transition between convective and absolute instabilities was likely to appear under the experimental conditions of Matas et al. (2011) and that the mechanism behind this absolute instability was due to a pinching between the shear branch and a branch controlled by surface tension. Particularly, the absolute instability is triggered by a reduction of δ_d. This convective/absolute transition has also been seen numerically (at reduced density ratio) to be driven by splitter plate thickness (Fuster et al., 2013). Moreover, an energy budget has shown that the instability was mostly fed by viscous stresses. In case of absolute instability, the agreement with experiments is satisfying, whereas frequency is strongly overestimated when instability is predicted to be convective, which is the case for most of experimental injection conditions.

Even if this study from Otto et al. (2013) has evidenced the fact that an absolute instability could appear in this configuration, and that this transition could be due to the effect of velocity profile variation in splitter plate wake, it does not allow a complete convergence between LSA and measured wave frequencies. It also does not explain the apparent paradox behind the superiority of inviscid theory against viscous theory to predict wave frequency.

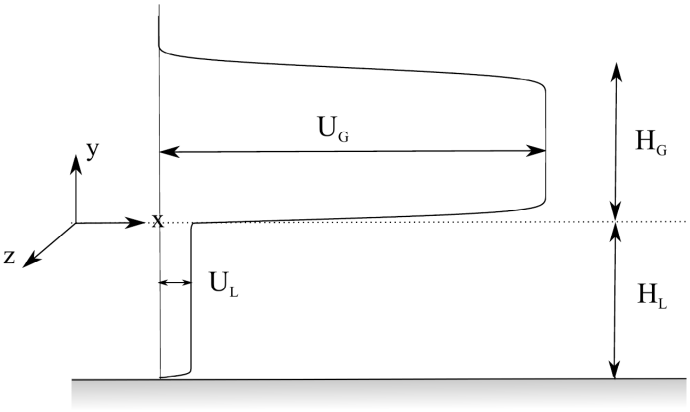

Fig. 1.14 – Base flow used in Matas (2015). Compared to the profiles used in Otto et al. (2013), finite thicknesses of gas and liquid streams (confinement) is taken into account. The interfacial velocity can still be adjusted through a deficit parameter.

As shown for the stability of wakes (Biancofiore et al., 2011), homogeneous mixing layers (Healey, 2009), or jets (Juniper and Candel, 2003), the confinement of a flow can have an effect on its stability, and can favour a transition from convective to absolute instability. By confinement, we refer to the proximity of a wall or the finite thickness of a stream.

Following these studies, Matas (2015) has finally obtained a satisfying agreement between LSA and experimental data using a complete study (with viscosity, surface tension, gravity, control of interface velocity using a deficit parameter) and the introduction of finite width of gas and liquid streams (base flow presented on figure 1.14).

It is evidenced that two different mechanisms of absolute instability and a convective instability were likely to appear for the experimental conditions of Matas et al. (2011). These two types of absolute instability are due to a pinching point between a shear branch, which refers to the branch coming from the upper-half of the complex k-plane, and either a confinement branch, located close to k_i axis and therefore leading to low wavenumber instability, or a surface tension branch, coming from the lower-half of the complex k-plane. This is illustrated in figure 1.15 for a co-axial configuration. For moderate deficit ($\delta_d = 0.3$, $*$), the shear branch deforms until pinching with a confinement branch located close to the k_i axis. For stronger deficit ($\delta_d = 0.1$, $+$), the shear branch deforms until pinching with a surface tension-controlled branch.

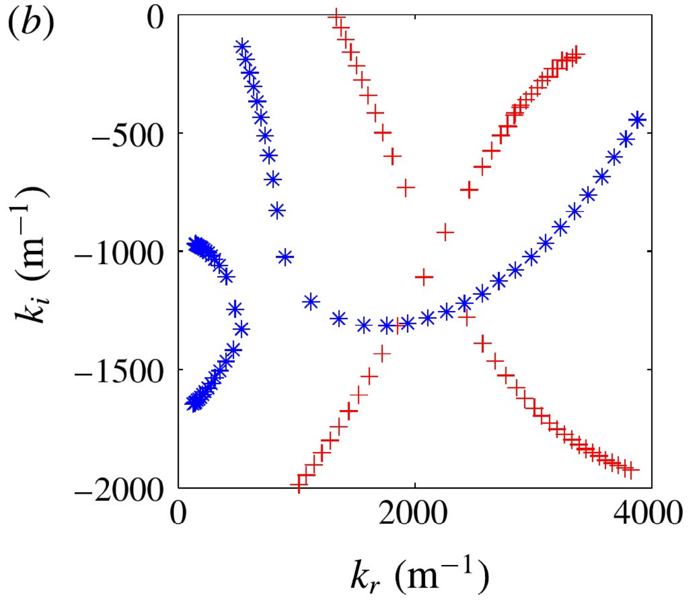

Fig. 1.15 – Illustration of the pinching points leading to absolute instabilities. Co-axial configuration in air-water conditions, with $H_g = H_l = 5$ mm, $U_l = 0.28$ m/s, $U_g = 37$ m/s. $*$: $\delta_d = 0.3, \omega_i = 270\text{s}^{-1}$;$+$: $\delta_d = 0.1, \omega_i = 950\text{s}^{-1}$. Extracted from Matas et al. (2018).

The results of Matas (2015) are presented on figure 1.16. We can see that for the two largest liquid velocities, the agreement betwenn LSA and experiments is satisfying with the results of Otto et al. (2013) ($*$) which corresponds to surface tension driven absolute instability. For lower liquid velocities, the agreement is made with the new results of Matas (2015) ($\circ$ and $\square$), this time predicting an absolute mechanism driven by confinement. The fact that, for the lowest liquid velocities, agreement is found without deficit is also consitent with the idea that a velocity deficit will be longer to resorb at larger liquid velocities, i.e., that δ_d needs to be reduced when increasing U_l, assuming that the picture of figure 1.11 is a correct representation of the flow behind the splitter plate. Note that, the convergence between LSA, with the inclusion of confinement, and experiments on primary wave frequency value has also been obtained for co-axial geometry (Matas et al., 2018). In Matas et al. (2018), the product $\delta_d\delta_l$ for which there is agreement between LSA and experiments is found to be of the order of splitter plate thickness. It is not known yet whether this is significant or just a coincidence.

It should be noted, however, that for an absolute instability the predicted spatial

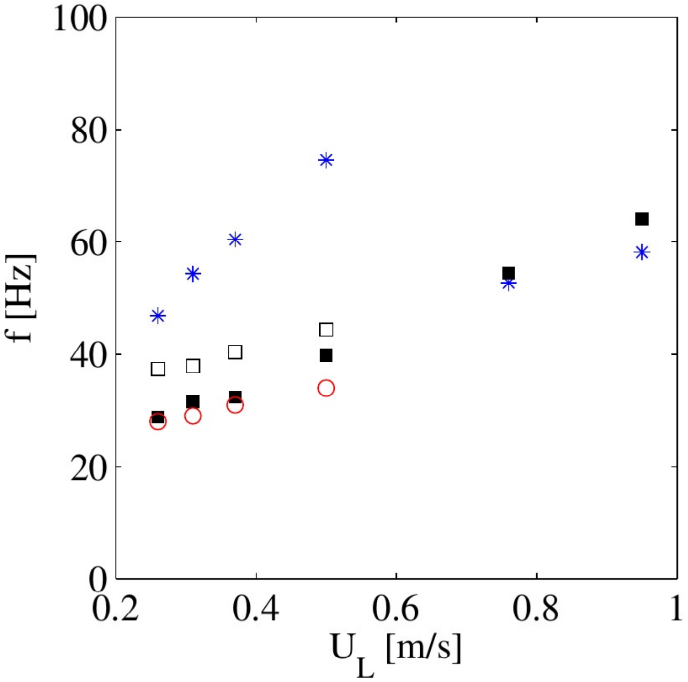

Fig. 1.16 – Convergence between linear stability analysis and experiments for $U_g = 27m/s$, $H_g = H_l = 1$cm. ■ : experimental results Matas et al. (2011), $*$: theoretical results of Otto et al. (2013) with a strong deficit ($\delta_d = 0.1$), ○ : results of Matas (2015) without deficit ($\delta_d = 1$), □ : results of Matas (2015) with a moderate deficit ($\delta_d = 0.5$). Extracted from Matas 2015.

growth rate has no clear meaning for waves traveling downstream of the injector (because the instability is growing where it has been generated, see figure 1.5). The comparison of this quantity between theoretical predictions and experiments did not give satisfaction. The predicted k_i may however still be useful as it provides a length scale for instability in the transverse direction (Juniper et al., 2011).

Most importantly, using an energy budget, the mechanism behind confinement driven absolute instability is shown to be inviscid (fed by gas Reynolds stresses), while for the other cases the mechanisms are viscous, which explains the performance of an invscid study to predict the characteristics of this instability compared to a purely viscous, temporal or spatial, study.

Map of the different regimes

As stated before, the absolute instability can be triggered by confinement or by surface tension. The viscous mechanism is triggered by viscosity differences across interface.

As described in Healey (2007), the mechanism due to confinement is due to the propagation of perturbations in cross-stream direction (figure 1.17a) which, due to finite width of gas/liquid layers, can be reflected (figure 1.17b) and enter in resonance with the shear instability wave.

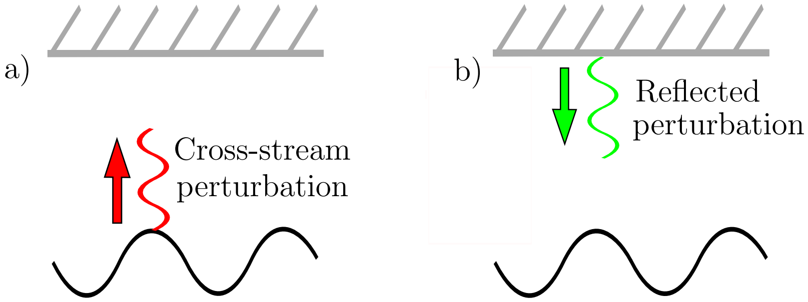

Fig. 1.17 – Mechanism of resonance due to confinement leading to absolute instability.

As said previously, surface tension-induced absolute instability is triggered by a reduction of interfacial velocity. As interpreted in Matas et al. (2018), on co-axial configuration, the condition for this instability to occur is that interface velocity should be low enough so that capillary waves can send information upstream. Therefore, the mechanism of resonance leading to absolute instability is the following: shear instability creates a downstream propagating wave (figure 1.18a) that enters in resonance with the upstream propagating capillary wave generated by the restoring effect of surface tension σ (figure 1.18b).

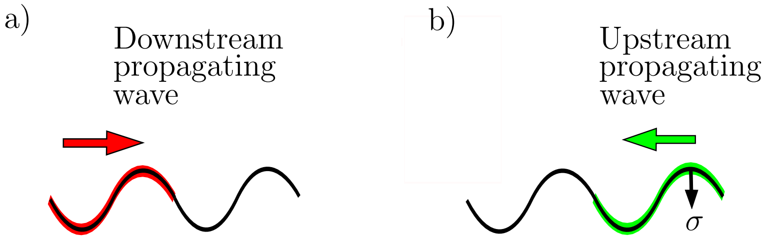

Fig. 1.18 – Mechanism of resonance due to surface tension leading to absolute instability.

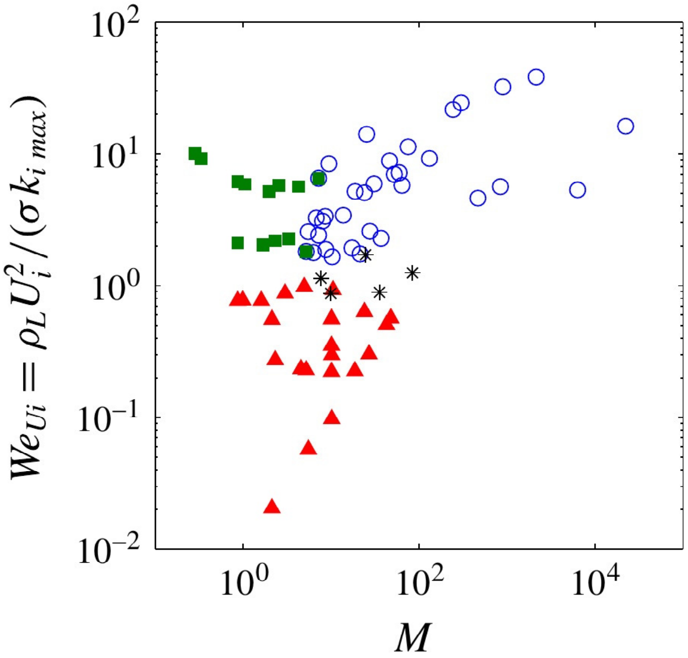

Fig. 1.19 – Map of the different regimes, extracted from Matas et al. (2018). Filled △: surface tension driven absolute instability, filled □: convective viscous mechanism, ○: confinement driven absolute instability, ∗: cases where both absolute regimes have similar absolute growth rates.

Exploring the borders between the different regimes, Matas et al. (2018) finds that borders are well defined on a map constructed with two parameters. The first one is the dynamic pressure ratio M and the second one is $We_{U_i} = \rho_l U_i^2/(\sigma k_{i\ max})$, a liquid Weber number based on the interfacial velocity, U_i, and $k_{i\ max}$, the maximum growth rate of the shear branch. This map is shown on figure 1.19. As soon as We_{U_i} is lower than one, surface tension-induced absolute mode (filled △) is dominating. Above this threshold, the transition between convective (□) and absolute mode due to confinement (○) is driven by M, with the absolute mode dominating for large M.

Impact of gas turbulence intensity

A parameter that is difficult to control in industrial configurations is the turbulent intensity. It is studied in Matas et al. (2015) how it affects instability. Two different techniques are used in order to generate turbulence intensity: with obstacles of different heights placed upstream of the gas nozzle and with an impulse jet introduced upstream of the gas nozzle. This way, results are independent of forcing method. It is found that turbulence intensity has a great impact on instability and that wave frequency is increasing linearly with the level of fluctuations (see figure 1.20).

For a turbulent level of 10%, frequency is doubling compared to a case with almost no turbulent fluctuations. It is also possible to predict this trend using LSA with the introduction of an eddy viscosity model representing the increased level of diffusion with turbulent intensity (symbols $\star$). This effect could be a possible cause for discrepancies between results carried on similar experiments, and for reproductibility issues. Moreover, as turbulence intensity is inducing a decrease of the absolute growth rate at the pinching point, it could also affect the convective/absolute transition and the convective mode may be favoured at high turbulence intensity.

These results are confirmed numerically at moderate density ratio by Jiang and Ling (2020), who also found a linear increase of primary wave frequency with gas turbulence intensity, and found in addition a linear increase of primary wave spatial growth rate with gas turbulence intensity.

Primary wave growth

In the previous section, we explained in details the state of the art of the comparison between LSA and experiments on primary wave frequency. In most of experimental and numerical studies, wave speed is found in close agreement with U_D, Eq. (1.18), thus giving a way to estimate wavelength through Eq. (1.19). So far, we have not described spatio-temporal growth of waves, i.e., what is happening to the wave after its inception, except that, once a liquid sheet is formed, it can undergo different instabilites leading to ligaments or droplets ejections.

The experimental study of waves amplitude in Matas et al. (2011) shows that 3 zones can be distinguished, see figure 1.21a). The first one is a region of "super-exponential" growth in the vicinity of the inlet. The second one, enhanced by red dashed lines, is a region of exponential growth. In the third zone, one can see that wave keep growing with downstream distance but at a lower rate than in the previous zone.

The nature of the first zone is still unclear but certainly linked with the presence of splitter plate. The second zone shows that the instability is following a region of

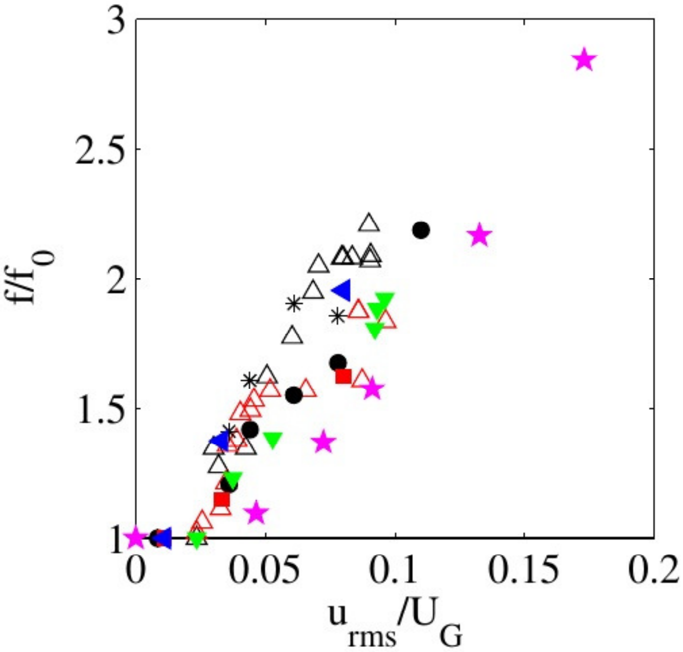

Fig. 1.20 – Effect of turbulence level on primary instability frequency, extracted from Matas et al. (2015). In this case $U_g = 27 m/s$, $U_l = 0.28 m/s$, $H_l = H_g = 1$cm. f_0 is the frequency of the instability with the initial turbulence level. ★ : results of theoretical prediction using an eddy viscosity model. Other symbols are experimental values obtained with different techniques.

exponential growth. For most of the cases under study, the instability is absolute (Matas, 2015). As discussed previously, the predicted value of the spatial growth rate has no clear meaning for an absolute instability, but this exponential growth zone has been found in experiments as well as in numerical simulations (Agbaglah et al., 2017; Ling et al., 2019; Jiang and Ling, 2020). Figure 1.21a) also shows that the width of this zone, and its slope, are greatly affected by variations in gas velocity. Particularly, in Matas et al. (2011) the measured spatial growth rate is shown to be proportional to U_g^2.

Figure 1.21a) is also showing that an increase in gas velocity will favour the entry in third zone: the faster the gas, the closer to the injector is the entry in the third zone. From the measurements of Ben Rayana (2007) (see figure 1.21b), we know that, in this third zone, amplitude is growing linearly with downstream distance, with a pre-factor that depends on injection conditions.

These observations can be linked with the work of Hoepffner et al. (2011) and the

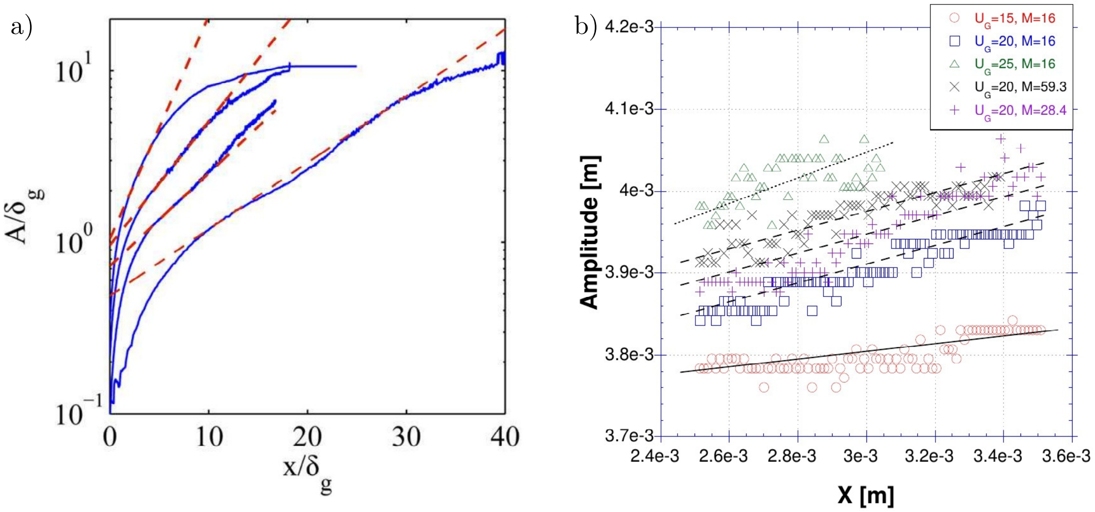

Fig. 1.21 – Wave amplitude variation with downstream distance. a) experimental data of Matas et al. (2011). The red dashed lines enhance the region of exponential growth of the instability. From right to left : $U_g = 12, 17, 22$ and 27m/s. $U_l =$ 0.37m/s. $H_g = H_l =$ 1cm. b) : experimental data of Ben Rayana (2007) for $H_g = H_l =$ 1cm. The black dashed lines enhance the region of linear growth with downstream distance.

study of the growth of a localized disturbance, going back to the original proposition from Helmholtz (1868). It is found that there is a region of algebraic growth of the wave where a self-similar solution can be derived,

$$h \sim \sqrt{\frac{\rho_g}{\rho_l}} U_g t, \tag{1.22}$$

where h is the wave height and t is the time after wave inception. This model has been derived using a balance of pressure between both phases. The mechanism is represented on figure 1.22a). From Bernoulli equation, one can state that pressure drop in gas phase is $P^+ - P^- \sim \rho_g U_g^2$. As the same law is applied in the liquid and if pressure drops in liquid and gas are equal, we also have $P^+ - P^- \sim \rho_l v^2$, where v is the suction velocity at the wave bottom, leading to the relation $v \sim \sqrt{\rho_g/\rho_l} U_g$. If S is the wave surface which has crossed the $y = 0$ limit, with $S = h^2$, we can derive its evolution with a simple time differential equation: $\partial_t S \sim hv$ (the flow is entering from the wave bottom of width h with a velocity v), which, once integrated, results in the

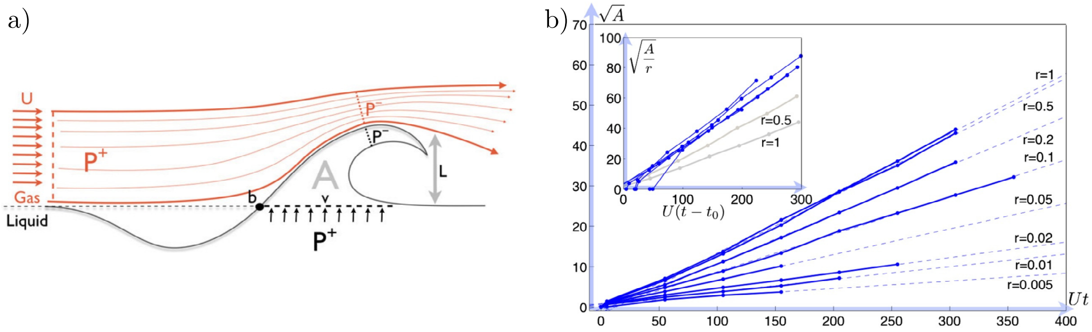

Fig. 1.22 – Algebraic growth of a localized perturbation in Kelvin-Helmholtz instability, figures extracted from Hoepffner et al. (2011). A is the liquid area that has crossed the y=0 limit (refered to as S in the text), L is the wave height ($L = h$) and U is the gas velocity. a): representation of the mechanism behind self-similar solution. b): Numerical results (blue curves) as fonction of the density ratio r ($r = \rho_g/\rho_l$) compared to the self-similar solution (light blue dashed lines). The insert represents the results for $r > 0.1$.

self-similar relation Eq. (1.22). This model is then compared to numerical simulations (figure 1.22b).The agreement is satisfying as soon as density ratio $r = \rho_g/\rho_l$ is lower than 0.1. It should also be noted that this approach is only valid in a range between the scale where viscosity and surface tension have a damping effect, to the scale where gravity will limit wave growth (gravity is not included in Hoepffner et al. (2011) but is included latter in Orazzo and Hoepffner (2012)).

Marty (2015) adapts the self-similar relation Eq. (1.22) to his experimental studies by replacing t with x/U_D. The algebraic growth of waves is validated up to $U_g = 30m/s$. Beyond this value, wave growth is limited by the strong atomization of its crests. However, systematic study of the comparison between the mean ratio h/x and the quantity $\sqrt{\rho_g/\rho_l}U_g/U_D$ shows that some corrections must be introduced on wave velocity to obtain a perfect agreement for all dynamic pressure ratios.

One quantity that has been quantified by many authors is the liquid cone length, L. It corresponds to the length of the cone in which liquid is always present through time. The knowledge of L is useful as it allows locating where liquid is detached from injector. The creation of this cone is not exclusively due to primary wave growth, but is also due to the transformation of the wave into ligaments and droplets. L is found to vary as $L/2H_l = Pref/\sqrt{M}$, with $Pref = 6$ (Raynal, 1997; Ben Rayana, 2007). Simple arguments based on mass conservation and interfacial turbulent stress continuity confirm the model. Marty (2015) finds that the value of $Pref$ is affected by changes in H_l, and that at very low H_l, the dependency in $M^{-1/2}$ is not valid anymore.

1.4 Challenges of atomization simulations

To engineers, atomizing liquid-gas flows present major challenges for control and optimization in comparison to single-phase flows. In addition to the large viscosity and density differences between the two phases, leading to discontinuous pressure and velocity gradients, liquid-gas interface exchanges kinetic energy with the flow via surface tension. Moreover, spray formation involves frequent topology changes, usually through formation and rupture of liquid ligaments and sheets. Downstream of atomization region, the spray is dispersed (and thus simpler to represent, e.g., as a collection of spherical droplets), but it remains dense, strongly coupled to gas phase turbulence, and droplet-droplet interactions are frequent. Such challenges hinder simple mechanistic descriptions of liquid sprays and, since liquid droplets and ligaments form an optically opaque zone that surrounds the liquid core where atomization takes place, experiments have been similarly limited. Consequently, the detailed understanding of liquid atomization physics that would be needed to enable spray control simply does not exist today.

As said in the "Roadmap for the Development of Advanced Atomization and Spraying Technologies" by the Atomization Technology Innovation Consortium (March 2017):

"Numerical simulation and high-fidelity, physics-based models provide far greater detail on the mechanisms that influence the break-up of fluids than traditional process models. Improvements in computational capabilities and broad access to high-performance computing facilities can enable direct numerical simulations of complex engineering spray and atomization processes. Being able to better predict the impacts of variables such as physical property variations, differences in nozzle geometries, and changes in process variables on the characteristics of atomized droplets and spray patterns can enable more advanced process improvements."

Such simulations have to deal with various difficulties. The combination of high density and velocity differences between both phases is known to create numerical difficulties that are difficult to resolve without ensuring consistency between mass and momentum transport (Rudman, 1998; Desjardins and Moureau, 2010; Vaudor et al., 2017). Numerical errors are a natural consequence of the numerous approximations made in order to resolve the equations of motion, and such numerical errors can create erroneous interfacial momentum transport, leading to dramatic interfacial deformations (Pal et al., 2021).

As seen in experimental pictures in section 1.1 and said just before, spray formation involves large interfacial deformations and energy transfer through surface tension. Both elements are challenging to tackle numerically and a perfect solution simply does not exist today. Both elements are tight together, as interfacial deformations will result in interfacial curvature variations, thus modifications in surface tension forces. Numerical inacurracies at any of the different steps will result in erroneous simulation result, or even to numerical instabilities.

Resolving these challenges (need for consistent transports, need to resolve large interfacial deformations, need to compute interfacial curvature), as well as dealing with discontinuous pressure fields, velocity gradients and physical properties, incompressibility condition, turbulence generation, necessity to resolve from the injector to the droplet scale, ... , is an extremely challenging task. Putting aside the question of the cost of the methods (in terms of computational time), simulation capabilities have been recently advanced and these challenges have either been resolved, or are on the edge of being resolved.

The problem of the air-water mixing layer has recently been used as a way to quantitatively validate numerical solvers, against experiments, that managed to combine methods that resolve the previously cited challenges, or at least limit the associated errors (Fuster et al., 2013; Agbaglah et al., 2017; Vaudor et al., 2017). Numerical simulations have also been extensively used on jets or mixing layer problems with relaxed conditions compared to experiments, i.e., with lower density ratios, or lower velocity contrast between phases. These simulations, even though they cannot always be considered as fully realistic, are of great interest for the scientific community and have already provided, and will keep providing, numerous informations on the physic of atomization (airblast or not). For example, the Direct Numerical Simulation (DNS) of a mixing layer at moderate density ratio has been obtained by Ling et al. (2017, 2019), illustrated in figure 1.23a), enlighting the link between interfacial instability development and downstream turbulence, as well as the mechanisms behind spray formation under those conditions.

In addition to references already cited in section 1.3, we give here more details on references that simulated the case of an air-water mixing layer. Bagué et al. (2010) simulate the case of the convective mode and show that very high resolution is needed to correctly capture the sharp variations of eigenfunctions close to the interface. Fuster et al. (2013) simulate a case of absolute instability triggered by surface tension. They obtain a satisfying agreement between their simulation, experimental results and linear stability analysis on the value of wave frequency. Desjardins et al. (2013)

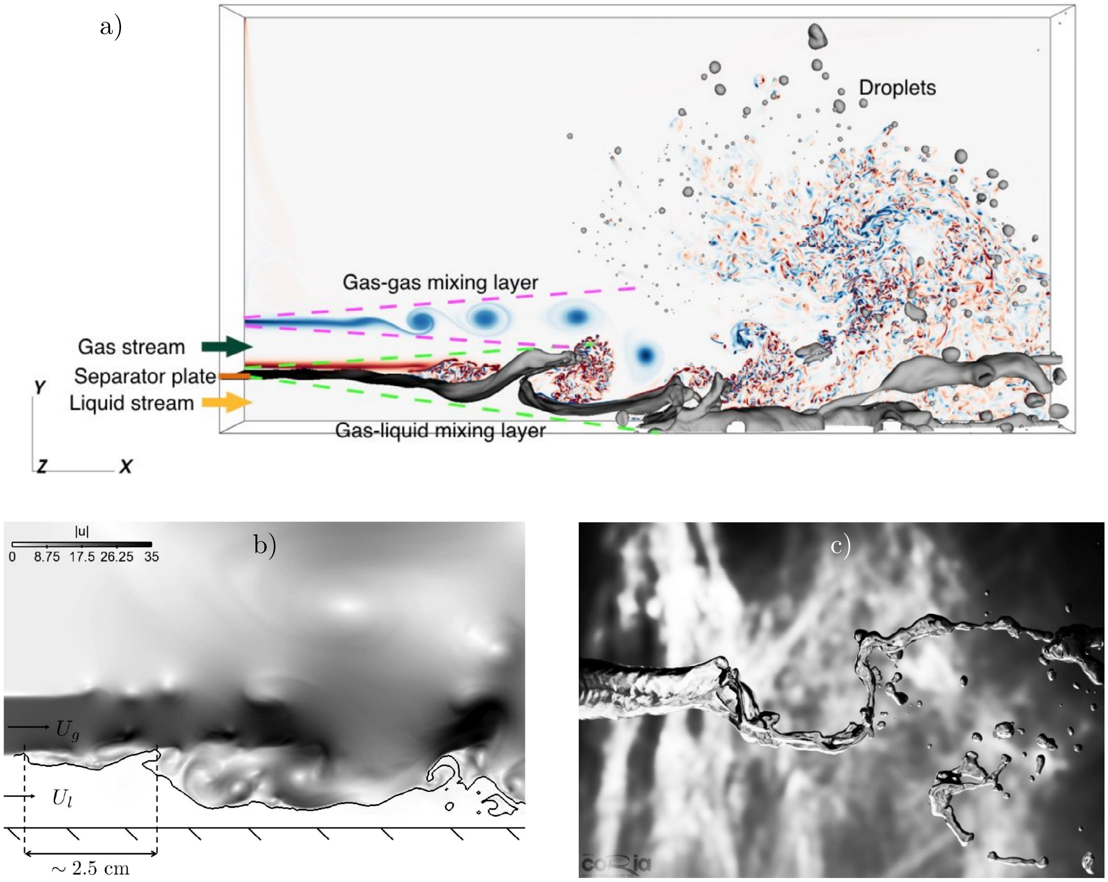

Fig. 1.23 – Illustration of liquid-gas mixing layer simulations. a) DNS at reduced density ratio (Ling et al., 2019). The grey surface is the liquid-gas interface and the background is the z-component of vorticity. b) 2D air-water mixing layer (Desjardins et al., 2013). The black line is the liquid-gas interface and the background is the velocity magnitude. c) Co-axial air-water jet (Vaudor et al., 2017).

simulate an air-water mixing layer, as illustrated in figure 1.23b), and show a good agreement of liquid cone length and wavelength with the experiments of Ben Rayana (2007) for two values of M. Agbaglah et al. (2017) and Chiodi and Desjardins (2017) demonstrate good agreement with experiments on frequency, wave speed, growth rate and liquid cone length for several values of M, in an absolute regime supposed to be driven by surface tension (conditions of Fuster et al. (2013)). They also present the effect of splitter plate angle on flow stability, as well as provide flow statistics in two-dimensions (2D) and three-dimensions (3D). Vaudor et al. (2017) obtain a good agreement with experimental results concerning liquid cone length in prefilming and co-axial configurations, as illustrated in figure 1.23c). In air-water conditions, Fuster et al. (2013); Agbaglah et al. (2017); Vaudor et al. (2017); Desjardins et al. (2013) are including a splitter plate in their configuration. Contact line dynamic occurs at the splitter plate, as revealed by simulations (Fuster et al., 2009), and simulating such process is challenging and expensive.

1.5 Objectives & contents of the manuscript

It follows from previous section that only few studies are providing a comparison of numerical results with linear stability analysis and experiments, including a systematic validation of instability characteristics, i.e., frequency, growth, wave speed, and that the range of resolution needed to accurately simulate an air-water mixing layer is not known. The effect of the confinement on the stability of the flow has been demonstrated theoretically (Matas, 2015) and provides an explanation for the low frequencies observed in the experiments, but it has never been observed numerically.

This thesis aims at filling a part of this gap by answering to the following questions:

- Can we obtain the systematic convergence between simulations, experiments and LSA on the different regimes of instability?
- Can we proove that the confinement is indeed a destabilizing mechanism, as predicted by LSA?
- Taking advantage of the flexibility of numerical simulations, in synergy with a simplified approach like LSA, what is the impact of injector sizes (liquid or gas) selection on the primary wave formation of an air-water mixing layer?

To do so, we gave in this first chapter all the elements needed to understand the context, the physical mechanisms behind the stability of an air-water mixing layer, the theoretical framework used to reveal these mechanisms, and the challenges associated with the simulation of such flows.

In the second chapter we will give more details on the numerical simulation of atomization, starting from fundamentals of fluid mechanics, to an emphasis on the methods used to produce this work. In the third chapter, we will answer to the questions presented just above.

The fourth chapter is devoted to the numerical development of an open boundary condition for turbulent and multiphase flows. This work started as a side project over the course of the present thesis, with the initial aim of reducing the cost of air-water mixing layers simulations and improving their accuracy. Even though this work is not connected anymore to the other three chapters, it is entirely part of the work done over the course of this thesis.

Chapter 2

Simulating atomization

2.1 Fundamentals of incompressible fluid dynamics

Fluid dynamic is governed by conservation laws. Those conservation laws concern mass, momentum and energy. In a Lagrangian formalism, they are applied on a small volume of fluid that moves at the speed of the flow, whereas in an Eulerian formalism, they are applied on a small volume of fluid that is fixed in space.

We consider a volume V, fixed in space (Eulerian formalism), of external surface

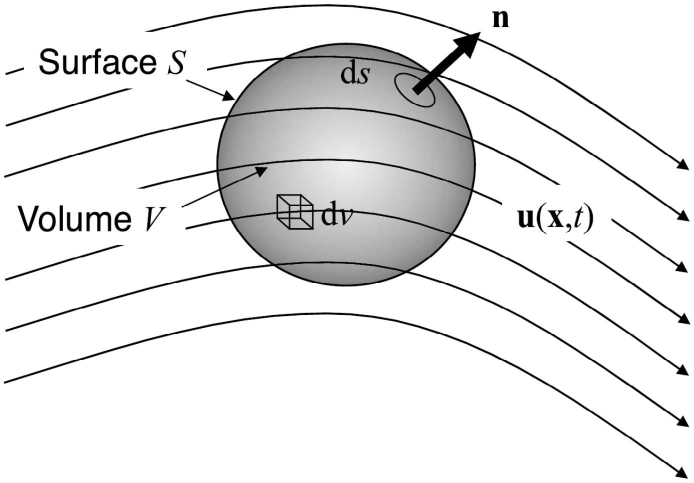

Fig. 2.1 – A control volume V, fixed in space, of external surface S, extracted from (Tryggvason et al., 2011).

S, and with $\mathbf{n}$, the normal vector to its surface oriented towards the exterior of V. $\mathrm{d}S$ and $\mathrm{d}V$ are the infinitesimal surface and volume elements, respectively, see figure 2.1. The velocity field is $\mathbf{u}(\mathbf{x}, t)$, with $\mathbf{x}$ the spatial coordinate vector, and t the time.

Incompressibility condition

The temporal variation of V is related to the flow rate passing through its boundaries, i.e.,

$$\frac{\mathrm{d}}{\mathrm{d}t}\int_V \mathrm{d}V = -\oint_S \mathbf{u}\cdot\mathbf{n}\mathrm{d}S, \tag{2.1}$$

which, using divergence theorem, can be transformed into

$$\frac{\mathrm{d}}{\mathrm{d}t}\int_V \mathrm{d}V = -\int_V (\nabla\cdot\mathbf{u})\mathrm{d}V. \tag{2.2}$$

Therefore, the velocity divergence is related to change in the control volume, i.e., to the local compression or dilatation of the fluid. For an incompressible fluid, the previous equation becomes

$$\nabla\cdot\mathbf{u} = 0, \tag{2.3}$$

which is true as long as the local flow speed is much smaller than the speed of sound.

Mass conservation

The temporal variation of the mass inside V is related to the mass flux passing through its boundaries, i.e.,

$$\frac{\mathrm{d}}{\mathrm{d}t}\int_V \rho\mathrm{d}V = -\oint_S \rho\mathbf{u}\cdot\mathbf{n}\mathrm{d}S, \tag{2.4}$$

which, as the volume is fixed in space and using divergence theorem, can be transformed into

$$\int_V \frac{\partial\rho}{\partial t}\mathrm{d}V = -\int_V \nabla\cdot(\rho\mathbf{u})\mathrm{d}V, \tag{2.5}$$

which is true for any volume V. Therefore, we obtain the local mass conservation equation

$$\frac{\partial\rho}{\partial t} + \nabla\cdot(\rho\mathbf{u}) = 0, \tag{2.6}$$

which can further been expanded into,

$$\frac{\partial\rho}{\partial t} + \mathbf{u}\cdot(\nabla\rho) = -\rho(\nabla\cdot\mathbf{u}), \tag{2.7}$$

whose right hand side will be equal to zero for an incompressible fluid.

Mass being conserved, any compressibility effect (change in volume) will be related to change in density. In incompressible flows, it does not mean that all fluid parcels must have the same density, but that the density of a fluid parcel will not change through time. In incompressible multiphase flows, density is constant within each phase but discontinuous at the interface. Moreover, in incompressible flows, the pressure loses its thermodynamic role and cannot be computed through an equation of state. In an incompressible flow, acoustic phenomena are not considered and pressure waves (sound waves) are supposed to travel at infinite speed.

Momentum conservation

The temporal variation of the momentum inside V is due to the momentum flux passing through its boundaries as well as due to the momentum generated by body forces $\mathbf{f}$ and surface forces $\mathbf{T}$ acting on its boundaries, i.e.,

$$\frac{\mathrm{d}}{\mathrm{d}t}\int_V \rho\mathbf{u}\mathrm{d}V = -\oint_S \rho\mathbf{u}\otimes\mathbf{u}\cdot\mathbf{n}\mathrm{d}S + \int_V \mathbf{f}\mathrm{d}V + \oint_S \mathbf{T}\cdot\mathbf{n}\mathrm{d}S. \tag{2.8}$$

The body force is usually the gravitational force, $\mathbf{f} = \rho\mathbf{g}$, but can be of other nature (e.g., magnetic, rotational acceleration). The surface force is related to the local deformation rate and pressure forces. For a Newtonian fluid, the relation between stress and deformation rate is linear, i.e.,

$$\mathbf{T} = \left(-p - \frac{2}{3}\mu\nabla\cdot\mathbf{u}\right)\mathbf{I} + 2\mu\mathbf{S}, \tag{2.9}$$

where $\mathbf{I}$ is the identity tensor, μ is the viscosity of the fluid and $\mathbf{S} = \frac{1}{2}\left(\nabla\mathbf{u} + \nabla\mathbf{u}^T\right)$ is the deformation rate tensor. This expression for surface stress does only correspond to internal stresses, interfacial stresses being detailed later in this section. Introducing the expression for $\mathbf{T}$ in Eq. (2.8), and using the divergence theorem, the fact that V is fixed in space and the fact that the final relation is true for any volume V, one can obtain the local momentum conservation law,

$$\frac{\partial\rho\mathbf{u}}{\partial t} + \nabla\cdot(\rho\mathbf{u}\otimes\mathbf{u}) = \mathbf{f} - \nabla p - \nabla\left(\frac{2}{3}\mu\nabla\cdot\mathbf{u}\right) + \nabla\cdot(2\mu\mathbf{S}), \tag{2.10}$$

where the third term on the right hand side is equal to zero for incompressible flows.

Similarly, one can build a conservation law for energy that relates the local rate of change of internal and kinetic energy to body, pressure and viscous forces, as well as to the local heat flux, see Tryggvason et al. (2011) for a derivation.

Interfacial boundary condition

Previous equations are valid only if we use them on a scale large enough so that matter can be considered as continuous. Similarly, at a fluid-fluid interface, one can adopt two points of view to describe the transition from one fluid to another: at the microscale, the interface is a zone of interpenetration of the molecules coming from both fluids, whereas at the macroscale we consider the interface as a two-dimensional medium of zero mass and thickness. The thermodynamic desequilibrium at the interface gives rise to the presence of singular forces acting on it. In this work, we only consider the effect of surface tension, but note that shear or dilatational effects can also occur in this two-dimensional medium (Patouillet, 2020).

In the absence of phase change, the application of the momentum balance Eq. (2.8) to a control volume surrounding a fluid-fluid interface (volume of thickness approaching zero and whose normal coincides with the normal to the interface $\mathbf{n}_\Gamma$), and the introduction of the singular force acting on the interface results in

$$[\mathbf{T}]_\Gamma \cdot \mathbf{n}_\Gamma = \sigma\kappa\mathbf{n}_\Gamma + \nabla_S \sigma, \tag{2.11}$$

where κ is the interfacial curvature and ∇_S is the surface gradient operator. The notation $[.]_\Gamma$ refers to the jump from one phase to another. Expressing the previous equation in the normal and tangential directions to the interface results in, respectively,

$$[p]_\Gamma = \sigma\kappa + 2\,[\mu]_\Gamma\, \mathbf{n}_\Gamma^T \cdot \nabla\mathbf{u} \cdot \mathbf{n}_\Gamma, \tag{2.12}$$

$$-\left[2\mu\ \mathbf{t}_\Gamma^j \cdot \mathbf{S} \cdot \mathbf{n}_\Gamma\right]_\Gamma = \mathbf{t}_\Gamma^j \cdot \nabla_S \sigma, \tag{2.13}$$

where $\mathbf{t}_\Gamma^j$ refers to the tangential vectors to the interface. The first boundary condition states that the magnitude of the pressure discontinuity at a fluid-fluid interface is due to the curvature of the interface and the surface tension coefficient, as well as due to viscous effects. The second boundary condition states that a gradient of surface tension can induce a jump of tangential stresses. In the rest of this work, surface tension gradient will be equal to zero.

Moreover, in the absence of phase change, the jump of velocity is zero at the interface, i.e.,

$$[\mathbf{u}]_\Gamma = 0. \tag{2.14}$$

Finally, in incompressible multiphase flows, the set of equations to resolve is composed of Eqs. (2.3)–(2.7)–(2.10) completed by interfacial boundary conditions, Eqs. (2.12)–(2.13)–(2.14), and wall boundary conditions (moving or static walls, contact angles). In the following section we explain how we resolve these equations in the context of airblast atomization. For larger introductions to numerical methods for multiphase flows we refer the reader to Tryggvason et al. (2011) and Mirjalili et al. (2017).

2.2 Numerical methods: generalities

In the previous section we presented the system of equations to be resolved in order to simulate incompressible multiphase flows. No general analytical solution for these equations can be obtained. Numerical simulation thus involves approximating the equations in the best way as possible in order to obtain a solution. One first approximation is that the equations are discretized spatially, i.e., flow variables are known only at specific spatial locations, and temporally, i.e., flow variables are known only at specific instants. Refining these discretizations means getting closer to a space and time continuous solution. Ideally, numerical methods must be able to tend towards the exact solution (if available) when refining discretization, but this involves an increase in the number of operations needed to approximate the equations, therefore an increase of computational cost.

A Lagrangian approach of the spatial discretization would involve a spatial grid moving and deforming at the fluid velocity (see for example the SPH method (Monaghan, 1992)), whereas in an Eulerian formalism the spatial grid is fixed. In the framework of the finite volume method, used in this work, flow variables are stored at specific locations and control volumes are built around those grid points. The governing equations are then solved by evaluating mass and momentum fluxes at the boundaries of these control volumes. In this work, we use a staggered arrangement of the variables, where each of the variables is stored at a different spatial location (Harlow and Welch, 1965). This arrangement is shown on figure 2.2 where one can see a two-dimensional cartesian grid where the shaded area is a computational cell centered on the pressure location, i.e., the pressure cell. Velocity components are stored on the boundaries of this cell. Note that other scalar quantities (volume fraction, temperature) are usually stored at the same location as the pressure.

In case of multiphase flows, Eqs. (2.3)–(2.7)–(2.10) are valid within each phase and coupled by interfacial boundary conditions Eqs. (2.12)–(2.13)–(2.14). Therefore, these equations could be resolved for each phase of the system and coupled through interfacial boundary conditions and closure models (see for example the work of Mer et al. (2018) using this “two-fluids” approach on the test case of an emptying bottle).

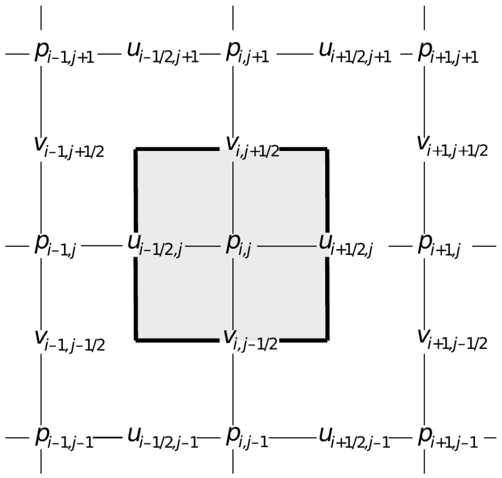

Fig. 2.2 – Staggered arrangement of the variables for a two-dimensional Cartesian grid. Pressure and scalars are located at the center of the grid cells, whereas velocity components are located on their edges. Extracted from Tryggvason et al. (2011).

In this work, we rather use the formalism of the one-fluid model, i.e., a single system of equations is solved for the whole flow and the presence of the different phases is accounted for by using space varying physical properties with the inclusion of singular forces at the interface to account for the presence of surface tension. Local momemtum conservation equation thus becomes, in case of incompressible flows,

$$\frac{\partial \rho \mathbf{u}}{\partial t} + \nabla \cdot (\rho \mathbf{u} \otimes \mathbf{u}) = -\nabla p + \nabla \cdot \left(\mu \left[\nabla \mathbf{u} + \nabla \mathbf{u}^T \right] \right) + \mathbf{T}_\sigma + \rho \mathbf{g}. \tag{2.15}$$

where T_σ is a singular surface tension force acting on the interface and the physical properties, ρ and μ, are function of space and time, i.e., $\rho \equiv \rho(\mathbf{x}, t)$ and $\mu \equiv \mu(\mathbf{x}, t)$. The singular surface tension force is expressed as $T_\sigma = \sigma \kappa \mathbf{n}_\Gamma \delta_S$, where δ_S is a surface Dirac–δ function that is non-zero only at the interface.

Using this formulation, one needs to know the position of the interface in order to compute the physical properties used in Eq. (2.15) from the individual properties of each fluid, and to compute interfacial quantities such as interface normal and interfacial curvature. This is achieved by using a marker function that will identify each fluid in the system. In the following section, we briefly review the different possibilities to use a marker function in order to compute all the quantities related to mass advection and interface deformation, we then explain the methods implemented in the solver used in this work, NGA (Desjardins et al., 2008a).

2.3 Numerical methods: mass advection and interfacial quantities

Advecting the marker function

As said previously, we use a marker function in order to identify the region occupied by each fluid. This can be achieved in many different ways and the disctinction between Lagrangian and Eulerian methods can be made. In a Lagrangian method, instead of directly using a marker function, one uses marker points located on the interface. The marker function is then reconstructed from the marker points. In Eulerian methods, the marker function is advected directly. Lagrangian methods are usually refered to as “Front–Tracking”, whereas Eulerian methods are refered to as “Front–Capturing”.

In Front–Tracking methods, such as the one developped by Unverdi and Tryggvason (1992), the interface is seeded with marker points that are then advected using the fluid velocity interpolated at the marker points locations. Once marker points position is known, one can compute a marker function used to compute the physical properties. Surface tension forces, known at the marker points location, have then to be interpolated back to the Eulerian grid where flow variables are known.

In Front–Capturing method, the marker function is directly advected by the velocity field using the advection equation,

$$\frac{\partial G(\mathbf{x},t)}{\partial t} + \mathbf{u} \cdot (\nabla G(\mathbf{x},t)) = 0, \tag{2.16}$$

where the flow is supposed to be incompressible and $G(\mathbf{x},t)$ is the marker function, whose expression depends on the method.

In the Level-Set method, the marker function is taken as the signed distance between the grid point and the closest interface location (Osher and Sethian, 1988),

$$G(\mathbf{x},t) = \phi(\mathbf{x},t) = \min||\mathbf{x} - \mathbf{x_\Gamma}||, \tag{2.17}$$

where $\mathbf{x_\Gamma}$ is the interface position. The interface is thus located as the isocontour $\phi = 0$. The definition of $\phi(\mathbf{x},t)$ implies that $||\nabla\phi|| = 1$, which will not be the case after advection by Eq. (2.16). The advection step has thus to be completed with a reinitialization step that will modify $\phi(\mathbf{x},t)$ so that the condition $||\nabla\phi|| = 1$ is finally respected. Neither the advection step nor the reinitialization ensure mass conservation, which is the main drawback of the method. Many improvements have been brought to this formulation, such as the Conservative Level-Set (Olsson and Kreiss, 2005), the Accurate Conservative Level-Set (Desjardins et al., 2008b), and their subsequent modifications (McCaslin and Desjardins, 2014; Chiodi and Desjardins, 2017), that all improved the performance of Level-Set methods.

In the Volume-Of-Fluid (VOF) method, the marker function is a discontinuous function that is equal to one in the liquid and zero in the gas (Hirt and Nichols, 1981). The liquid volume fraction, α, is reconstructed by the integration of the marker function in each cell. In grid cells that contains the interface, $0 < \alpha(\mathbf{x}, t) < 1$. Physical properties can be obtained from the knowledge of $\alpha(\mathbf{x}, t)$, e.g., the density can be computed using an arithmetic averaging,

$$\rho(\mathbf{x}, t) = \alpha(\mathbf{x}, t)\rho_l + (1 - \alpha(\mathbf{x}, t))\rho_g, \tag{2.18}$$

and the viscosity using, for example, an harmonic averaging,

$$\mu(\mathbf{x}, t)^{-1} = \alpha(\mathbf{x}, t)\mu_l^{-1} + (1 - \alpha(\mathbf{x}, t))\mu_g^{-1}. \tag{2.19}$$

VOF method is conservative providing that advection step is done carefully, and topological changes are implicit in the formulation. The only information given by the advection step is the field of α. Informations about interface orientation and normals are obtained through a step of interface reconstruction. The method is illustrated on figure 2.3. On figure 2.3a), the real interface is represented using a solid line and the field of $\alpha(\mathbf{x}, t)$ obtained after the advection step is indicated in the cells. Using the values of $\alpha(\mathbf{x}, t)$, one can reconstruct the interface using either the method of Hirt and Nichols (1981) 2.3b), or the PLIC method 2.3c) (Rider and Kothe, 1998). In the PLIC method, used in this work, the interface is represented by a single straight line whose position in the grid cell depends on the normal vector to the interface orientation and the value of the liquid volume fraction.

Many methods have been proposed to advect the marker function in the context of VOF method. The main difficulty being to avoid excessive diffusion of the (discontinuous) marker function while ensuring mass conservation. Two classes can be distinguished: geometric VOF and algebraic VOF. In the first, used in this work, the geometric reconstruction of the interface is needed to compute the VOF fluxes entering trough each grid cell boundaries, while in the latter the marker function is approximated by, for example, a hyperbolic-tangent which allows an algebraic computation of the fluxes (Xiao et al., 2005). Geometric VOF methods can be divided in two sub-classes: split and unsplit advection.

In split advection methods, the advection step Eq. (2.16) is decomposed along each direction and additional steps are used to ensure mass conservation and divergence free. One can cite the schemes of Aulisa et al. (2007) and Weymouth and Yue (2010).

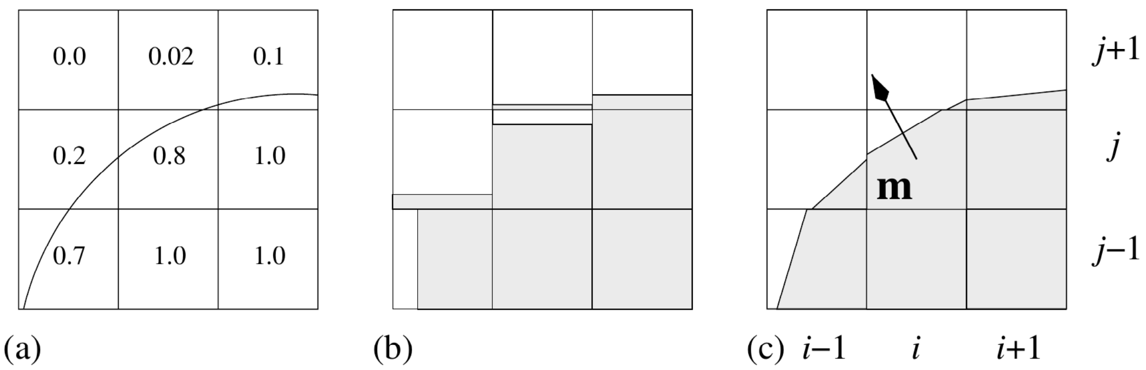

Fig. 2.3 – Illustration of the principle behind VOF method. a) after advection, the liquid volume fraction is known in each pressure cell (indicated in numbers). The real interface is displayed as a thin continuous line. The interface can then be reconstructed using the method of Hirt and Nichols (1981) b), or using the PLIC reconstruction c). The later method requiring the knowledge of the normal orientation represented by the vector **m** on figure c). Extracted from Tryggvason et al. (2011).

In unsplit advection methods, the advection is performed in one single step. In this work we use the unsplit VOF advection method of Owkes and Desjardins (2014) that is illustrated with a two-dimensional example on figure 2.4. The velocity field is first interpolated at the vertices of the pressure cell. Using a simple Lagrangian advection step, the vertices of the cell are projected back in time, i.e., point 2 is projected back in time into point 3. Once this is done for all vertices of the pressure cell, one obtain for each face a three-dimensional flux volume. In 2D, for the left face of the pressure cell, this flux volume is the flux area formed by points $1-2-3-4$. In order to evaluate the flux entering or leaving by the left face of the pressure cell, one need to evaluate the area occupied by the liquid in the flux area. This is done by performing surface cutting (or volume cutting in 3D) operations, until being able to exactly integrate gas and liquid volume fractions in each flux volume.

Once this operation has been performed for all faces of the pressure cell, the new liquid volume fraction can be obtained. Such construction of the flux volumes will avoid overlapping between flux volumes but does not naturally respect divergence free condition. A correction step is therefore needed before performing volume cutting operations, see Owkes and Desjardins (2014) for more details. Note that such scheme has been extended to unstructured grids (Ivey and Moin, 2017). For all volume cutting operations and interface reconstructions we use the open-source library IRL

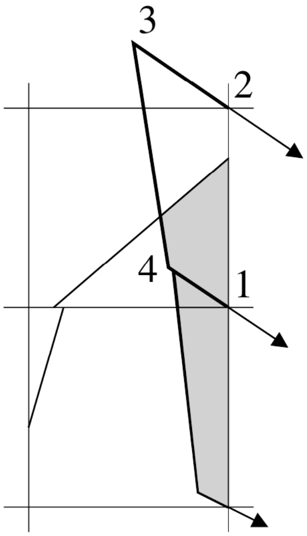

Fig. 2.4 – Illustration of an unsplit geometric VOF advection method. Extracted from Tryggvason et al. (2011).

[1].

Interface reconstruction and curvature computation

Once the liquid volume fraction α is known in every computational cell, the interface can be reconstructed. Using PLIC method, once α is known, the only missing information is the normal orientation, which can be computed in many different ways. One can cite, the gradient method (Youngs, 1982), the least-squares VOF interface reconstruction algorithm (LVIRA, Puckett et al. (1997)) and its efficient version (ELVIRA, Pilliod Jr and Puckett (2004)), or the MOF method (Dyadechko and Shashkov, 2008; Mukundan et al., 2020). We refer to the introduction of Comminal et al. (2015) for an explanation of the differences between these methods. In this work, we use the ELVIRA method as it provides second error convergence on normal orientenation error. Once the normal vector to the interface is obtained, one can perform the PLIC reconstruction step. A recent improvement of the reconstruction method is the two planes reconstruction method (R2P) of Chiodi and Desjardins (2018), which allows the capture of liquid films of thickness much smaller than grid size.

---

[1] Source code available at `https://github.com/robert-chiodi/interface-reconstruction-library`

Once the liquid volume fraction, the normal vector to the interface, and the interface position are known, the remaining interfacial quantity to compute is the interfacial curvature. Such step is of critical importance in atomization simulation, where surface tension effects must be accurately computed for the atomization of the liquid to be correctly captured. Here we detail the way the curvature κ is computed, whereas in the next section we detail how surface tension forces are included into the momentum conservation law. For a larger introduction to surface tension models we refer the reader to the review of Popinet (2018).

Curvature may be obtained from volume fraction by many different methods. Direct use of the volume fraction field, or from a smoothed volume fraction field, from a reconstructed distance function (similarly to what is done in Level-Set methods) are shown not to be converging, i.e., when refining spatial discretization, the error compared to an exact solution is not decreasing (Cummins et al., 2005). On the other hand, the height function method of Poo and Ashgriz (1989); Sussman (2003) has shown to give satisfying results in both error levels and convergence order providing that curvature is low enough compared to spatial resolution (Cummins et al., 2005), i.e., that $\kappa\Delta < 1/5$, with Δ the cell size. Rotated height functions have been developped to improve curvature computation of under-resolved interface (Owkes and Desjardins, 2014). Another class of methods relies on approximating the interface by a paraboloid and resolving a minimization problem to find its best possible orientation, see for example Renardy and Renardy (2002). Such method is found to be efficient for under-resolved interface, even though at the cost of solving a non-linear optimization problem. Switching from height functions to paraboloid approximations is a way to optimize curvature computation over a large range of resolution.

In this work, we use a combination of the height function method of Popinet (2009) and least-squares fits (in a way similar to Owkes et al. (2018)). More exactly, if the height function method fails to provide a sufficient number of heights, we use a least-squares fit of a paraboloid through the PLIC barycenters with weights based on a Gaussian function of the distance to the interface times the PLIC surface area.

As we have detailed how we resolve mass conservation and obtain interfacial quantities, we detail in the next section how we resolve momentum conservation Eq. (2.15).

2.4 Numerical methods: momentum advection

General algorithm

Resolving momentum conservation involves resolving the coupling between velocity and pressure. A popular way to resolve this coupling is through a pressure projection method (Chorin, 1968). In this work we use the incremental pressure projection method of Goda (1979). This method is usually not used for multiphase flows but we saw that, providing that an incremental approach was also used for surface tension forces, this approach was not creating more errors than the classical projection method, in addition of being approximately 30% faster.

Time is advanced through an iterative Crank-Nicolson scheme (Teukolsky, 2000) with an implicit discretization of viscous effects and a semi-implicit discretization of inertial effects. These choices are motivated by energy conservation and stability properties (Desjardins et al., 2008a). In the following equations, superscripts n and $n+1$ refer to previous and new time steps, respectively, whereas subscript k refers to the subiterations of the iterative Crank-Nicolson time advancement scheme. The succesion of equations being resolved in the solver is as follow. Note that we remove surface tension effects of the equations and detail how they are included in a following subsection. First, a non-solenoidal velocity field, $\mathbf{u}^*{}_{k+1}$, is computed as

$$\begin{aligned}\frac{\rho^{n+1}_{k+1}\mathbf{u}^*_{k+1}-\rho^n\mathbf{u}^n}{\Delta t} =& -\nabla p^{n+1}_k - \nabla\cdot\left(\rho^n\mathbf{u}^{n+1/2}_k\otimes\left(\frac{\mathbf{u}^n+\mathbf{u}^*_{k+1}}{2}\right)\right)\\ &+\nabla\cdot\left[\mu^{n+1}\left(\nabla\left(\frac{\mathbf{u}^n+\mathbf{u}^*_{k+1}}{2}\right)+\nabla\left(\frac{\mathbf{u}^n+\mathbf{u}^*_{k+1}}{2}\right)\bigg|^T\right)\right]\\ &+\rho^{n+1}_{k+1}\mathbf{g},\end{aligned} \tag{2.20}$$

where the intermediate velocity field is

$$\mathbf{u}^{n+1/2}_k=\frac{1}{2}\left(\mathbf{u}^{n+1}_k+\mathbf{u}^n\right). \tag{2.21}$$

Then, a Poisson equation is solved for the pressure increment $\Phi^{n+1}=p^{n+1}_{k+1}-p^{n+1}_k$,

$$\nabla\cdot\left(\frac{\Delta t}{\rho^{n+1}_{k+1}}\nabla\left(\Phi^{n+1}\right)\right)=\nabla\cdot\mathbf{u}^*_{k+1}. \tag{2.22}$$

Finally, the velocity and the pressure at the next time step are obtained using Φ^{n+1},

$$\mathbf{u}^{n+1}_{k+1}=\mathbf{u}^*_{k+1}-\frac{\Delta t}{\rho^{n+1}_{k+1}}\nabla\left(\Phi^{n+1}\right), \tag{2.23}$$

$$p_{k+1}^{n+1} = p_k^{n+1} + \Phi^{n+1}. \tag{2.24}$$

Eqs. (2.20), (2.22) and (2.23)-(2.24) are refered to as *estimation*, *projection*, and *correction*. Δt is the time step size. In the case of multiphase flows, ρ^n and μ^{n+1} values are computed from the old and new VOF field, respectively, whereas ρ_{k+1}^{n+1} is computed in a way that ensures consistency between mass and momentum transport, see more details in the next subsection. All spatial derivatives, except the one used in the convective term at the interface, are approximated using second order centered schemes.

At any of the different steps, boundary conditions have to be provided. For more details, we refer to chapter 4 of this manuscript and to Desjardins et al. (2008a).

Details on consistent mass and momentum advections

We give here some details on the strategy used to obtain consistent mass and momentum advections. In order to simplify the explanation, the strategy is detailed in the case of a one-dimensional advection.

As explained earlier, we use a staggered arrangement of the variables, see figure 2.2, where scalar quantities are stored at a different location than velocity components, which may result in spurious interfacial momentum transfer when the coupling between mass and momentum schemes is insufficient, see for example Vaudor et al. (2017).

The staggered arrangement of the variables is illustrated on figure 2.5: cells i and $i-1$ are centered on the pressure location, whereas cell i_u is centered on the axial velocity location. The first step of the consistent methodology is to reconstruct a density field where momentum is computed, i.e., at the velocity location. The liquid volume fraction at the previous time step α^n is known only in cells i and $i-1$, but interface position at time n can be used in order to obtain α_u^n, the old liquid volume fraction in cell i_u. α_u^n is then used to obtain the old density in the staggered cell ρ_u^n.

The next steps are to compute the new staggered density field $\rho_{u,k+1}^{n+1}$, and to enforce consistency between mass and momentum transport using appropriate numerical schemes. To do this, we solve a new equation to obtain $\rho_{u,k+1}^{n+1}$,

$$\frac{\rho_{u,k+1}^{n+1} - \rho_u^n}{\Delta t} + \frac{\partial \rho_u^n u_k^{n+1/2}}{\partial x} = 0, \tag{2.25}$$

before the estimation step,

$$\frac{\rho_{u,k+1}^{n+1} u_{k+1}^{*} - \rho_u^n u^n}{\Delta t} + \frac{\partial \rho_u^n u_k^{n+1/2} u_{k+1}^{n+1/2}}{\partial x} = RHS, \tag{2.26}$$

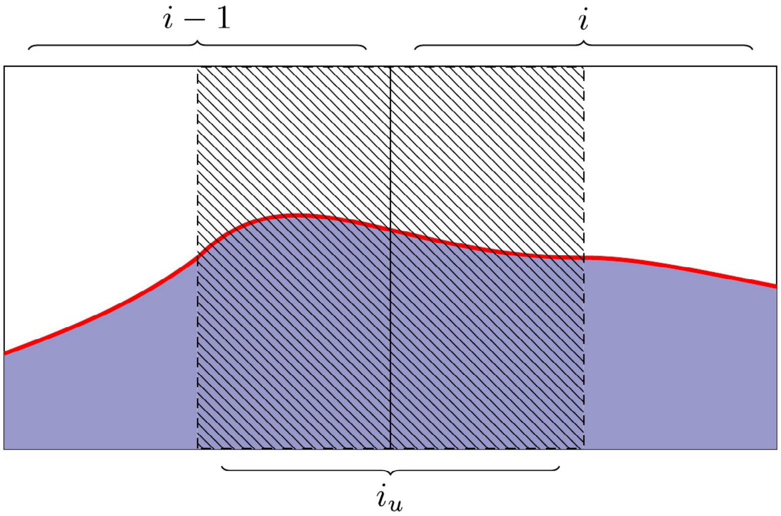

Fig. 2.5 – Illustration of the staggering of the variables and of the strategy to obtain consitant mass and momentum trasnport. Density and momentum fluxes have to be reconstructed in the staggered cell i_u. Extracted from Palmore and Desjardins (2019).

where RHS represents all the terms on the right hand side of Eq. (2.20). The key aspect of this treatment is that, at the interface, the advective fluxes in Eqs. (2.25) and (2.26) must be discretized using the same operator. In our case $\partial/\partial x$ is approximated using a first order upwind scheme. See Palmore and Desjardins (2019) for more details. Note that viscosity is also computed using a staggered approach, and is computed directly where the viscous fluxes are evaluated.

Inclusion of surface tension forces

As said previously, surface tension forces are expressed as $T_\sigma = \sigma\kappa\mathbf{n}_\Gamma\delta_S$. We explained in a previous section how we compute κ. We now detail the way surface tension forces are included into momentum conservation law

The product $\mathbf{n}_\Gamma\delta_S$ can be expressed as the gradient of a Heaviside function H, i.e.,

$$T_\sigma = \sigma\kappa\mathbf{n}_\Gamma\delta_S = \sigma\kappa\nabla H, \tag{2.27}$$

where different choices can be made for H, see Popinet (2018) for a review. In our case we use the CSF approach (Francois et al., 2006) where H is equal to α.

For $\mathbf{u} = 0$, momentum conservation, Eq. (2.15), reduces to,

$$-\nabla p + \sigma\kappa\nabla H = 0, \tag{2.28}$$

which, in case of constant σ and κ, further reduces to

$$-\nabla\left(p - \sigma\kappa H\right) = 0. \tag{2.29}$$

This equation has an exact solution, $p = \sigma\kappa H + \text{constant}$, that can be recovered numerically only if the same discrete operator is used to evaluate the pressure gradient and the gradient of H, i.e., if the formulation is well-balanced (Francois et al., 2006; Popinet, 2018). A one-dimensional well-balanced formulation is therefore,

$$-\frac{p_{i+1} - p_i}{\Delta} + (\sigma\kappa)_{i+1/2}\frac{\alpha_{i+1} - \alpha_i}{\Delta} = 0, \tag{2.30}$$

where the gradients are evaluated using the same centered scheme and where Δ is the cell size. Note that curvature has to be evaluated at the location $i+1/2$, i.e., the location where gradients of pressure and α are evaluated. In our case, curvature is evaluated at $i+1/2$ using a surface area wheighted interpolation from known values in cells i and $i+1$.

In our solver, surface tension forces are included in the pressure gradient using an incremental approach. In Eq. (2.20), $-\nabla p_k^{n+1}$ is thus replaced by $-\nabla p_k^{n+1} + (\sigma\kappa\nabla\alpha)^n$. In Eqs. (2.22) and (2.23), the pressure increment gradient is completed by surface tension forces, i.e., $\nabla\Phi^{n+1}$ is replaced by $\nabla\Phi^{n+1} + (\sigma\kappa\nabla\alpha)^n - (\sigma\kappa\nabla\alpha)^{n+1}$.

Note that the interfacial boundary condition Eq. (2.12) contains a jump of normal stress due to a jump in viscosity, and that Eq. (2.13) involves the continuity of tangential stresses. In our approach, as viscosity is function of α (harmonic averaging), the viscous term in momentum conservation law Eq. (2.15) already includes these boundary conditions.

Conclusion on the flow solver

We have thus describe the main elements of the numerical solver used in the present work. This solver has been extensively validated on a large collection of configurations, from single-phase flows (Desjardins et al., 2008a) to airblast water layer simulations (Agbaglah et al., 2017). This solver is exactly mass, momentum and energy conserving within each phase while mitigating momentum and energy conservation errors at the interface even in the presence of high density or viscosity ratio, high shear or large exchange of kinetic energy.

An open-source version of this solver, NGA2, upgraded with an object-oriented structure that allows overlapping of multiple meshes and simulations, is now available [2].

---

[2] Source code available at `https://github.com/desjardi/NGA2`

Chapter 3

Stability of an air-water mixing layer: focus on the confinement effect

Abstract

The content of this chapter until the end of section 3.3 has been created in collaboration with Prof. Jean-Philippe Matas (Univ. Lyon 1/LMFA). The results of section 3.4 have been partially obtained by Samantha Pereira (Cornell U.) during her undergraduate research project under my guidance.

3.1 Configuration

We study a wall-bounded air-water mixing layer corresponding to the configuration studied experimentally in Matas et al. (2011). The description of the numerical domain is presented in figure 3.1a). A slow liquid stream with velocity U_l, located above a wall, is placed below a fast gas stream with velocity U_g. Liquid and gas streams both have a finite thickness, H_l and H_g, respectively. The domain is 2D, with a velocity field defined as $\mathbf{u} = (u, v)$, where u, v are the velocity components in the x, y directions, respectively, with $0 \leq x \leq L_x$ and $0 \leq y \leq L_y$.

We choose not to include the splitter plate separating the gas and liquid streams. This has two advantages: firstly, we avoid the simulation of the contact line dynamics on the splitter plate, which is expensive given the typical scales of the splitter plate; secondly we retain full control over the shape of the initial velocity profile. Linear stability (Matas, 2015; Otto et al., 2013) has shown that the details of the

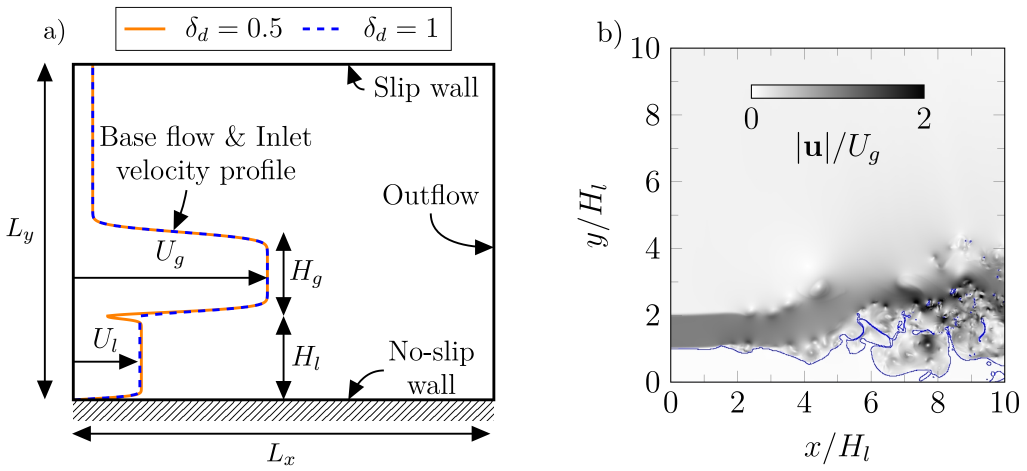

Fig. 3.1 – a) Sketch of the configuration. The deficit value δ_d controls the initial shape of the velocity profile close to the interface. b) Typical picture of the flow displaying the liquid-gas interface (blue line) and the velocity magnitude (gray scale).

velocity profile close to the interface and the finite thickness of the streams control the transition between convective and absolute regime, as well as the transition from confinement-induced to surface tension-induced absolute instability. In this study, we compare the results obtained using simulations, i.e., a fully non-linear and global approach that allows for the development of the base flow, and linear stability analysis, i.e., a highly idealized approach that performs a local analysis of a parallel base flow subjected to infinitesimal perturbations. Both approaches are connected as the inlet velocity profile in simulations is also used as the base flow in the linear stability analysis.

The inlet velocity profiles are expressed as $\mathbf{u}_{in} = \mathbf{u}(x = 0, y) = (u(y), 0)$. The expression of $u(y)$ depends on the vertical position. For $y \leq H_l$,

$$u(y) = \left\{ U_l \mathrm{erf}\left(\frac{H_l - y}{\delta_l}\right) + U_i \left(1 + \mathrm{erf}\left(\frac{y - H_l}{\delta_d \delta_l}\right)\right)\right\} \times \mathrm{erf}\left(\frac{y}{\delta_l}\right), \tag{3.1}$$

for $H_l < y \leq H_g + H_l$,

$$u(y) = \begin{cases} \left\{ U_g \mathrm{erf}\left(\frac{y - H_l}{\delta_g}\right) + U_i \left(1 - \mathrm{erf}\left(\frac{y - H_l}{\delta_d \delta_l}\right)\right)\right\} \\ \times \mathrm{erf}\left(\frac{H_g + H_l - y}{\delta_g}\right) \\ + U_{sm}\left(1 + \mathrm{erf}\left(\frac{y - (H_g + H_l)}{\delta_g}\right)\right), \end{cases} \tag{3.2}$$

and for $y > H_g + H_l$,

$$u(y) = U_{sm}\left(1 - \mathrm{erf}\left(\frac{y - (H_g + H_l)}{\delta_g}\right)\right) + U_{cf}\mathrm{erf}\left(\frac{y - (H_g + H_l)}{\delta_g}\right). \tag{3.3}$$

In the previous expressions, δ_g is the gas vorticity thickness, δ_l is the liquid vorticity thickness, δ_d is the dimensionless deficit parameter, U_i is the interfacial velocity, $U_{cf} = 0.1U_g$ is the co-flow velocity, and $U_{sm} = (U_{cf} + U_g)/2$ is the single-phase mixing layer velocity. The gas vorticity thickness is computed using the experimental correlation given in Matas et al. (2011): $\delta_g = 6H_g/\sqrt{\rho_g U_g H_g/\mu_g}$. Note that, in the following, when H_g is varied we do not vary δ_g but instead keep the value obtained using the previous relation for $H_g = 1$ cm. The liquid vorticity thickness is constant and equal to 5×10^{-4} m. Following Otto et al. (2013), the interfacial velocity is defined based on tangential stresses continuity, $U_i = (U_g\mu_g/\delta_g + U_l\mu_l/\delta_l)/(\mu_l + \mu_g)\delta_d\delta_l$, with μ_l and μ_g the liquid and gas dynamic viscosities, respectively. The deficit parameter δ_d is used to control the magnitude of the interfacial velocity, therefore the shape of the velocity profile around the liquid gas interface: if $\delta_d = 1$, there is no velocity deficit, while a reduction of δ_d will induce a decrease of the interfacial velocity, as seen on figure 3.1a). This velocity profile only differs from the one used for linear stability by the presence of a co-flow used to provide the mass entrained by the high speed gas (as in da Silva and Métais (2002a)). Note that one will exactly recover the velocity profiles used for linear stability analysis with $U_{cf} = 0$.

The inlet velocity profile described by Eqs. (3.1)-(3.3) is imposed at $x = 0$. Except stated otherwise, a uniformely random perturbation of maximum amplitude $\epsilon = 10^{-5}$ m/s is introduced at the inlet on both components of the velocity in a band of width δ_g around the interface. A convective outlet boundary condition is imposed at $x = L_x$ (Orlanski, 1976). The convective velocity used in that condition is taken as the maximal speed in the vicinity of the outlet plane. The bottom boundary condition at $y = 0$ is a no-slip wall, while the top boundary condition $y = L_y$ is a slip wall. The physical properties of air and water, as well as σ, the surface tension coefficient at an

ρ_l (kg/m^3)	ρ_g (kg/m^3)	μ_l (Pa · s)	μ_g (Pa · s)	σ (N/m)
1000	1.2	10^{-3}	1.8×10^{-5}	0.072

Table 3.1 – Physical properties of air and water

Case	U_g (m/s)	U_l (m/s)	M $(-)$	$Re_{g,Hg}$ $(-)$	$Re_{l,Hl}$ $(-)$
A1	22	0.50	2.32	14667	5000
A2	22	0.37	4.24	14667	3700
A3	22	0.26	8.59	14667	2600
B1	27	0.50	3.49	18000	5000
B2	27	0.37	6.39	18000	3700
B3	27	0.26	12.94	18000	2600

Table 3.2 – Summary of injection conditions and relevant non-dimensional parameters for $H_g = H_l = 1$ cm.

air-water interface, are taken as constant throughout this study and are presented in table 3.1. Gravity is taken into account, with $\mathbf{g} = (0, -9.81)$ m/s^2 the gravity vector. The numerical domain is discretized with a uniform cell size, $\Delta x = \Delta y = \delta_g/n$, with n to be specified later, for $y \leq 6H_l$. In the upper part of the domain, the mesh is progressively stretched in the vertical direction up to $y = L_y = 1.3L_x$ using a constant stretching ratio of 1.05.

All the combinations of injection velocities used in this paper, as well as relevant non-dimensional parameters, are summarized in table 3.2 for the case where $H_g = H_l = 1$ cm. The additional non-dimensional parameters presented in table 3.2 are the gas stream Reynolds number, $Re_{g,Hg} = \rho_g U_g H_g/\mu_g$ and the liquid stream Reynolds number, $Re_{l,Hl} = \rho_l U_l H_l/\mu_l$.

Finally, the base flow for stability analysis is the inlet velocity profile, with $U_{cf} = 0$. The method used is the same as in Matas (2015). After superposition of a perturbation to the base flow and linearization, the perturbations are expanded into normal modes of the form $\tilde{\mathbf{u}}(k, y, \omega)\mathrm{e}^{\mathrm{i}(kx-\omega t)}$, witk k and ω the complex wavenumber and complex frequency, respectively. Gravity is taken into account. Integration of the resulting equations with a Runge-Kutta method is carried out from the solid wall in the liquid, and from a solid wall located at a distance L_g in the gas phase, with L_g much larger than the stream thicknesses, namely $L_g = 30\max(H_g, H_l)$. The dispersion relation results from the connection of these integrated liquid/gas solutions at the interface via appropriate continuity of normal and tangential stresses.

The dispersion relation is solved for complex k using a shooting method, for fixed complex ω. The absolute modes are then tracked using the Briggs criterion (Briggs, 1964): we look for a pinching between branches (controlled by shear, confinement or surface tension) located in opposite sides of the k half-plane at large ω_i, with ω_i the imaginary part of the complex frequency. Particularly, this pinching must occur at positive ω_i for the instability to be considered as absolute, and $\partial\omega_r/\partial k_r$, the group velocity, is equal to zero at the pinching point, with ω_r and k_r the real part of the complex frequency and wavenumber, respectively.

3.2 Stability of an air-water mixing layer

General description

A typical flow picture displaying the liquid-gas interface and the velocity magnitude is presented on figure 3.1b). Initially flat, the interface progressively deforms into a wavy shape. The liquid strongly interacts with the high speed jet in the downstream part of the flow: the liquid jet gets thinner due to the transfer of momentum from gas to liquid and flow rate conservation, but one can also see large amplitude waves deviating the gas jet, as well as ligaments and liquid fragments pulled out by the jet. The gas-gas mixing layer shows the triggering of a Kelvin–Helmholtz instability. No recirculation is observed in the top part of the domain, showing that the co-flow actually provides the mass entrained by the high speed jet. The vertical position of the interface is sampled for all positions downstream of the inlet at a frequency of $10,000$ Hz, allowing the study of the spatio-temporal development of the instability.

On figure 3.2a), we show the spatial evolution of the wave amplitude, and on figure 3.2b) the spectrogram of the interface height for case A2, with $n = 2$ and $\delta_d = 1$. The wave amplitude is computed using the method presented in Matas et al. (2011): for a given downstream position, we construct a histogram of the interface positions over the sampling time and exclude the lowest and highest 0.5%. The remaining width of the histogram is taken as the amplitude A of the waves. Several zones can be distinguished. Focusing on figure 3.2a), one can see that for $20 \leq x/\delta_g \leq 50$, the computed amplitude ($\circ$) seems to increase exponentially with downstream distance,

$$A = A_0 e^{k_i x}, \tag{3.4}$$

with, for figure 3.2a), $k_i = k_{i,exp} = 323.2\ \mathrm{m}^{-1}$, where $k_{i,exp}$ is the value obtained experimentally (Matas et al., 2011), as represented with a dashed line on figure

3.2a).

This observation has to be taken cautiously. The stability analysis predicts that the instability is absolute for these conditions, as seen on figure 3.3, where we see the pinching between the confinement branch, located close to the k_i axis, and the shear branch. Non-linearity is therefore expected to quickly dominate. As the group velocity at the pinching point is zero, the predicted spatial growth rate has no clear meaning for the waves travelling downstream of the injector (Huerre and Monkewitz, 1990). This exponential growth zone has been seen experimentally and numerically (Agbaglah et al., 2017; Ling et al., 2019). Figure 3.2a) shows that the wave growth obtained numerically is in agreement with the wave growth observed experimentally. The insert in figure 3.2a) shows that the zone of exponential growth rate is extremely short, as seen in experiments.

The end of the previous zone occurs when the amplitude is on the order of the vorticity thickness, as observed in experiments. For $x/\delta_g \geq 75$, the amplitude is growing linearly with downstream distance, following well the self-similar model of Hoepffner et al. (2011),

$$A = C_0 \sqrt{\rho_g/\rho_l} U_g \tau, \tag{3.5}$$

with the characteristic time taken as $\tau = x/U_D$, as in Marty (2015), U_D is obtained using Eq. (1.18), and C_0 is a model constant to be specified. This model is represented by the continuous line in figure 3.2a).

On figure 3.2b), one can see the spatial evolution of the interface height spectra. For each location downstream of the inlet, we obtain the interface height spectrum and then normalize the spectral power by its local maximum. Note that we use the Welch method (Welch, 1967) to facilitate the extraction of the most amplified frequency, i.e., before taking its Fourier transform, we split the signal in 10 parts with a 60% overlap between them, the resulting spectra are then averaged. The most amplified frequency remains unchanged over a large extent of the domain and a very clear peak is observed, in agreement with the absolute nature of the instability. Close to the outlet, lower frequency peaks are appearing.

In the next section, we detail the influence of the numerical parameters and the integration time on these results.

Assessment of the numerical methods

On figure 3.4a), we show the influence of integration time on the most amplified frequency obtained at three downstream locations for two sets of injection conditions. The most amplified frequency is presented as a function of the normalized duration of

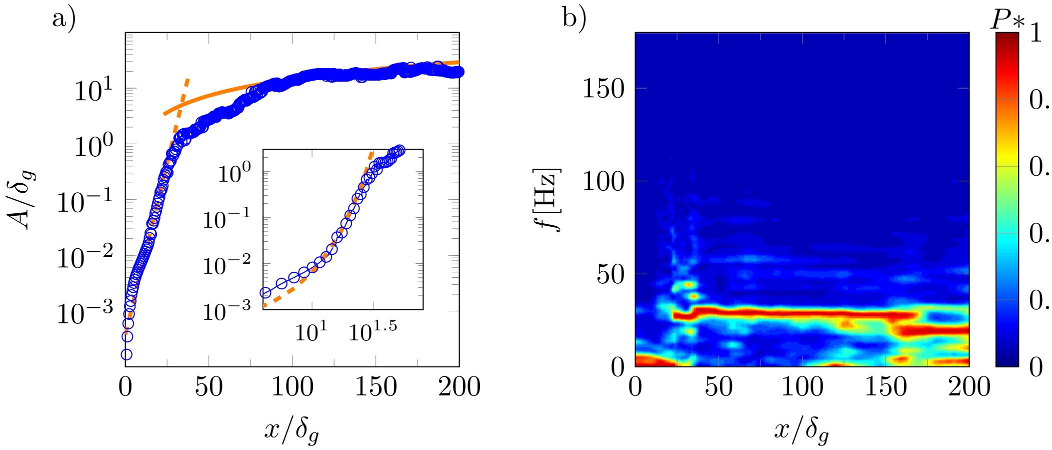

Fig. 3.2 – Spatio-temporal development of the instability for the case A2 with $n = 2$, $\delta_d = 1$. a) spatial evolution of the wave amplitude. ○: computed wave amplitude, ⋯: Eq. (3.4), with $A_0/\delta_g = 3.8 \times 10^{-4}$ and $k_i = k_{i,exp} = 323.2\ \mathrm{m}^{-1}$, −: Eq. (3.5), with $C_0 = 0.21$. The insert shows the same data in a log scale, with a zoom in on the exponential growth region. b) spectrogram of the interface height. $P*$ is the normalized spectral power.

the signal $\Delta T f_{th}$, with ΔT the signal duration and f_{th} the predicted wave frequency obtained by linear stability analysis. Note that the statistics are collected once the averaged height is stabilized over time. One can see that as soon as $\Delta T f_{th}$ is larger than 10, i.e., approximately 10 waves have been generated, the variations of the most amplified frequency in time and space are of the order of the spectral resolution. This is in agreement with the results of Agbaglah et al. (2017). For both cases, the most amplified frequency is stable in time, and with the increase of spectral resolution all measured frequencies become perfectly independent of the position, providing that the latter is in the interval $25 \leq x/\delta_g \leq 150$. In order to reduce the uncertainty on the frequency value an integration time of $\Delta T f_{th} \geq 40$ would be ideal, but this choice will be more difficult to achieve for 3D simulations, or even very resolved 2D simulations. The present analysis shows that even an integration time of $\Delta T f_{th} \sim 10$ is sufficient to obtain a good estimate of the frequency.

On figure 3.4b), we show the impact of domain length on the frequency spectra for two sets of injection conditions. Our tests show that, for the cases of figure 3.4b), the most amplified frequency is not affected by the position of the outlet boundary condition once L_x/δ_g is larger than 240, which has been confirmed for other cases (results not shown). We will therefore ensure that this condition is met for all cases.

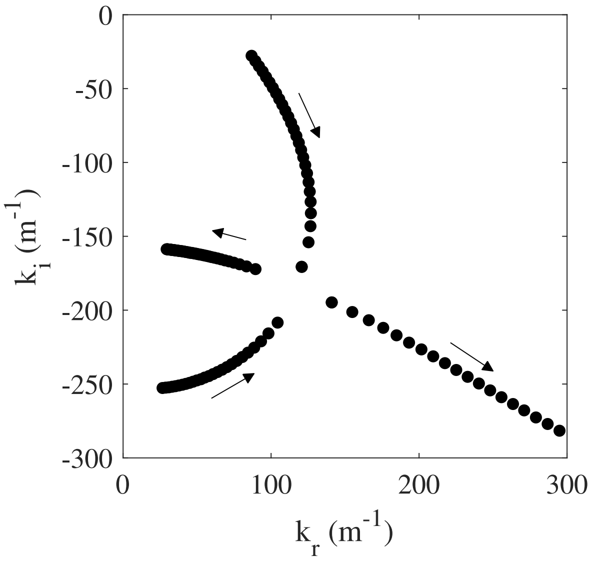

Fig. 3.3 – Case A2. Pinching between confinement and shear branches, at $\omega_i = 30$ s^{-1}. The confinement branch is located close to the k_i axis. The arrows indicate the direction in which ω_r increases.

On figure 3.5, we show the effect of resolution on the spatio-temporal development of the instability for case $B1$ and two values of the deficit parameter. On figure 3.5a) is presented the evolution of the frequency spectra with n ($= \Delta x/\delta_g = \Delta y/\delta_g$), the resolution, for $\delta_d = 1$. We see that, as the mesh is refined, the most amplified frequency approaches the theoretical value. The error on the finest mesh, here $n = 8$, is of only 4.6%, while the error for the coarsest resolution, $n = 2$, is of 12%. On figure 3.5b) the convergence of the amplitude with mesh resolution for $\delta_d = 1$ is shown. From $n = 2$ ($\triangle$) to $n = 16$ (+) the amplitude is mostly affected by the resolution in the area close to the injector, where the amplitude is small. Far from the inlet, i.e., $x/\delta_g \geq 75$, the amplitude is essentially not affected by resolution and closely follows the self-similar model. Mesh resolution mostly affects the location at which the amplitude reaches this self-similar region. This location is shifted closer to the injector as the mesh is refined. Note that the amplitude is essentially not modified between $n = 8$ and $n = 16$, meaning that we reach independence from mesh resolution. Note also that, close to the injector, we do again see a zone of exponential growth, with a slope equal to the one observed experimentally for these injection conditions. As the mesh is refined, the transition between the inlet of the domain and the zone of exponential growth progressively disappears, which is not

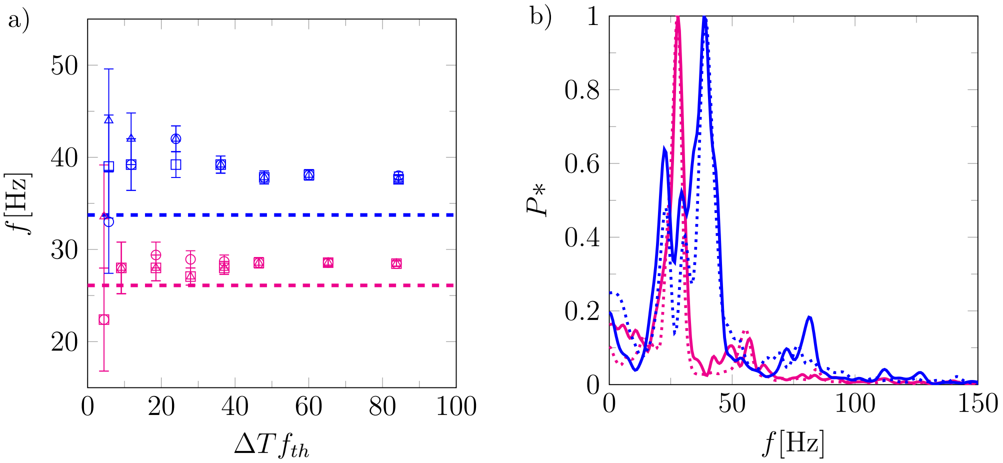

Fig. 3.4 – (Color online) Dependence of frequency measurements on integration time and domain length for $n = 2$, $\delta_d = 1$. a) Spatio-temporal convergence of the most amplified frequency. Blue: case B1, magenta: case A2. ○: $x/\delta_g = 44$, △: $x/\delta_g = 67$, □: $x/\delta_g = 89$. The error bars represent the spectral resolution. Horizontal dashed lines: theoretical frequency for each case. b) Dependence of frequency spectra on domain length for $\Delta T f_{th} = 40$, $x/\delta_g = 89$. Blue: case B1, magenta: case A2. Continuous line: $L_x/\delta_g = 240$, dotted line: $L_x/\delta_g = 320$

the case in experiments (Matas et al., 2011) or simulations including a splitter plate (Agbaglah et al., 2017; Ling et al., 2019).

On figure 3.5c), we present the evolution of the frequency spectra with mesh resolution for $\delta_d = 0.5$ and the same B1 case. Again, one can see that, as the mesh is refined, the most amplified frequency converges towards the predicted value, but the error on the finest resolution, $n = 10$, is still of 12%. The evolution of amplitude with resolution for $\delta_d = 0.5$ is shown on figure 3.5d). Similarly to the case without velocity deficit, we can see that as the mesh is refined, the position at which the amplitude enters the self-similar region is shifted towards the inlet. In the exponential growth region, we are again in very good agreement with the slope measured experimentally by Matas et al. (2011). Note that we do observe that the self-similar growth region is affected by the reduction of δ_d as we had to increase C_0 from 0.21 to 0.27 in order to obtain a good agreement between the computed amplitude and Eq. (3.5) in the downstream area. This is consistent with our observation of a decrease in the wave speed with the decrease of δ_d (results not shown). This suggests, as already pointed out by Marty (2015), that one needs to adjust the velocity scale used in Eq. (3.5) to

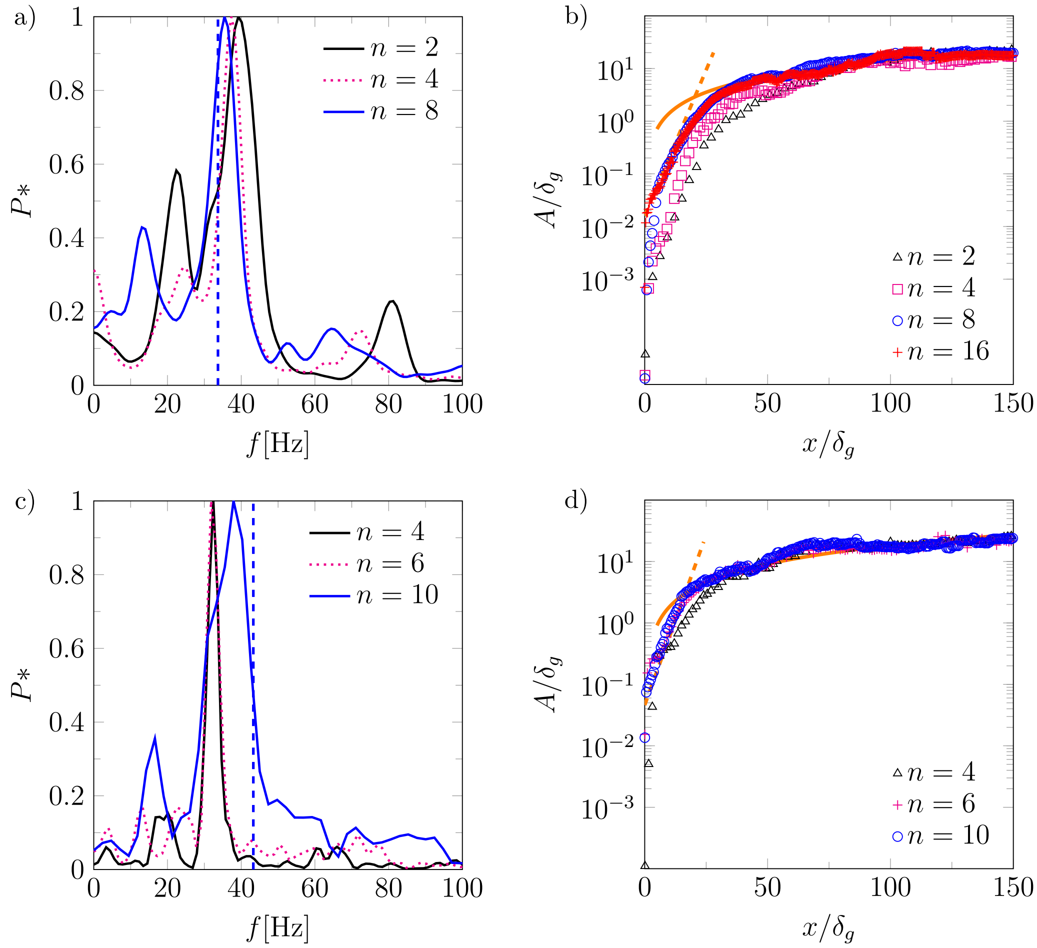

Fig. 3.5 – (Color online) Effect of mesh resolution on the instability characteristics for case B1 and two values of the deficit parameter. In the zone of interest, $\Delta x = \Delta y = \delta_g/n$. All spectra are taken at $x/\delta_g = 67$, with $\Delta T f_{th} \geq 20$. a) Convergence of frequency with mesh resolution for $\delta_d = 1$. The vertical dashed line represents the corresponding theoretical frequency. b) Convergence of wave amplitude with mesh resolution for $\delta_d = 1$. ⋯: Eq. (3.4), with $A_0/\delta_g = 0.016$ and $k_i = k_{i,exp} = 569.9$ m^{-1}, −: Eq. (3.5), with $C_0 = 0.21$. c) Similar to a), with $\delta_d = 0.5$. d) Similar to b), with $\delta_d = 0.5$, $A_0/\delta_g = 0.046$ and $C_0 = 0.27$. Note that in b) and d), only 1 data point every 6 is shown to enhance readability.

the variations of the interfacial wave speed, therefore to the details of the velocity profile, in order to obtain a good self-similarity of the wave amplitude.

Overall, we find that the influence of the velocity deficit δ_d is expensive to capture and the systematic study of its influence on the simulation results is left to future work. For the rest of this work, we will only consider the $\delta_d = 1$ case in simulations. Nonetheless, we wish to comment on the reason for this difficulty. As pointed out by Otto et al. (2013), and seen on figure 3.1a), the presence of an interfacial velocity deficit induces the presence of a minimum in the velocity profile, in our case on the liquid side, around which the shear changes sign. Depending on the value of δ_d and other injection parameters, this minimum can move very close to the interface. In our case this minimum is located at a distance of $238\,\mu$m from the interface, hence a distance twice smaller than the vorticity thickness. Reducing δ_d or M can make this minimum move even closer to the interface (Otto et al., 2013). The position of this minimum and the associated shear are very expensive to capture in simulations, hence the difficulty to capture the effect of δ_d. Unlike the case of convective modes presented in Bagué et al. (2010), we do not observe the presence of extremely sharp variations of the eigenfunctions associated with the mode of instability, as can be seen on figure 3.6, where we show $|\Psi|$, the norm of the stream function computed by the stability analysis for case $B1$ and for two values of δ_d: $\delta_d = 1$ (dashed line) and $\delta_d = 0.5$ (continuous line), as a function of the vertical coordinate. The stream function is related to the vertical velocity perturbation: $\partial\Psi/\partial x = \tilde{v}(k, \omega, y)\mathrm{e}^{\mathrm{i}(kx-\omega t)}$. No significant difference is observed between both cases, except a slightly higher value of $|\Psi|$ in the gas stream for $\delta_d = 1$. Thus, we think that the difficulty associated with the resolution of the velocity deficit is solely due to the difficulty of resolving the velocity minimum position and the associated shear, rather than to an increase in the eigenfunctions sharpness. Note that this comment only applies to confinement-induced absolute modes which occur at low wavenumbers (Matas, 2015).

This mesh convergence study shows that, focusing on the case where no interfacial velocity deficit is introduced, a resolution $n = 8$ allows a converged amplitude and a very low error on the frequency value. We will therefore choose this resolution in section 3.2 where we will compare simulation results obtained for all cases presented in table 3.2. However, the previous mesh convergence study also shows that a resolution $n = 2$ leads to an acceptable error on the frequency, as well as an amplitude that follows the self-similar growth model. We will therefore choose $n = 2$ in section 3.3, devoted to the analysis of the effect of confinement on the stability of the flow.

We have thus established the performance and the limits of our numerical methods, which could be useful for the development and validation of future methods. We

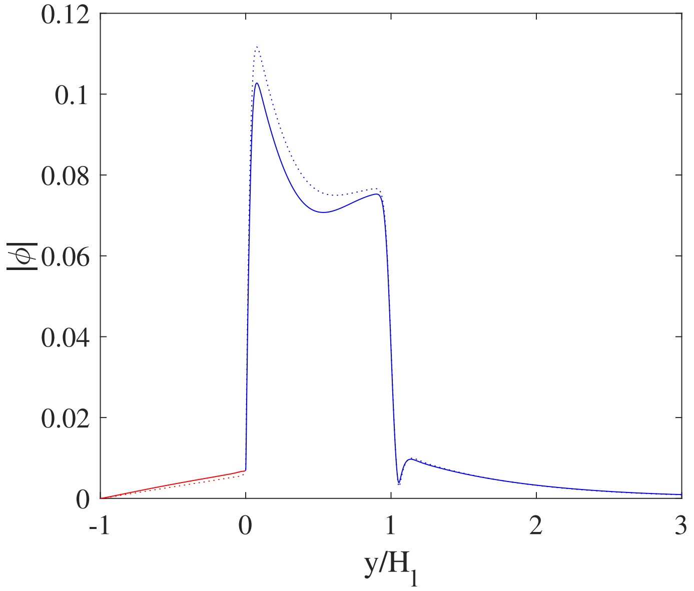

Fig. 3.6 – Absolute value of the stream function eigenfunction for case B1 with $H_g = H_l = 1$ cm. Dotted line: $\delta_d = 1$ ($k = 140 + 170i$ m^{-1}, $\omega = 209 + 30i$ s^{-1}), continuous line: $\delta_d = 0.5$ ($k = 135 + 195i$ m^{-1}, $\omega = 272 + 35i$ s^{-1}). Red: liquid side, blue: gas side. The horizontal axis is rescaled so that the $y = 0$ location corresponds to the interface location.

now switch to the use of the solver to demonstrate convergence between simulations, linear theory, and experiments on confinement-induced absolute modes.

Convergence between simulation, linear theory, and experiments

On figure 3.7a), we show the evolution of the most amplified frequency obtained numerically, for $n = 8$ (○) and $n = 2$ ($*$), as a function of the dynamic pressure ratio and for all cases of table 3.2. We plot the numerical results along with the most amplified frequency obtained with linear stability analysis (△). For all cases of table 2, the stability analysis predicts that the instability is absolute, driven by a resonance of the shear instability within the confined streams (confinement mechanism). We also add for reference the experimental results of Matas et al. (2011) (□). We do see that the comparison between simulation and linear stability analysis is very satisfactory, with a level of error varying between 0.5% and 14% on the finest resolution, and

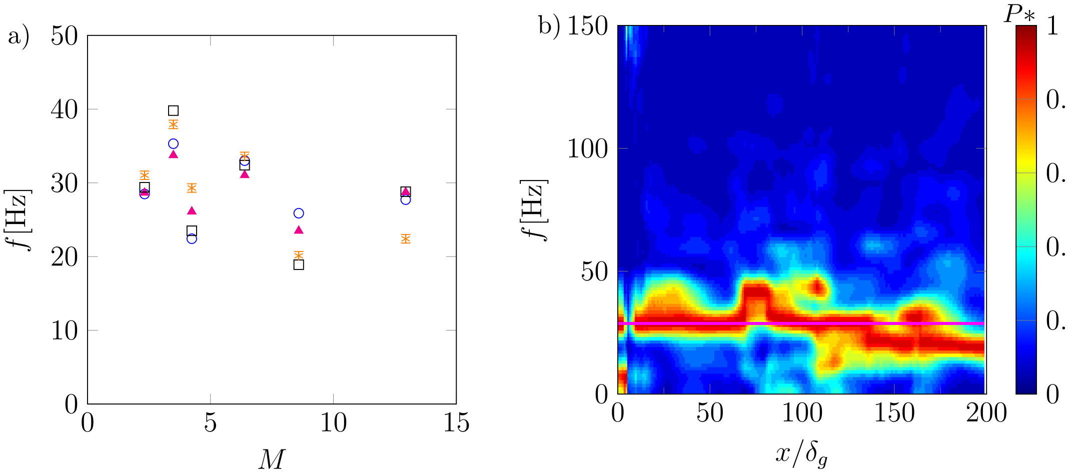

Fig. 3.7 – (Color online) a) Most amplified frequency of the interface height signal as a function of the dynamic pressure ratio for all cases of table 3.2. □: experimental results (Matas et al., 2011), △: linear stability analysis results, ∗: simulation results with $n = 2$, ○: simulation results with $n = 8$. b) Spectrogram of the interface height signal for case $A1$, with $n = 8$. The horizontal magenta line represents the predicted wave frequency.

between 8% and 21% on the coarsest. Moreover, the comparison with experiments is very favorable.

This is a significant result because it shows that, while the level of error may vary between cases, we do observe convergence between simulation, linear stability analysis and experiment on cases where the instability is triggered by confinement. The inclusion of the finite thickness of liquid and gas streams in the stability analysis has been shown to allow the convergence between experiments and linear stability analysis (Matas, 2015; Matas et al., 2018), here we do confirm for the first time its impact through simulations. Our work is therefore highly complementary to the one presented in Fuster et al. (2013), which showed convergence between simulation, linear stability analysis, and experiments on surface tension-induced absolute instabilities. In section 3.3, we will give further evidence of the destabilizing influence of confinement.

In figure 3.7b), we show a spectrogram of the interface height signal for case A1 with $n = 8$. One can see that the most amplified frequency is not perfectly constant with downstream distance, but that it matches the theoretical value for more than half of the spatial locations. We can thus question the appearance of such small spatial variations of the most amplified frequency. A possibility would be to question the local or global nature of the mode of instability (Huerre and Monkewitz, 1990). The frequencies predicted by linear stability analysis correspond to the stability property of the inlet velocity profile, but do not give the information of whether the predicted absolute mode is local or global. However, it is observed experimentally that the most amplified frequency does not vary with downstream distance (Matas et al., 2011), i.e., that the absolute mode is global. We observed in our simulations that those spatial frequency variations are increasing with resolution. Therefore, we postulate instead that this is an effect of the 2D nature of the simulation, and particularly of the 2D nature of the turbulence. Note that a decrease of frequency with downstream distance has already been observed for similar 2D configurations with moderate density ratios, and was attributed to vortex pairing (Fuster et al., 2009) or wave merging (Valluri et al., 2010). A way to improve the understanding of spatial frequency variations would be to perform a mesh convergence in 3D under experimental conditions, but this task is made difficult by its very high computational cost.

In figure 3.8, we present a comparison of the wave amplitude evolution for the cases of table 3.2. In figure 3.8a), one can see that for all cases studied, the amplitude follows a similar evolution as the one described in section 3.2. The main differences in terms of amplitude are found for $x/\delta_g \leq 50$, where we see that, for the range of injections conditions under study, the amplitudes are sorted with the dynamic pressure ratio, as detailed by the insert in figure 3.8a). This effect of the dynamic pressure ratio on the near injector amplitude is coherent with the creation of a potential liquid cone that shortens with M (Raynal, 1997). Downstream of this zone, the amplitudes are closer to each other, but clearly follow a linear growth with downstream distance, as predicted by Eq. (3.5). To further examine this zone of linear growth, we present on figures 3.8b) and 3.8c) the evolution of the amplitude at fixed gas Reynolds number, $Re_g = 14667$ and $Re_g = 18000$, respectively, and for the three values of the liquid Reynolds number used in this study. On both of those figures, we add the self-similar growth model, Eq. (3.5), for comparison. The agreement with simulation results is very good. Remarkably, C_0 is constant for all plots, and the differences in the slopes are only due to the change in injection conditions, showing a clear self-similarity of the wave amplitude. This was not the case in the experiments of Marty (2015), where C_0 had to be adjusted to fit the experimental results. This is consistent with our observation of section 3.2: when the wave speed changes, some corrections have to be applied to the velocity scale used in Eq. (3.5). Since all the cases simulated in this section correspond to confinement-induced absolute modes, the wave velocity is close to U_D, which is in agreement with the inviscid mechanism driving the instability (Matas, 2015), therefore no correction

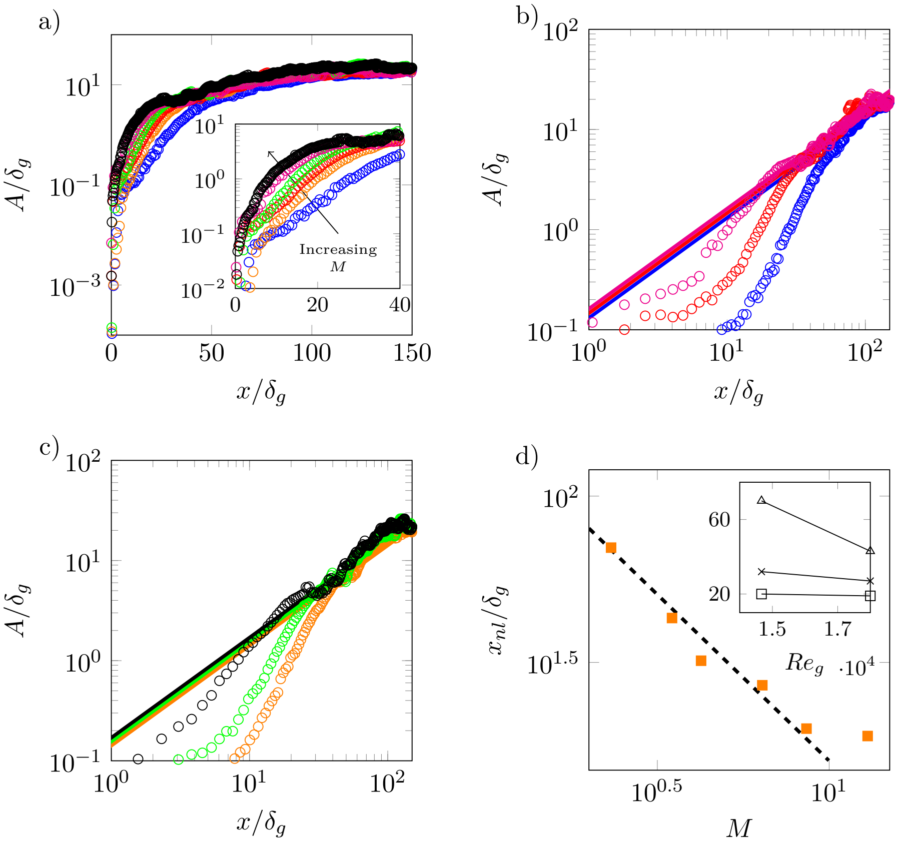

Fig. 3.8 – (Color online) Comparison of wave amplitude for all cases of table 3.2, for $n = 8$. ○:A1, ○:A2, ○:A3, ○:B1, ○:B2, ○:B3. a) evolution of the amplitude for all 6 cases. The insert shows the same data with a zoom in on the inlet area. b) Evolution of the amplitude for $Re_g = 14667$. c) Evolution of the amplitude for $Re_g = 18000$. In b) and c), the solid lines correspond to the self-similar growth model, Eq. (3.5), with the same color code as the symbols and $C_0 = 0.21$. d) □: evolution of the position of entry in the non-linear regime as a function of the dynamic pressure ratio for all cases of table 3.2. The dashed black line corresponds to a $1/M$ scaling. The insert shows the same data plotted as a function of the gas Reynolds number with □: $Re_l = 2600$, ×: $Re_l = 3700$, △: $Re_l = 5000$. Note that in a), b) and c), only 1 data point every 6 is shown to enhance readability.

is needed in the self-similar growth model.

In figure 3.8d) we present the position of entry in the self-similar region as a function of the dynamic pressure ratio. For the range of injection conditions studied here, one can see that the position of entry in the self-similar zone appears to scale as $1/M$. We also plot this position as a function of the gas Reynolds number, which shows that the impact of the liquid Reynolds number increases when the gas Reynolds number is reduced. Note that, in figure 3.5d), one can observe that the decrease of δ_d seems to induce an earlier entry in the non-linear growth region.

In summary, we have demonstrated the agreement between linear theory, simulations, and experiments on wave frequency value in case of confinement modes, which validates the role of confinement in the stability of an air-water mixing layer. We have also shown the consistency between simulations and experiments on wave growth.

3.3 Exploring the effect of confinement

In this section we explore in greater details the effect of gas and liquid stream confinement on the stability of the flow. We first prove that confinement is indeed one of the mechanisms driving the transition between convective and absolute instabilities (along with the interfacial velocity value). We then discuss the effects of confinement, symmetric or non-symmetric, on the characteristics of the instability. For this part, we exclusively study cases A1 and B2. All parameters but H_g and H_l are kept constant and equal to the values used in the previous section. In particular, note that the gas vorticity thickness δ_g is kept constant equal to its value obtained for $H_g = 1$ cm.

Convective/absolute transition

As already said in the introduction, convectively unstable flows behave as noise amplificators, i.e., the response of the system depends on the injected perturbations, whereas absolutely unstable flows behave as oscillators, i.e., the response of the system does not depend on the injected perturbations (Huerre and Monkewitz, 1990).

In order to apply those notions to our study, we first focus on case B2, with $H_g = H_l = H$, i.e., a symmetric confinement. We study two values of H, namely $H = 1$ cm and $H = 0.25$ cm. We show on figure 3.9 that the flow is predicted by linear stability analysis to be absolutely unstable for $H = 1$ cm (•), and convectively unstable for $H = 0.25$ cm ($*$). In case of absolute mode, a pinching occurs at low wavenumber (and positive ω_i) between confinement and shear branches. For the

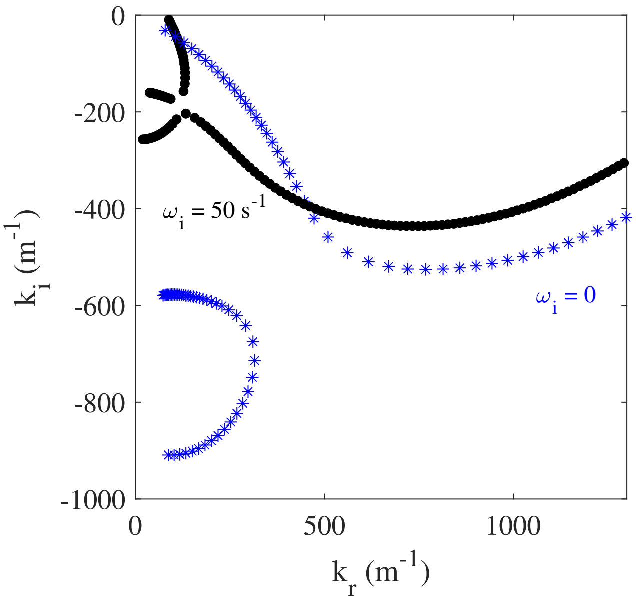

Fig. 3.9 – Spatial branches for case B2. $H = 1$ cm (●) and $H = 0.25$ cm ($*$).

convective mode, the most unstable mode of the shear branch, corresponding to the largest $|k_i|$, is located at a higher wavenumber. For $H = 0.25$ cm ($*$), the confinement branch can be seen close to the imaginary axis but no pinching occurs with the shear branch.

On figure 3.10, we examine the spectrograms of the instability for these two values of H and different injected perturbations. We choose a uniformely random, low-amplitude perturbation (figure 3.10a) and b)), as in the previous section, and a deterministic perturbation $f' = 10^{-3}\sin(2\pi f_{pert}t)$ (figure 3.10c), d), e) and f)), with f_{pert}, the perturbation frequency to be specified later.

One can see that when the mode is predicted to be absolute ($H = 1$ cm, left column of figure 3.10), the spectrograms are barely modified by the injected perturbations. The injected deterministic perturbation can be seen on figures 3.10 c) and e), only very close to the inlet ($x/\delta_g \leq 5$). Further downstream, the flow has its own dynamic, and the most amplified frequency and its variations are not affected by the injected perturbation.

On the other hand, when the mode is predicted to be convective ($H = 0.25$ cm, right column of figure 3.10), the spectrograms look very different depending on the injected noise. In the case of a random, low-amplitude perturbation, shown in figure 3.10b), the most amplified frequency is more difficult to extract as it varies spatially.

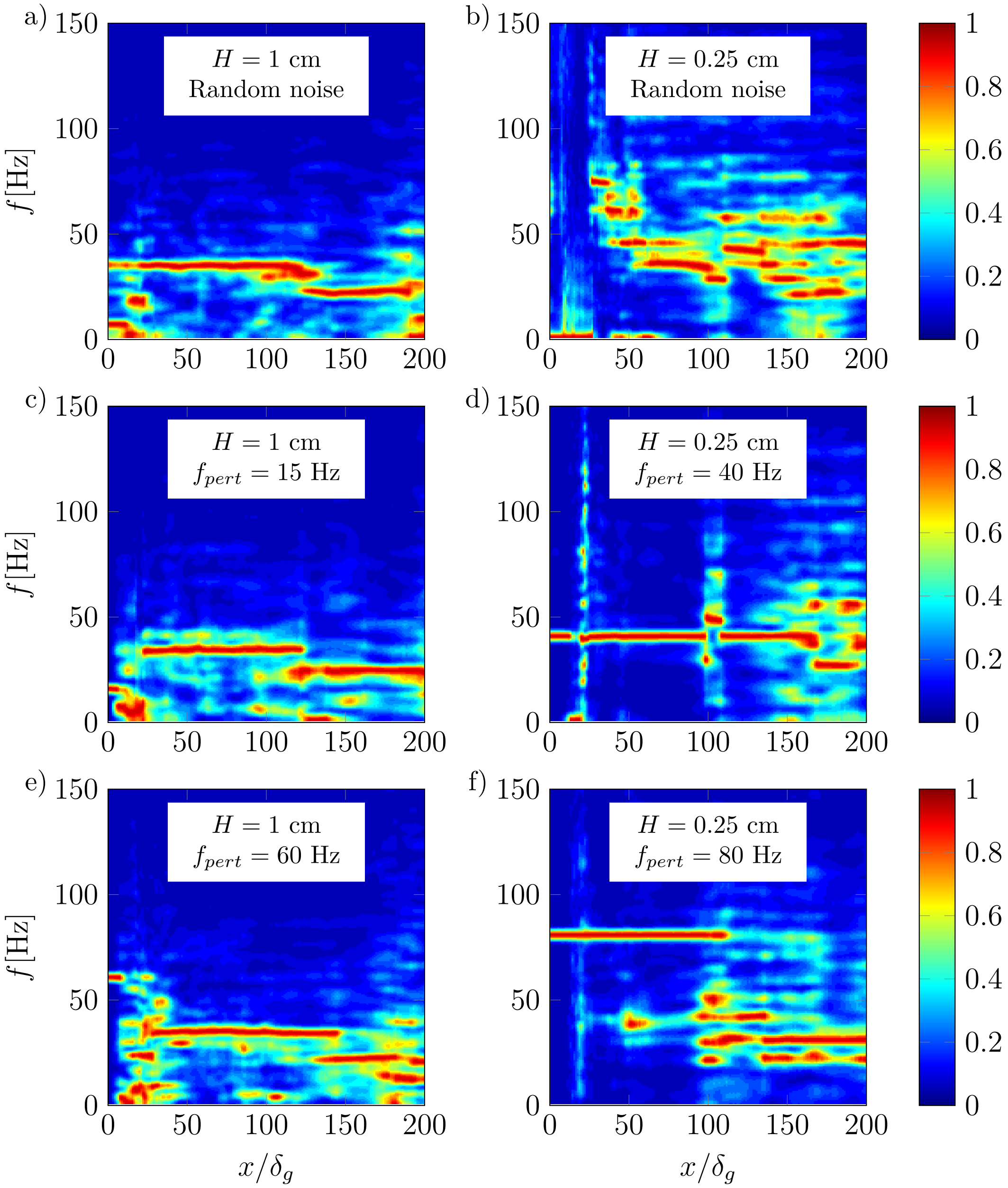

Fig. 3.10 – (Color online) Noise amplificator versus oscillator behaviour. Case B2, $n = 2$. Spectral resolution is 0.56 Hz for all spectrograms. a), c), e): $H = H_g = H_l = 1$ cm and b), d), f): $H = H_g = H_l = 0.25$ cm. a) and b): random noise of amplitude 10^{-5}. c), d), e) and f): deterministic noise of amplitude 10^{-3} and $f_{pert} = 15; 40; 60; 80$ Hz for the cases c), d), e) and f), respectively. The color scale corresponds to the normalized spectral power.

This behaviour had already been seen in Fuster et al. (2009), where it is also said that for the case of convectively unstable flows, the comparison between local linear stability analysis and simulations has to be restricted to the linear growth region, i.e., where the linear stability analysis makes sense. In this area, around $x/\delta_g = 25$, the most amplified frequency is of 73 Hz. Further downstream, the most amplified frequency is progressively decreasing. For the cases with a deterministic perturbation injection, shown in figures 3.10d) and f), one can see that the forcing frequency is the most amplified in more than half of the domain, showing that the stability of the flow does actually depend on the injected perturbation.

Another way to illustrate that we capture a convective/absolute transition driven by confinement is by constructing a spatio-temporal diagram of the interface height, also called Hovmöller diagram, as used in Odier et al. (2015, 2018). As shown on figure 3.9, in the confinement-induced absolute mode, the pinching point occurs at a low wavenumber, whereas in the case of convective mode, the most amplified wavenumber is much higher. This difference can also be seen through the Hovmöller diagram of the instability. On figure 3.11, we show, for case B2 and a random inlet forcing, two spatio-temporal diagrams of the interface height for the same time window and two values of H: $H = 1$ cm (left) and $H = 0.25$ cm (right). One can see that the main difference between both plots is in the wavelength. The waves are much shorter for $H = 0.25$ cm than for $H = 1$ cm which is consistent with the much larger predicted wavenumber for these conditions.

Acccording to the energy budget presented in Matas (2015), the absolute mode induced by confinement is driven by inviscid stresses, whereas the convective mode is driven by viscous stresses. This difference can also be seen by examining the effect of H on the wave speed. On figure 3.11, we add on both plots a magenta line corresponding to a wave speed equal to U_D. For $H = 1$ cm (left figure), this value is in agreement with the numerical result, which may be interpreted as an argument in favour of an inviscid mechanism, as suggested by Matas (2015). On the other hand, for $H = 0.25$ cm (right figure), the agreement between the numerical results and U_D is less favourable.

These three previous arguments (noise amplificator versus oscillator behaviour, wavenumber value, and wave speed) demonstrate that the transition from convective to absolute mode is indeed induced by confinement, as predicted by linear stability analysis, and is fully captured numerically.

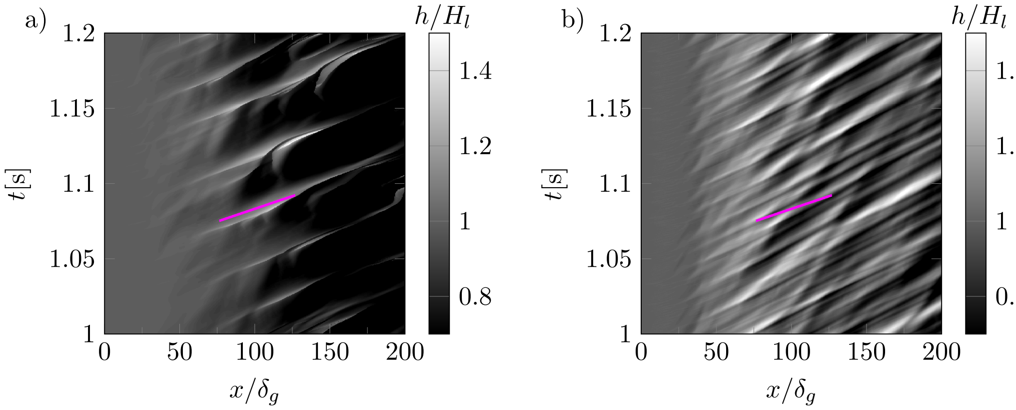

Fig. 3.11 – (Color online) Spatio-temporal diagrams of the interface height. Case B2, $n = 2$ with a low amplitude random forcing at the inlet. a) $H = H_g = H_l = 1$ cm. b) $H = H_g = H_l = 0.25$ cm. The magenta line corresponds to a wave speed equal to U_D, i.e., $U_\phi = U_D = 1.30$ m/s.

Effect of confinement on the stability of the flow

In the previous section we confirmed the transition between convective and absolute modes due to flow confinement. We now study the impact of confinement, symmetric or not, on the characteristics of the instability, i.e., frequency and amplitude. We remind the reader that we focus on cases A1 and B2, where we only vary the thicknesses of the gas and liquid streams, H_g and H_l, respectively, while keeping all other parameters constant. We first start by considering the effect of H for a symmetric confinement, $H_g = H_l = H$, on the most amplified frequency, shown in figure 3.12.

First, one can observe that the overall agreement between linear stability analysis and simulations is very satisfactory, in convective as well as in absolute regimes.

One can observe that, when reducing H, case A1 ($M = 2.32$) presents a transition from absolute to convective regimes for H between 0.75 cm and 1 cm. On the other hand, case B2 ($M = 6.39$) presents the same behaviour for H between 0.25 cm and 0.35 cm. These results suggest that the transition from convective to confinement-induced absolute instabilities does depend on the injection condition, i.e., the value of M, as well as on the confining geometry. In other words, when increasing M, the flow may be absolutely unstable for a larger range of stream thicknesses.

On figure 3.13, we show the evolution of the most amplified frequency in the case of non-symmetric streams, i.e., we keep one stream thickness constant while varying

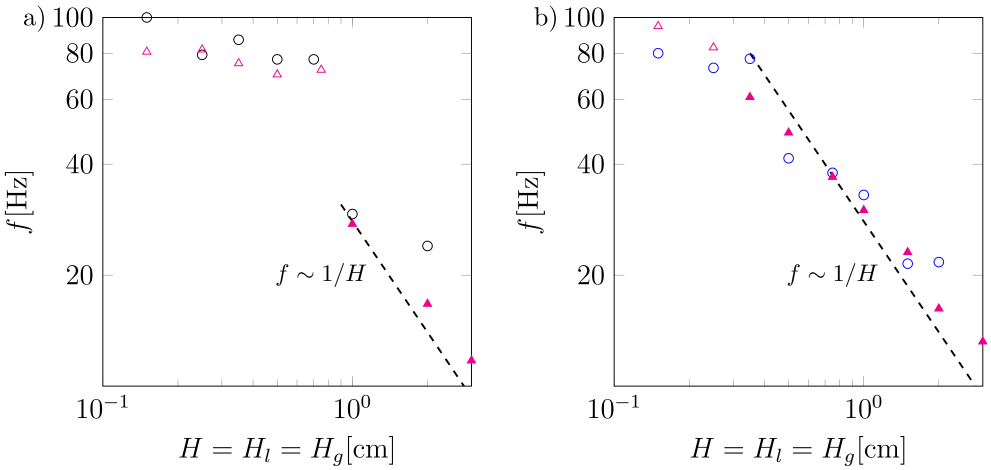

Fig. 3.12 – (Color online) Case of a symmetric confinement: effect of H on the most amplified frequency. $n = 2$. a) ○: simulation results for case A1, b) ○: simulation results for case B2. In both plots the triangles correspond to the frequency predicted by linear stability, with an open symbol for a convective mode and a filled symbol for an absolute mode due to confinement. Spectral resolution is of 0.56 Hz for all simulation results. Dashed lines correspond to a $1/H$ scaling.

the other one. In figure 8 of Matas (2015), it is shown through stability analysis that both thicknesses have symmetric effects on the location of the pinching point, which may be surprising as a flow with a thin gas stream and a large liquid stream could seem very different from a flow with a thick gas stream and a thin liquid stream. Here we do confirm this symmetric behaviour through simulations: one can see on figure 3.13 that in most cases, the results for $H_g = 1$ cm, $H_l = H$ (symbols ○ and ○) and $H_g = H$, $H_l = 1$ cm (symbols □ and □) are in agreement. For $H \leq 1$ cm, the most amplified frequencies are very similar to the ones presented on figure 3.12 for the case of symmetric streams, i.e., $H_g = H_l$. Above $H = 1$ cm, and in case of absolute mode, the most amplified frequency appears to be constant with H, which is not the case for a symmetric confinement (see figure 3.12).

For case A1, $H_g = 1$ cm and $H_l = 2$ cm, as well as for $H_l = 1$ cm and $H_g = 2$ cm, the mode is predicted to be convective, hence the high value (71 Hz) for the frequency predicted by linear stability analysis, whereas for both non-symmetric cases we find numerically a resonance at low frequency (26 Hz). Compared to the case of a symmetric confinement, the fact that a non-symmetric confinement may favour a transition to a convective instability is explained by a decrease in the absolute growth

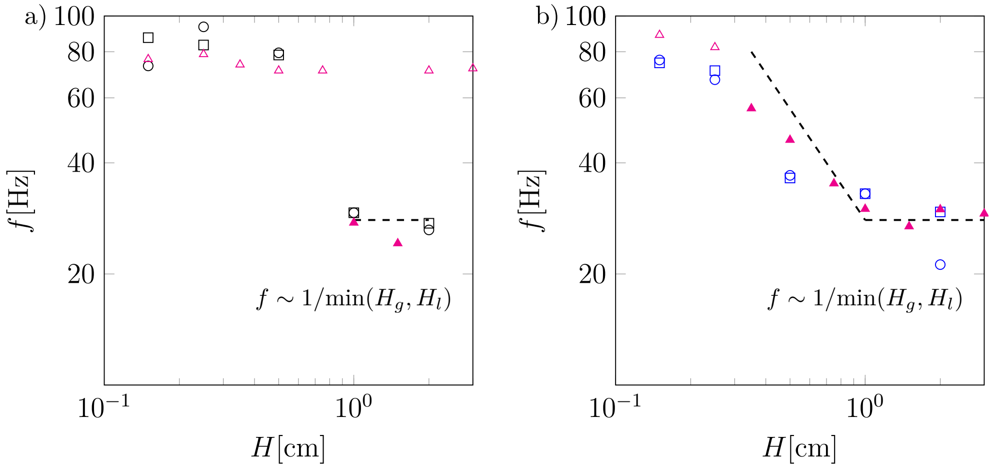

Fig. 3.13 – (Color online) Case of a non-symmetric confinement: effect of H on the most amplified frequency. $n = 2$. a) case A1, ○: simulation results with $H_g = 1$ cm and $H_l = H$, □: simulation results with $H_g = H$ and $H_l = 1$ cm, b) case B2, ○: simulation results with $H_g = 1$ cm and $H_l = H$, □: simulation results with $H_g = H$ and $H_l = 1$ cm. In both plots the triangles correspond to the frequency predicted by linear stability for $H_g = 1$ cm and $H_l = H$, with an open symbol for a convective mode and a filled symbol for an absolute mode due to confinement. The spectral resolution is of 0.56 Hz for all simulation results. Dashed lines correspond to a $1/\min(H_g, H_l)$ scaling.

rate at the pinching point. Indeed, for this case, the pinching between shear and confinement branches occurs at a frequency of 26 Hz, i.e., the value found numerically, but at an absolute growth rate of $-20\ \mathrm{s}^{-1}$. The predicted instability can therefore not be considered as absolute and the value retained for the prediction is therefore that corresponding to the largest $|k_i|$, namely 71 Hz. This discrepancy between numerics and linear stability analysis in the transition from convective to absolute modes may be due to numerical errors (Cossu and Loiseleux, 1998).

Note again that the linear stability results presented in figure 3.13 correspond to the case $H_g = 1$ cm and $H_l = H$, as the symmetric case gives the same result, which has been carefully checked, see also figure 8 of Matas (2015). Even though we simulate extremely small injectors ($H = 1.5$ mm), we do not observe the occurence of a jetting/driping transition, i.e., a transition to an absolute regime driven by the reduction of the liquid Weber number (Clanet and Lasheras, 1999). This may occur for lower liquid velocities, smaller liquid injectors, or for a co-axial atomizer. In such

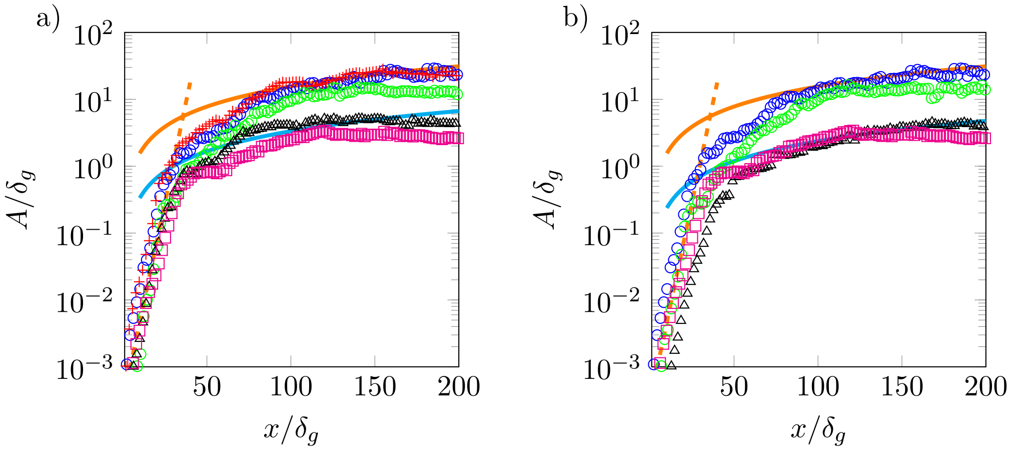

Fig. 3.14 – (Color online) Effect of confinement on the amplitude for case B2 with $n = 2$. a) Effect of the reduction of H for a symmetric confinement ($H_g = H_l = H$). +: $H = 2$ cm, ○: $H = 1$ cm, ○: $H = 0.5$ cm, △: $H = 0.25$ cm, □: $H = 0.15$ cm. b) Evidence of the non-symmetric effect of the gas and liquid thicknesses on the amplitude. ○: $H_l = H_g = 1$ cm, ○: $H_g = 0.15$ cm and $H_l = 1$ cm, △: $H_l = 0.15$ cm and $H_g = 1$ cm, □: $H_l = H_g = 0.15$ cm. In both plots, only 1 data point every 4 is shown to enhance readability. ···: Eq. (3.4), with $A_0/\delta_g = 0.0003$ and $k_i = 614.6\text{m}^{-1}$. —: Eq. (3.5), with $C_0 = 0.21$. —: Eq. (3.5), with a): $C_0 = 0.045$, and b): $C_0 = 0.032$.

regime one may loose the symmetry of the role played by gas and liquid thickness.

One important observation is that the gas stream thickness, H_g, has its own effect on the instability via the triggering of this absolute instability. It does not only affect the instability through its effect on the gas vorticity thickness δ_g, unlike what has been observed in Matas et al. (2011) based on the results of Ben Rayana (2007). However, both effects are related in the experiments and controlling one independently of the other may not be technically feasible.

On figure 3.14, we present the effect of confinement on wave amplitude. We start by studying on figure 3.14a) the effect of a reduction of H for a symmetric confinement, from $H = 2$ cm (+) to $H = 0.15$ cm (□). One can see that the reduction of H induces a global decrease of the amplitude in the downstream region. The growth close to the inlet, i.e., $x/\delta_g \leq 25$, does not seem to be affected until the amplitude is on the order of the gas vorticity thickness. Further downstream, the lower the value of H, the earlier the amplitude seems to depart from the self-similar growth model, and stabilize up to a constant value increasing with H.

To clarify the effect of each stream thickness on the wave amplitude, we present on figure 3.14b) the effect of a reduction of H_g only (○), H_l only (△), and both (□). One can see that, although the effect of both stream thicknesses on the frequency is symmetric, the effect on the amplitude is non-symmetric. It seems that the decrease in amplitude observed in figure 3.14a) between $H = 2$ cm (symbol +) and $H = 0.15$ cm (symbol □) is mainly due to the decrease of H_l since the same decrease is observed when only H_l is reduced (symbol △ in figure 3.14b). It also seems that when H_l only is reduced, the growth is slower in the region close to the injector, which agrees with the experimental observations of Marty (2015).

Similarly, the departure from the self-similar model seems to be due to the reduction of H_g. Following the derivation of the self-similar model in Hoepffner et al. (2011), the amplitude increase is due to the aerodynamic suction created by the acceleration in the gas stream above the wave. When the wave amplitude becomes large compared to the gas stream, there is no longer a sufficient acceleration to induce wave growth.

Scaling law for confinement modes

The destabilizing effect of confinement has been demonstrated and explored by means of numerical simulations and linear stability analysis in previous subsections. In Matas et al. (2018), a scaling law derived from the linearized equations was proposed for the wave frequency in confinement-induced absolute modes,

$$f \sim \frac{\sqrt{\frac{\rho_g}{\rho_l}\frac{\delta_l}{\delta_g}}U_g + U_l}{L}, \tag{3.6}$$

where L is a characteristic length related to the confinement. This scaling has recently been found to account very well for the effect of the nozzle size in experiments on a co-axial configuration (Singh et al., 2020). Eq. (3.6) predicts a linear evolution of the frequency with the liquid velocity, which has been observed experimentally (Matas et al., 2011; Singh et al., 2020). In the case of large gas velocity, $\delta_g \ll \delta_l$, and for δ_g varying as $U_g^{-1/2}$, the frequency is proportional to $U_g^{5/4}$, which is close to the scaling predicted by inviscid theory (Raynal, 1997; Marmottant and Villermaux, 2004), see section 1.1. Note that the scaling of Eq. (3.6) is only valid for absolute modes due to confinement.

In order to compare our results to the scaling of Eq. (3.6), we add lines enhancing the scaling of the frequency with H in absolute regimes on figure 3.12. In confinement-induced absolute regime, we find that the most amplified frequency follows a $\sim 1/H$ scaling in the case of symmetric confinement. For $H_g \neq H_l$, as seen in figure 3.13, it seems that the frequency scales with the most restrictive confining length, i.e.,

$$f \sim 1/\min(H_g, H_l). \tag{3.7}$$

Thus, our results match very well with the scaling of Eq. (3.6) and we evidence that L is of the order of the smallest injector size. This is different from what has been observed experimentally by Delon et al. (2018) for a co-axial geometry, where the frequency is found to always scale with $1/H_l$. The shear branch being barely affected by the value of H, frequency is expected to be independent of the confining size in the convective regime.

3.4 Transition from primary to secondary instability

As said in the first chapter of this thesis, liquid ligaments generation is mainly due to a Rayleigh-Taylor instability triggered by liquid acceleration under aerodynamic stresses induced by gas jet. In order to go further in the study of the stability of an air-water mixing layer, by extracting informations about ligaments generation while keeping computational time to a reasonable level, we carry two studies. The first one is dedicated to a "classic" Rayleigh–Taylor instability and allows us to define a resolution requirement to accurately simulate such instability. The second study is focused on wave acceleration measurements, in the configuration studied previously, which are then compared to experimental results.

Rayleigh–Taylor instability

We study here the ability of our solver to predict the temporal growth of a "classic" Rayleigh–Taylor instability where a liquid layer of density ρ_l is located above a fluid of density ρ_g. Viscosity is not taken into account. Surface tension is the same as in the air-water case (see table 3.1 for physical properties values). At $t = 0$, the interface between both fluids is perturbed by a cosinusoidal deformation of low amplitude β, namely $\beta = 10^{-4}$ m. $\lambda_{rt} = 2\pi/k_r$ is the perturbation wavelength. Gravity is taken into account and is oriented from top to bottom. Application of linear stability analysis methodology to this problem leads to the following dispersion relation (Charru, 2012)

$$(\rho_l + \rho_g)\omega^2 - \big((\rho_g - \rho_l)gk_r + k_r^3\sigma\big) = 0, \tag{3.8}$$

where $g = 9.81$ m/s^{-2} is the gravity acceleration norm. For a temporal resolution, ω is complex and finding the roots of Eq. (3.8), solved for ω, depending on the different parameters values gives informations on flow stability.

For $\rho_g > \rho_l$, the roots are reals and there is no temporal amplification of perturbations.

For $\rho_l > \rho_g$, several cases can be distinguished. For $k_r > l_c$, with $l_c = \sqrt{\sigma/(g|\rho_l - \rho_g|)}$ the capillary length, or cut-off length, the roots are reals and the perturbation is not amplified. In this case, the destabilizing effect of gravity is damped by the restoring effect of capillarity. For $k_r < l_c$, the roots are purely complexes and the unstable

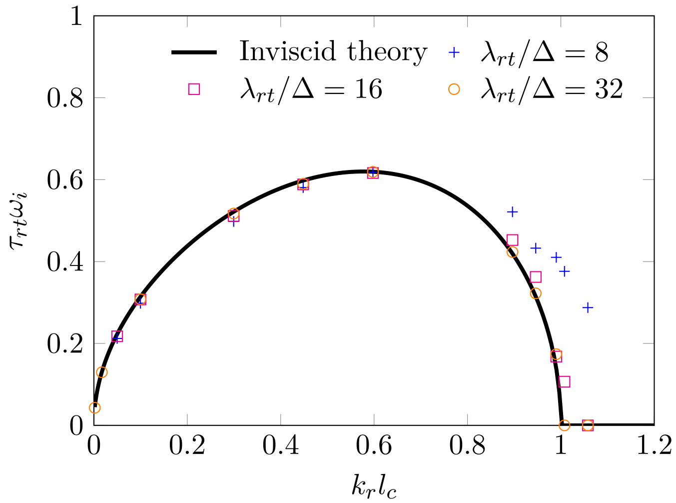

Fig. 3.15 – Rayleigh–Taylor instability: comparison of growth rate predicted by linear stability analysis to growth rate obtained by numerical simulation for different mesh resolutions.

mode grows with a rate

$$\tau_{rt}\omega_i = \sqrt{\left(\frac{\rho_l - \rho_g}{\rho_l + \rho_g}\right) k_r l_c \,(1 - k_r^2 l_c^2)}, \tag{3.9}$$

with $\tau_{rt} = \sqrt{l_c/g}$ the characteristic time. In order to confront our numerical results to the previous prediction, we simulate this configuration on a numerical domain of size $0 \leq x \leq \lambda_{rt}$, $0 \leq y \leq 10\lambda_{rt}$, discretized with a uniform cell size Δ to be prescribed. The growth rate is obtained from the temporal evolution of interface position by least-squares minimization. Physical properties correspond to the air-water case with zero viscosities.

Results are shown in figure 3.15, where we compare temporal growth rate obtained numerically for different resolutions and wavenumbers to the prediction of Eq. (3.9). One can see that for $\lambda_{rt}/\Delta = 8$, i.e., when resolution corresponds to eight cells per wavelength, growth rate is accurately captured for the smallest wavenumbers but not close to cut-off length. This might be due to errors in curvature computation. With such a resolution, waves smaller than cut-off length are amplified in time. As soon as the resolution corresponds to $\lambda_{rt}/\Delta = 16$, the error on the cut-off length is of less than 5%. With $\lambda_{rt}/\Delta = 32$, the growth rate obtained numerically matches the prediction. We should therefore recommand a resolution $\lambda_{rt}/\Delta = 16$ for accurate simulation of such instability. Note that better curvature computation methods could lead to better numerical prediction of growth rate close to cut-off length with lower resolution.

One can compare the value $\lambda_{rt}/\Delta = 16$ obtained by the present analysis to the resolution used previously for primary wave simulations. We remind that for primary wave simulations, resolution was taken as a function of gas vorticity thickness with $\Delta = \delta_g/n$. One therefore obtains $n = 16\delta_g/\lambda_{rt}$. From Ben Rayana (2007), the relation between Sauter Mean Diameter D_{32} and transverse wavelength is $D_{32} \approx 0.1\lambda_{rt}$. The Sauter diameter of a particle is the diameter of a sphere that has the same volume to surface ratio as the particle under study (in our case a water droplet). The Sauter Mean Diameter (SMD) is one of the quantities used to characterize the performance of an atomizer. n can thus be estimated as

$$n \approx 1.6\delta_g/D_{32}. \tag{3.10}$$

The quantity D_{32}/δ_g is available from drop sizes measurements of Marty (2015). For $H_g = H_l = 1cm$, $M = 16$ and U_g in the range $[20; 60]$ m/s, one obtains n in the range $[1.56; 9.45]$, with n increasing quadratically with U_g. For cases without velocity deficit, $n = 8$ allows resolution of primary wave as well as of Rayleigh–Taylor instability. In the instability cascade, wave acceleration is induced by aerodynamic stresses. One can therefore wonder how to measure this acceleration and which resolution is needed to correctly capture it. The following section gives some first attempts in this direction.

Note that the results presented in the present section do not include viscous effects. For the air-water case, viscous effects are negligible. We also carried a validation of the numerical solver for cases where viscous effects are important (results not shown) that confirmed the conclusion drawn above concerning the minimal resolution to accurately resolve the "classic" Rayleigh–Taylor instability. The only additional difficulty induced by the presence of viscous effects is that additional restrictions must be applied on the simulation time step (even with an implicit resolution of viscous terms) so that viscous errors are not amplified in time.

Wave acceleration

As said previously, we give here the result of our explorations concerning wave acceleration measurements and the comparison of numerical results to models and experimental results. The configuration used for numerical simulations is the one described in section 3.1 (viscous effects are included). The dynamic pressure ratio is kept equal to 4 and gas and liquid velocities are varied in order to change the Weber number based on gas vorticity thickness $We_{\delta_g} = \rho_g(U_g - U_D)^2\delta_g/\sigma$. Quantities related to secondary instability are classicaly presented as a function of We_{δ_g} (Marmottant and Villermaux, 2004; Varga et al., 2003; Ben Rayana, 2007; Marty, 2015).

Acceleration measurements could be done in many different ways, e.g., direct computation of a Lagrangian acceleration field or seeding of the interface with marker points. Here we rather use a simple strategy based on spatio-temporal diagrams of interface height. In section 3.3, these diagrams are constructed using the lowest interface position, i.e., if along the vertical direction at a given downstream position, several interfaces are found, interface position is taken as the vertical coordinate of the lowest interface. If, on the other hand, one uses the third interface position as interface height in case of multiple interfaces, one can follow the dynamic of the thin liquid sheet formed by wave crest under aerodynamic stresses.

An example of spatio-temporal diagram obtained with such method is shown in figure 3.16a). One can see that in the downstream area, i.e., $x > 80\delta_g$, some paraboloids are appearing. These paraboloids correspond to an acceleration in the x direction, which is the source of transverse instability. The acceleration is then measured by fitting a two-dimensional paraboloid onto the diagram each time such acceleration is seen. No efficient way to automatize paraboloid extraction and fitting operation has been found. These operations are simply done by arbitrarily picking up three points coordinates on the paraboloid, whose coefficients are then found by linear system resolution. This operation is repeated for a large number of waves (usually between 20 and 30) until the averaged acceleration $\langle a \rangle_t$ does not exhibit variations of more than 10%. Repeating this process for different injection conditions and injector geometries with a moderate resolution ($n = 2$), we obtain the results presented in figure 3.16b).

The acceleration is found to increase with We_{δ_g}, and a decrease of H_l induces an increase of wave acceleration. One can estimate the transverse wavelength λ_T as the most amplified wavelength of Rayleigh–Taylor instability, i.e.,

$$\lambda_T = 2\pi\sqrt{\frac{3\sigma}{\rho_l\langle a \rangle_t}}. \tag{3.11}$$

As $D_{32} \approx 0.1\lambda_T$ (Ben Rayana, 2007), one can therefore compare D_{32}/δ_g estimated from acceleration measurements to the experimental results of Marty (2015), as shown in figure 3.16c). One can see that the results seem closer to the $We_{\delta_g}^{-1}$ scaling than to $We_{\delta_g}^{-1/2}$ scaling, and that values obtained for D_{32}/δ_g from acceleration measurements are slightly higher than experimental values.

Acceleration was found to increase with mesh resolution, thus inducing a reduction of estimated D_{32}/δ_g, but its variations from one wave to another were also

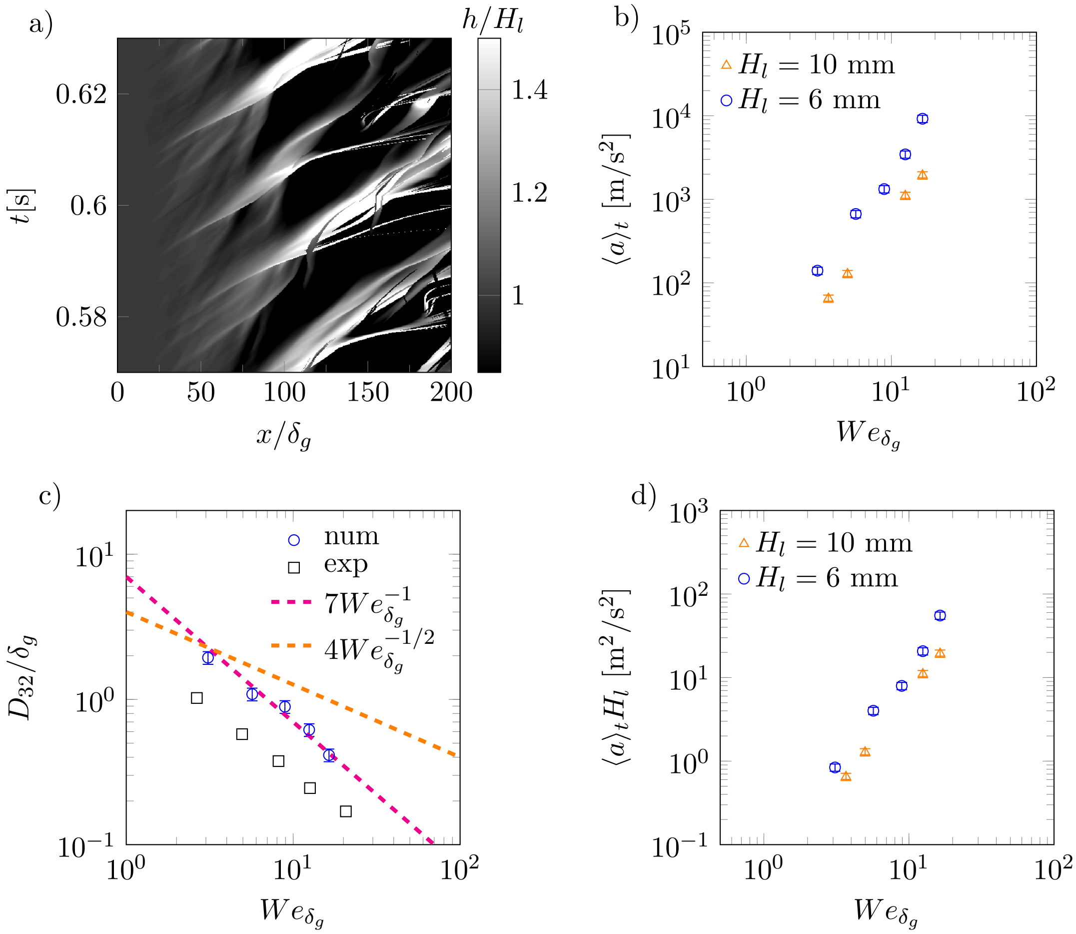

Fig. 3.16 – Wave acceleration measurements. a): spatio-temporal diagram of interface height for $H_g = H_l = 1$ cm, $M = 4$, $U_g = 40$ m/s, $n = 2$. b): evolution of measured wave acceleration with We_{δ_g} and two values for H_l. $H_g = 1$cm, $M = 4$, $n = 2$. c): comparison between experimental D_{32} values (Marty, 2015) and D_{32} deduced from acceleration measurements. The numerical results in c) correspond to the $H_l = 6$ mm case used in figure b). The experimental results are obtained for $M = 4$, $H_g = 1$ cm, $H_l = 6$ mm. d): same data as in b) but with mean acceleration multiplied by liquid injector size. In b) and d), the error bars correspond to the 10% uncertainty on mean acceleration value. In c), the error bars correspond to a 5% uncertainty due to the propagation of mean acceleration value uncertainty.

found to increase, requiring longer simulations to obtain a converged averaged acceleration. This last point might be due to a two-dimensional turbulence effect. We have therefore not performed further computations with the aim of measuring wave acceleration. A three-dimensional mesh convergence would be needed to check the dependency of results to mesh resolution and to the two-dimensional nature of present simulations. Despite simplicity of measurement method and moderate resolution, good agreement is obtained between simulations and experiments on the values of wave acceleration through the value of D_{32}/δ_g.

Finally, our numerical results and the experimental results of Marty (2015) can be compared to the literature. In Ben Rayana (2007) and Hong et al. (2003), D_{32}/δ_g scales as $We_{\delta_g}^{-1/2}$, whereas our results seem closer to a $We_{\delta_g}^{-1}$ scaling, as observed by Marty (2015). Following Marty (2015), the difference in experimental results might be explained by differences in optical measurement devices.

Focusing now on acceleration modeling, we first recall that the model of Varga et al. (2003) starts from an aerodynamic force balance,

$$a = \frac{F_d}{m_w} = \frac{C_d \rho_g \left(U_g - U_D\right)^2 A_w}{2 \rho_l A_w b} \tag{3.12}$$

where F_d is the aerodynamic force exerted by the gas on the wave, m_w is the mass of liquid accelerated by the gas, C_d is the wave drag coefficient, A_w is the wave area and b is the wave base thickness. b is assumed to be a fraction of primary wavelength, i.e., $b = \gamma\lambda$, with γ a model coefficient between 0 and 1. Following Raynal (1997) and Eq. (1.17)-(1.18), for large U_g the primary wavelength λ_{Ray} scales as

$$\lambda_{Ray} \sim \delta_g, \tag{3.13}$$

which gives the following scaling for acceleration

$$a_{Ray} \sim \frac{C_d}{\gamma} \left(U_g - U_D\right)^2 \delta_g^{-1}. \tag{3.14}$$

Similarly, combining Eq. (3.6) and Eq. (1.18), for large U_g the following scaling can be obtained for primary wavelength

$$\lambda_{Mat} \sim L\sqrt{\delta_g}, \tag{3.15}$$

which finally gives the following scaling for acceleration

$$a_{Mat} \sim \frac{C_d}{L\gamma} \left(U_g - U_D\right)^2 \delta_g^{-1/2}. \tag{3.16}$$

The scaling for a_{Mat} involves an inversely proportional relation to L, and is only valid for confinement-induced absolute modes. As shown in the previous section, as L scales with the smallest injector size, a reduction of H_g or H_l should induce an increase of acceleration. This corresponds to the results of figure 3.16b), where a decrease of H_l induces an increase of acceleration. In Marty (2015), a reduction of H_l is found to induce a decrease of D_{32}, therefore an increase of acceleration.

To further test the scaling of Eq. (3.16) for injector size effect, we plot in figure 3.16d) the quantity $[\langle a \rangle_t \times H_l]$ for the data series of figure 3.16b). The series are very close, even though not perfectly collapsed, suggesting that the scaling of Eq. (3.16) for injector size effect is correct. However, note that we have not studied the effect of H_g on acceleration. In Ben Rayana (2007), H_g is found not to have any other effect on D_{32} than through its effect on δ_g.

In figure 3.16c), the quantity D_{32}/δ_g seems to scale as $We_{\delta_g}^{-1}$. The corresponding scaling for acceleration with injection velocities is

$$a \sim (U_g - U_D)^4 \,. \tag{3.17}$$

Thus, except a correct prediction of the effect of H_l with the scaling of Eq. (3.16), in case of constant C_d and γ, and δ_g varying as $U_g^{-1/2}$, none of the proposed scalings can predict the good dependency to injection velocities. Non-constant C_d and γ with injection velocities might be the reason for the discrepancy between models and measurements for wave acceleration, as already suggested by Marty (2015). Numerical simulations could be a solution to measure γ and to deduce the variations of C_d with injection velocities from the scaling of Eq. (3.16). This is left to future work.

Note also that for D_{32}/δ_g scaling as $We_{\delta_g}^{-1/2}$, as found by Ben Rayana (2007); Hong et al. (2003), the scaling of Eq. (3.14) with injection conditions is correct, but does not involve any dependency to injector sizes.

Size	2D	$L_z = H_l$	$L_z = 3H_l$	$L_z = 6H_l$
$\Delta T f_{th}$	50	30	24	9
n_{cells}	1.4×10^5	6.6×10^6	20×10^6	40×10^6

Table 3.3 – Comparison between 2D and 3D simulations for case $B1$, $\delta_d = 1$, $n = 2$, $H_g = H_l = 1$ cm. Summary of transverse domain size, normalized sampling time, and number of cells.

3.5 Comparison between 2D and 3D simulations

In this section we present a comparison between two-dimensional and three dimensional simulations for the same $B1$ case, see table 3.2, without interfacial velocity deficit and for different transverse domain size. The different domain widths, sampling time, and number of cells for each of the simulations are summarized in table 3.3. The domain is uniformely discretized in the transverse direction with a cell size equal to δ_g/n. Periodic boundary conditions are applied in the transverse direction. Interface position is recorded during a time equal to $\Delta T f_{th}$, see table 3.3 for the values of $\Delta T f_{th}$ for each case, at all downstream positions and at $z = L_z/2$.

The objective is to provide qualitative and quantitative comparisons between 2D and 3D simulations, in order to evaluate the dependency of the results presented previously to the two-dimensional nature of simulations, and to provide a study of the dependency of the flow and instability characteristics to transverse domain size, which is an essential step before three-dimensional mesh convergence. We follow different steps: we first compare flow visualizations, then instability characteristics, and we finally compare mean flow statistics.

Visualization

In order to perform a qualitative comparison concerning the effect of the three-dimensional nature of the flow on interface deformations, we show a comparison of flow pictures for the different cases of table 3.3 at the same time, $t = 344$ ms, in figure 3.17. Note that here the comparison is done at one single instant but the observations presented hereafter are valid for the whole simulations. One can see that the three-dimensional case with the smallest transverse size (figure 3.17b) does not exhibit significant transverse deformations. The level of transverse deformations increases for $L_z = 3H_l$ (figure 3.17c) but no ligaments generation can be seen on this picture. On the other hand, for the largest domain size, corresponding to $L_z = 6H_l$ (figure 3.17d), a clear generation of liquid ligaments is seen. This seems to correspond

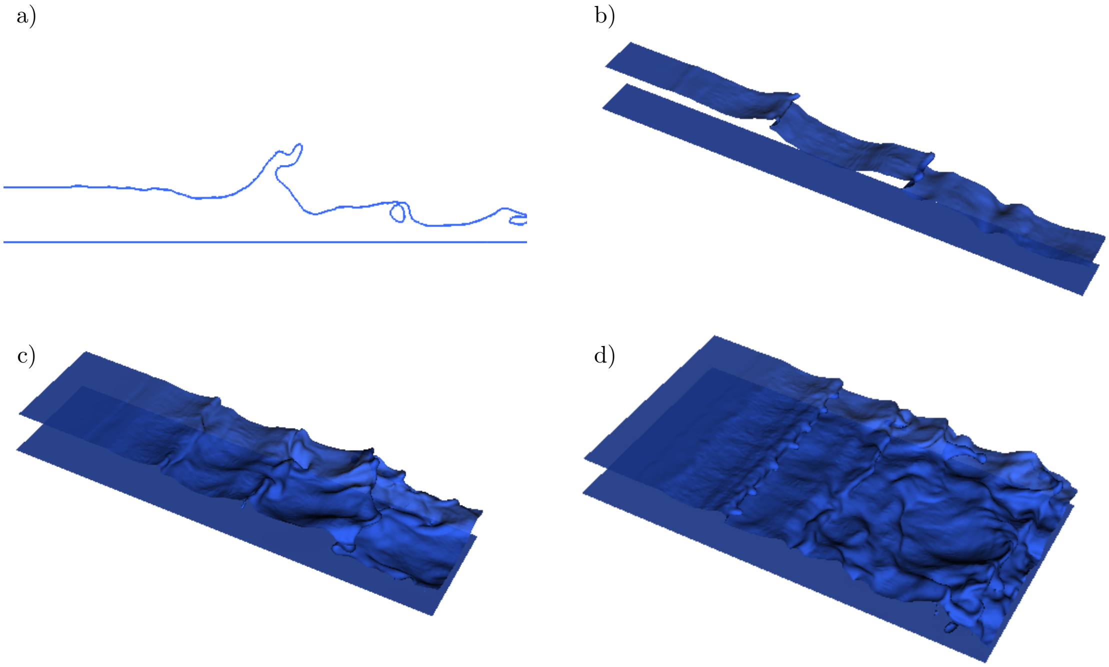

Fig. 3.17 – Comparison of interfacial deformations for different transverse domain sizes at $t = 344$ ms. $B1$ case, $\delta_d = 1$, $n = 2$, $H_g = H_l = 1$ cm. a) 2D simulation, b) $L_z = H_l$, c) $L_z = 3H_l$, d) $L_z = 6H_l$.

to a Rayleigh–Taylor instability induced by wave acceleration. Indeed, the spatio-temporal diagram of interface height confirms the presence of acceleration during liquid ligaments generation, see figure 3.18. Using the method presented in section 3.4 we obtain

$$a_{3D} = 67\text{m/s}^2, \tag{3.18}$$

which, as for this case $We_{\delta_g} = 4.87$, is in agreement with the values presented in figure 3.16b). This value can be used to get an estimation of the most amplified wavelength of Rayleigh–Taylor instability, Eq. (3.11),

$$\lambda_{T,est} = 2\pi\sqrt{\frac{3\sigma}{\rho_l a_{3D}}} = 1.13\text{cm}. \tag{3.19}$$

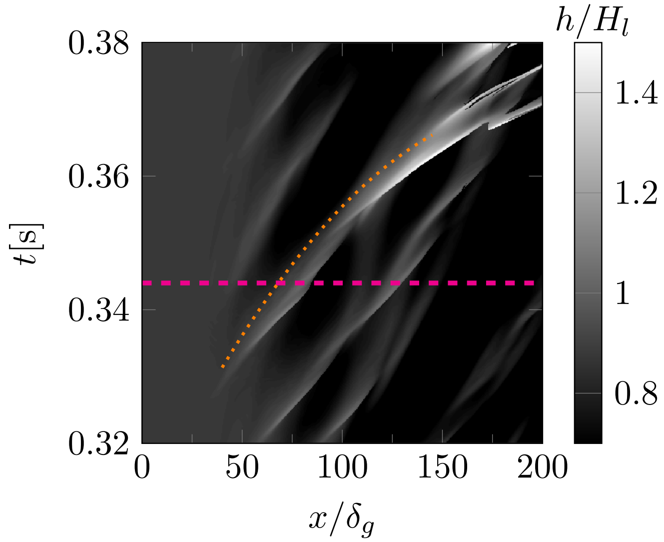

Fig. 3.18 – Evidence of acceleration during ligaments generation. $B1$ case, $\delta_d = 1$, $n = 2$, $H_g = H_l = 1$ cm, $L_z = 6H_l$. The magenta dashed line indicates $t = 344$ ms. The orange dotted line corresponds to $x = 0.5at^2 + bt + c$, with $a = 67$, $b = -21.93$, $c = 3.597$.

This value can be compared to a measured averaged transverse wavelength computed using the number of liquid ligaments seen in figure 3.17d), i.e.,

$$\langle \lambda_{T,meas} \rangle_z = \frac{L_z}{7} = 0.86\text{cm}. \tag{3.20}$$

Both values are in good agreement, even though the prediction using acceleration value is slightly higher than the value based on visual observation. This discrepancy might be explained by an erroneous measure for acceleration, by transverse domain size effect, or by the fact that the transverse wavelength due to a Rayleigh-Taylor instability may, in the absence of controlled forcing, be different from the most amplified frequency predicted by the model. This result is nonetheless a strong argument in favour of a model for transverse destabilization based on Rayleigh–Taylor instability. Note that for the widest domain ($L_z = 6H_l$), only one event of such a clear ligament generation has been seen, probably beacause of a too short simulation time. For $L_z = 3H_l$, several ligaments generation have been seen, but with a less clear wavelength compared to what is shown in figure 3.17d). One can also see in figure 3.18 that not all waves undergo acceleration.

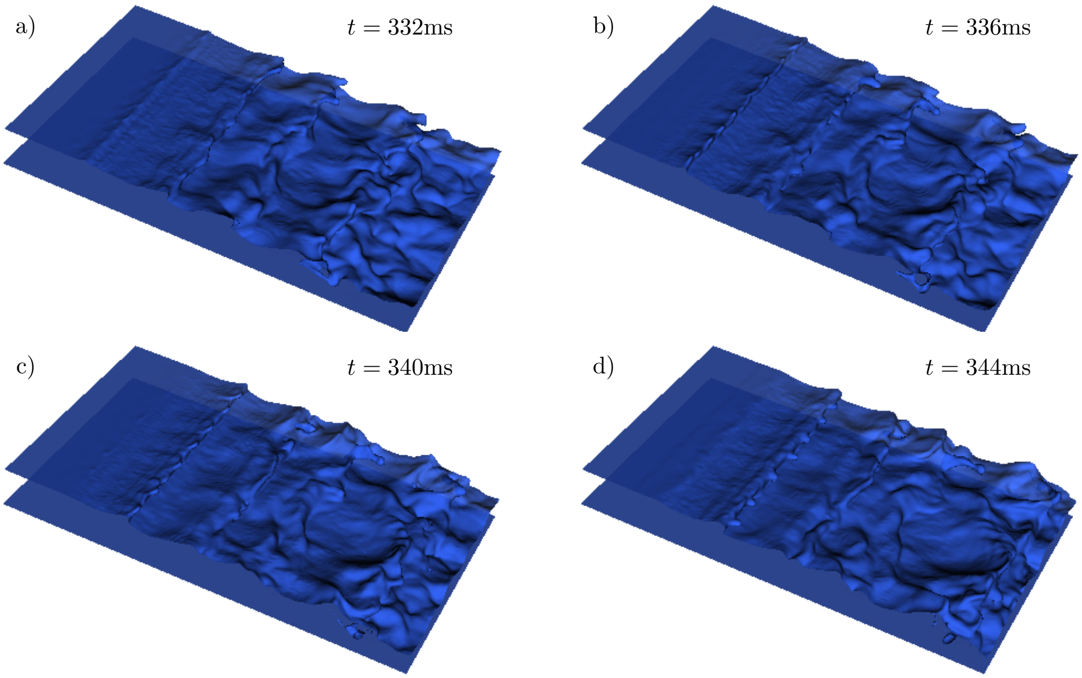

Fig. 3.19 – Visualization of ligaments generation. $L_z = 6H_l$, $B1$ case, $\delta_d = 1$, $n = 2$, $H_g = H_l = 1$ cm. a) $t = 332$ ms, b) $t = 336$ ms, c) $t = 340$ ms, d) $t = 344$ ms.

To complete previous observations on ligaments generation, we present in figure 3.19 a serie of flow pictures at succesive instants for the widest domain. One can observe wave formation and growth (figure 3.19 a-b) followed by transverse destabilization (figure 3.19 c) leading to ligaments generation (figure 3.19 d). We show a side view of ligaments generation for similar instants in figure 3.20. One can see that ligaments are indeed oriented in the axial direction, i.e., the direction in which acceleration occurs. One can also see that shortly after their generation, ligaments are falling down in the liquid and do not further desintegrate into droplets, as would have been expected in the instability cascade. This might be due to a lack of resolution that prevents resolution of capillary instability leading to droplets generation.

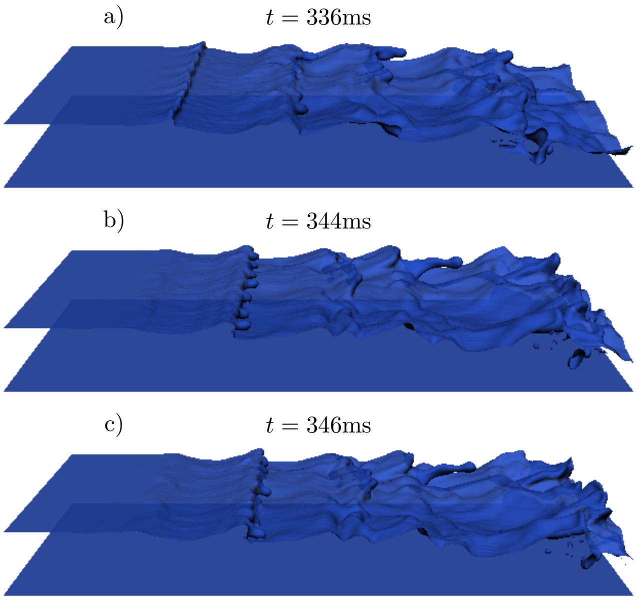

Fig. 3.20 – Side view of ligaments generation. $L_z = 6H_l$, $B1$ case, $\delta_d = 1$, $n = 2$, $H_g = H_l = 1$ cm. a) $t = 336$ ms, b) $t = 344$ ms, c) $t = 346$ ms.

Instability characteristics

We now turn to the comparison of instability characteristics. In order to compare the spatio-temporal development of the instability for all cases, we show in figure 3.21 the Hovmöller diagrams of interface height (constructed using the first interface position along vertical direction) for each case. On each plot we add a magenta line corresponding to a phase velocity equal to U_D. One can see that wave velocity is not affected by domain width and is in close agreement with U_D. On the other hand, one can observe that wavelength is shorter for the three-dimensional cases than for the two-dimensional simulation. This results in a wave frequency higher in 3D than in 2D. Note that all 3D simulations have the same wavelength and frequency.

This discrepancy could be explained by the impact of downstream turbulence rate in the gas phase. Indeed, although there is no turbulence injection at the inlet of the domain, turbulence quickly developped in gas phase, as we will see in the following subsection. As shown by Matas et al. (2015); Jiang and Ling (2020) and in chapter 1, a turbulence rate of 10% can double wave frequency compared to a case where there is no turbulence in gas phase. In 3D, the diffusion due to turbulence is higher than in 2D, which could explain why the effect of turbulence is seen in 3D but not in 2D, even though turbulence rates are similar. We remind the reader that increased turbulent diffusion is the source of the impact of gas phase turbulence on primary instability as it lowers the energy feeding the resonance leading to absolute instability (Matas et al., 2015) .

Another possibility for this discrepancy could be an increased level, in 3D compared to 2D, of numerical errors in curvature computation or in mass/momentum advection. In Agbaglah et al. (2017), frequency value is the same in 2D and 3D, but their configuration includes a splitter plate between gas and liquid streams. One can imagine that the splitter plate could impact frequency selection through a 3D mechanism but this is not documented in the literature. The presence of a splitter plate also induces higher wave amplitude in the near-injector region than for our configuration (results not shown), which could result in a lower influence of numerical errors, in 3D, for the configuration of Agbaglah et al. (2017). This discrepancy should be confirmed, or not, by mesh convergence in future work. Nonetheless, this reinforces the interest for 2D simulations as they allow a better control of the different parameters at play behind the stability of an air-water mixing layer.

Downstream of the flow, i.e., $x > 150\delta_g$, wavelength is increasing in 2D as well as in 3D. This shows that the appearance of low frequency peaks in this area, as seen in section 3.2, is not due to the 2D nature of the flow. We have carefully checked that this is not induced by outlet boundary condition type and position. This might be due to an incomplete atomization of waves due to a lack of resolution, or to the emergence of another mode of instability triggered by base flow variations. Mesh convergence and global linear stability would be useful to go further in this study, but this is left to future work.

In figure 3.22 we compare wave amplitude for all cases of table 3.3. Similarly to what has been done in previous sections, we add for reference the exponential growth obtained experimentally for this case (Matas et al., 2011), and the self-similar growth model of Hoepffner et al. (2011), Eq. (3.5), with $C_0 = 0.21$, as in previous sections for $\delta_d = 1$. One can see that no significant difference can be observed between cases. For each case, amplitude is first growing exponentially, in agreement with the growth rate found experimentally, then growing linearly with downstream distance, in agreement with self-similarity of waves.

Flow statistics

Finally, we provide a comparison between two-dimensional and three-dimensional mean flow quantities. The goal is not to perform an exhaustive comparison of flow statistics between all cases, but rather give some elements allowing to evaluate on

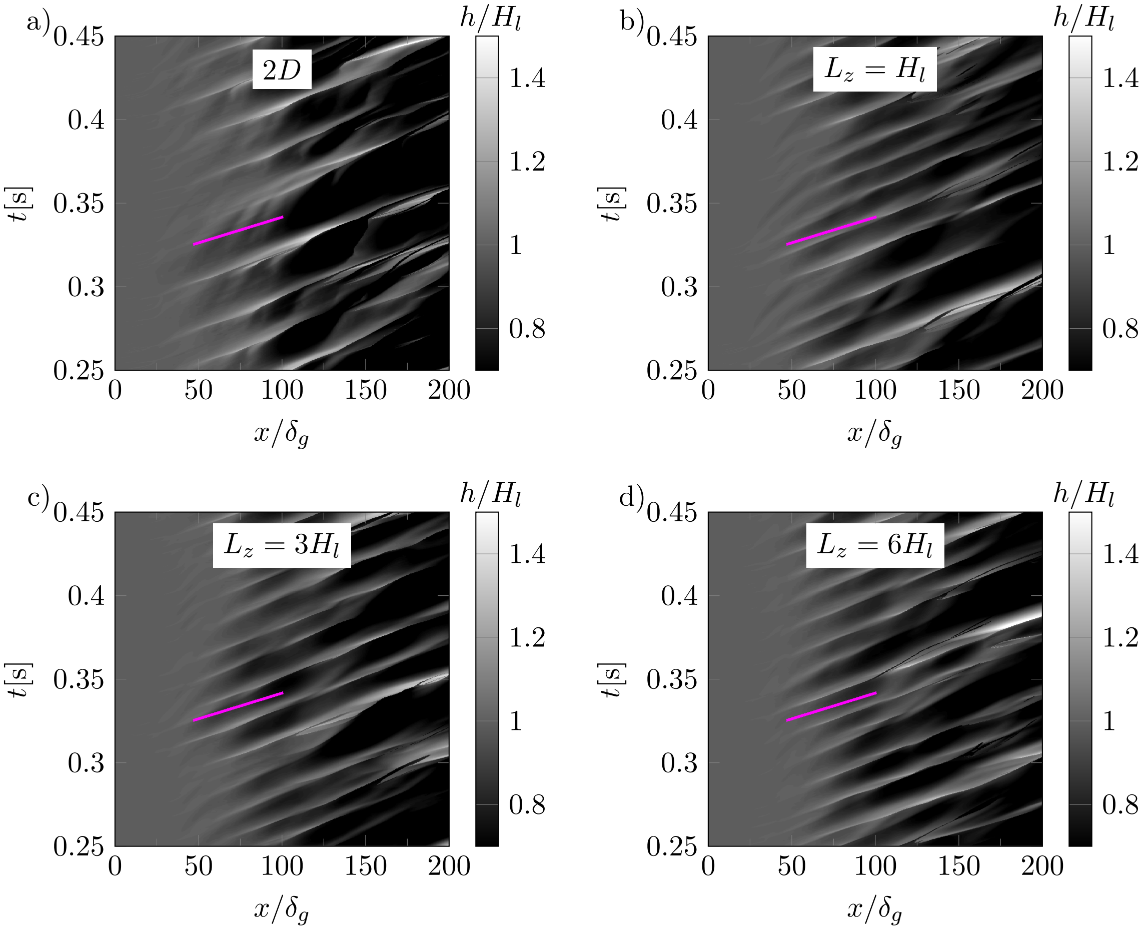

Fig. 3.21 – Spatio-temporal diagrams of interface height for different transverse domain sizes. $B1$ case, $\delta_d = 1$, $n = 2$, $H_g = H_l = 1$ cm. a) 2D simulation, b) $L_z = H_l$, c) $L_z = 3H_l$, d) $L_z = 6H_l$.

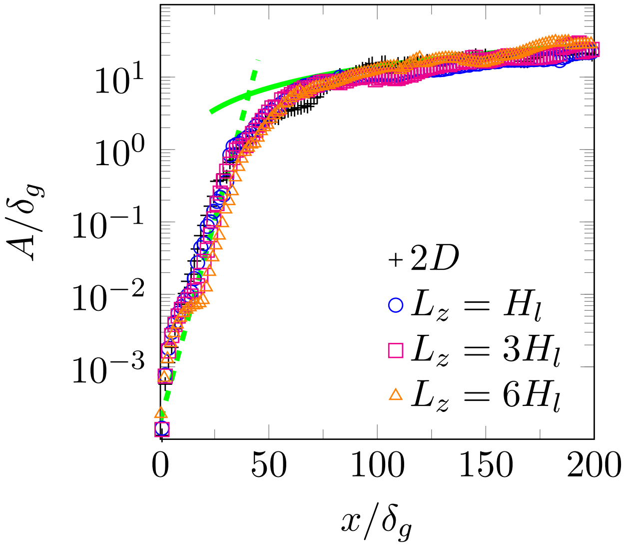

Fig. 3.22 – Evolution of wave amplitude for different transverse domain size. $B1$ case, $\delta_d = 1$, $n = 2$, $H_g = H_l = 1$ cm. ···: Eq. (3.4), with $A_0/\delta_g = 0.00018$ and $k_i = 569.9\mathrm{m}^{-1}$. –: Eq. (3.5), with $C_0 = 0.21$. Only 1 data point every 3 is shown to enhance readability.

which downstream distance the flow is not affected by the 2D nature of the simulation in case of 2D domains, and then to give the minimal transverse domain size that could be used to perform a DNS of primary wave formation, as well as some insights into flow development.

Several methods could be used to average flow quantities. We use here a time and space averaging (along transverse direction). For example, the averaged axial velocity is computed as

$$\langle u(x,y)\rangle_{z,t} = \frac{1}{L_z \Delta T}\int_{\Delta T}\int_{Lz} u(x,y,z)\mathrm{d}t\mathrm{d}z. \tag{3.21}$$

Alternatively, a Favre averaging method may be used, as in Ling et al. (2019).

We firt show the downstream evolution of the averaged interface height y_{int} for all cases of table 3.3 in figure 3.23a). One can see that no significant differences can be observed between 2D and 3D cases before $x/\delta_g = 75$. Beyond this value, the averaged height decreases slower for 3D simulations than in 2D. No differences is seen between 3D cases until $x/\delta_g > 150$, where case $L_z = H_l$ has a higher averaged amplitude. Similar observations can be made from the evolution of the maximum averaged axial velocity with downstream distance, see figure 3.23b).

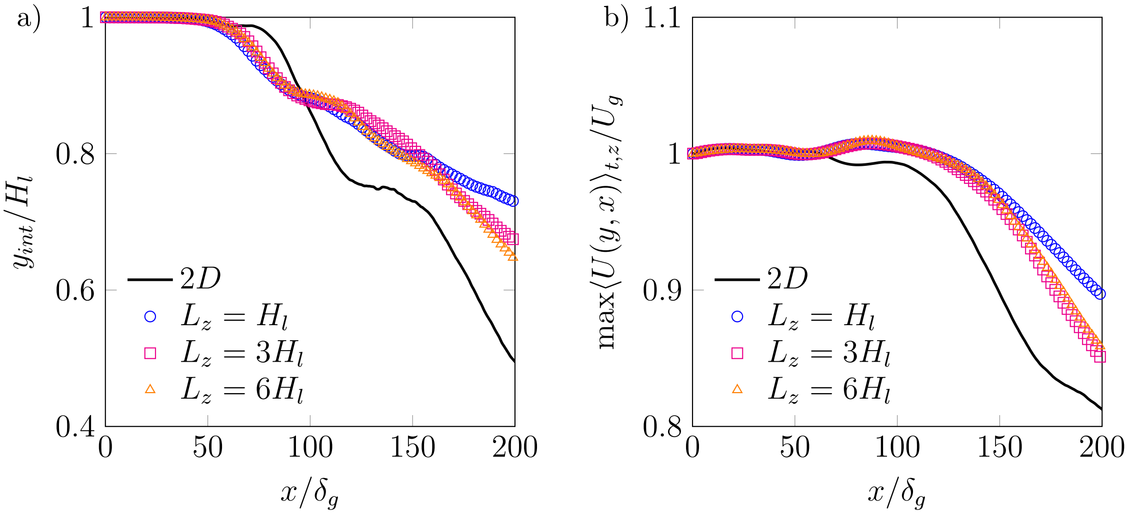

Fig. 3.23 – Evolution of averaged quantities with downstream distance for different domain sizes. a) averaged interface height, b) maximum averaged axial velocity. $B1$ case, $\delta_d = 1$, $n = 2$, $H_g = H_l = 1$ cm.

Then, we show the evolution of the averaged axial velocity profiles with downstream distance for different transverse domain sizes in figure 3.24. One can see that until $x/\delta_g = 80$ no differences is seen between cases. At $x/\delta_g = 80$ a recirculation zone is observed just above mean interface position for all cases. This recirculation is likely to appear in the waves wake. Further downstream, this recirculation is clearly longer to resorb in 2D than in 3D, as seen in figures 3.24c-d). This might be due to the absence of tridimensionalization for vortices generated in the wave wake. Due to the presence of this recirculation, gas jet deviation is higher in 2D than in 3D. The presence of this large recirculation might also be the reason for the smaller y_{int} in 2D than in 3D for $x/\delta_g > 100$. Case $L_z = H_l$ also shows a recirculation slightly longer to resorb than for cases with a wider domain, see figure 3.24c). No significant difference can be seen between $L_z = 3H_l$ and $L_z = 6H_l$.

Finally, we show a comparison of the evolution of $\langle u'u'\rangle_{t,z}$ with downstream distance for different transverse domain sizes in figure 3.25. u' is the deviation of the instantaneous velocity u from the averaged value, i.e., $u' = u - \langle u\rangle_{t,z}$. Note that this kind of averaging does not take into account fluctuations in density, and is strictly valid only for single-phase flows. The differences between the method used here and Favre averaging method will be mainly located in the gas-liquid mixing layer, but Reynolds stresses obtained using both methods have similar orders of magnitude

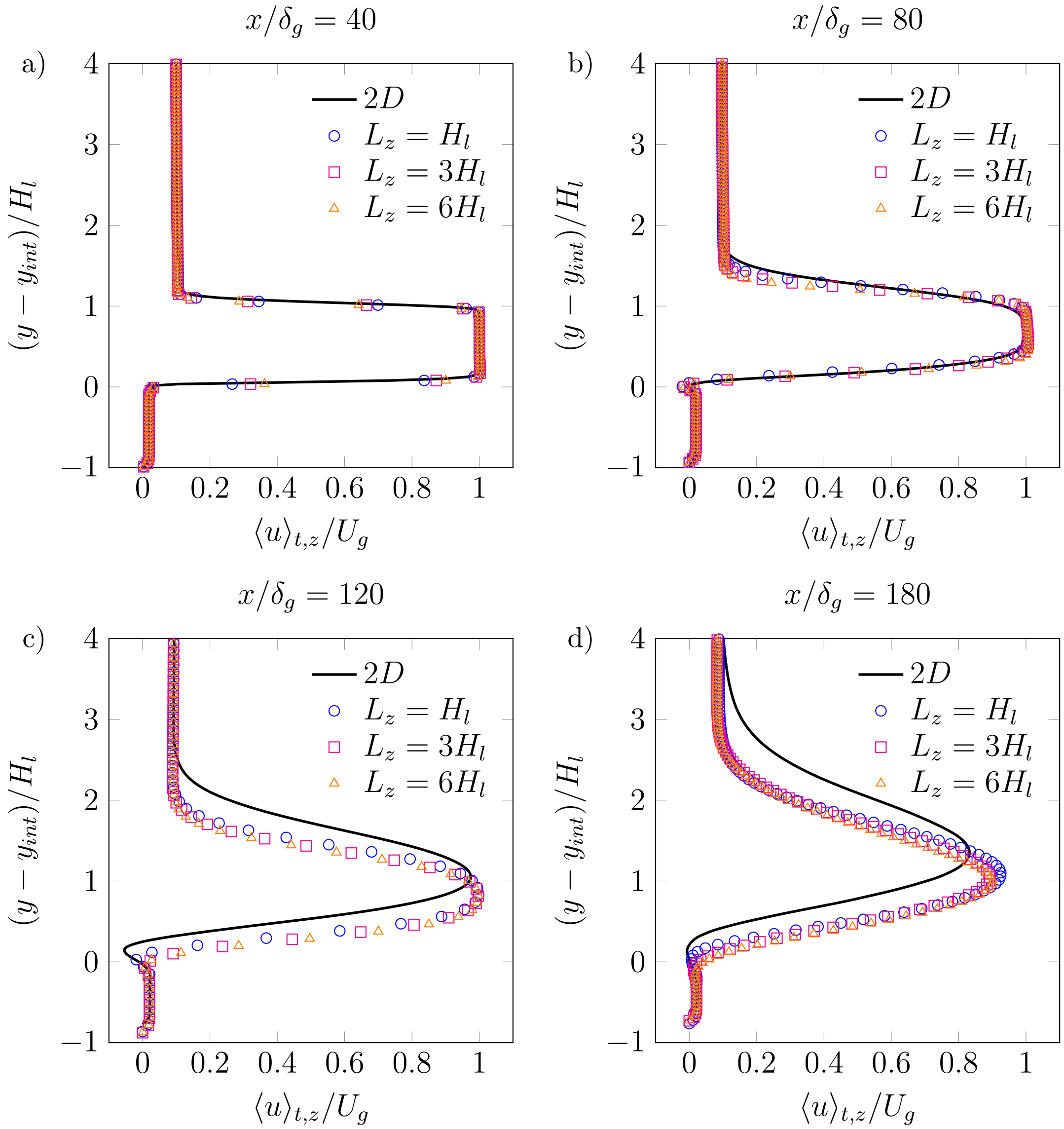

Fig. 3.24 – Evolution of averaged axial velocity profiles for different domain widths with downstream distance. The vertical axis is rescaled by mean interface location at each downstream position. $B1$ case, $\delta_d = 1$, $n = 2$, $H_g = H_l = 1$ cm. a) $x/\delta_g = 40$, b) $x/\delta_g = 80$, c) $x/\delta_g = 120$, d) $x/\delta_g = 180$. In a-b-d) only 1 data point every 2 is shown to enhance readability. In c) only 1 data point every 4 is shown to enhance readability.

(Ling et al., 2019). One can see in figure 3.25 that whatever the downstream position, $\langle u'u' \rangle$ is higher in 2D than in 3D. Beyond $x/\delta_g = 80$, in 2D, $\langle u'u' \rangle_{t,z}$ keeps increasing, which could be a consequence of vortex merging phenomena typical of two-dimensional turbulence. In 3D, beyond $x/\delta_g > 80$, the maximum value of $\langle u'u' \rangle_{t,z}$ does not increase anymore. No significant difference is observed between $L_z = 3H_l$ and $L_z = 6H_l$, except for $x/\delta_g = 40$ (figure 3.25a), where differences might be due to a shorter sampling time for the widest domain. Some slight differences can be noted between these two cases and the case with $L_z = H_l$ in the maxima of $\langle u'u' \rangle_{t,z}$ profiles.

Concerning turbulence rate, one can deduce from figure 3.25a) that, at $x/\delta_g = 40$ and in case of 3D simulations, the maximum level of fluctuations is between 15% and 18%. This value might be affected by the averaging method, but it is at any rate a sufficient turbulence level to induce an increase of frequency. However, this value corresponds to the maximum level of fluctuations close to the average interface position, whereas in Matas et al. (2015) the level of fluctuations is measured in the center of gas channel. In order to understand if these fluctuations could be responsible for the frequency increase observed in 3D simulations, the stability analysis performed in Matas et al. (2015) could be completed with the inclusion of an eddy viscosity profile rather than a constant value across the gas phase.

In this section, we have first shown through visualizations that ligaments generation is triggered by a Rayleigh–Taylor instability induced by wave acceleration. Wave growth and speed are not affected by domain width. However, frequency is different between 2D and 3D cases. This might be due to the turbulence rate in gas phase, but this point deserves further study. The study of averaged quantities shows that there is essentially no differences between $L_z = 3H_l$ and $L_z = 6H_l$. The value $L_z = 3H_l$ could be retained as the minimal domain width needed to perform a DNS of primary wave formation. However, resolving ligaments formation and subsequent atomization process may require a wider domain. The comparison between 2D and 3D domains shows that mean flow statistics start being affected by the 2D nature of the domain when the instability enters its non-linear growth area (beyond $x/\delta_g = 80$ for $n = 2$).

Starting from last conclusion, if one restricts the study to linear growth region, one can study velocity profiles spatial variations with statistics extracted from 2D simulations and for various resolutions. The main observation is that the base flow does not vary between the inlet of the domain and the location at which wave amplitude departs from exponential growth (results not shown). This is in agreement with Fuster et al. (2009).

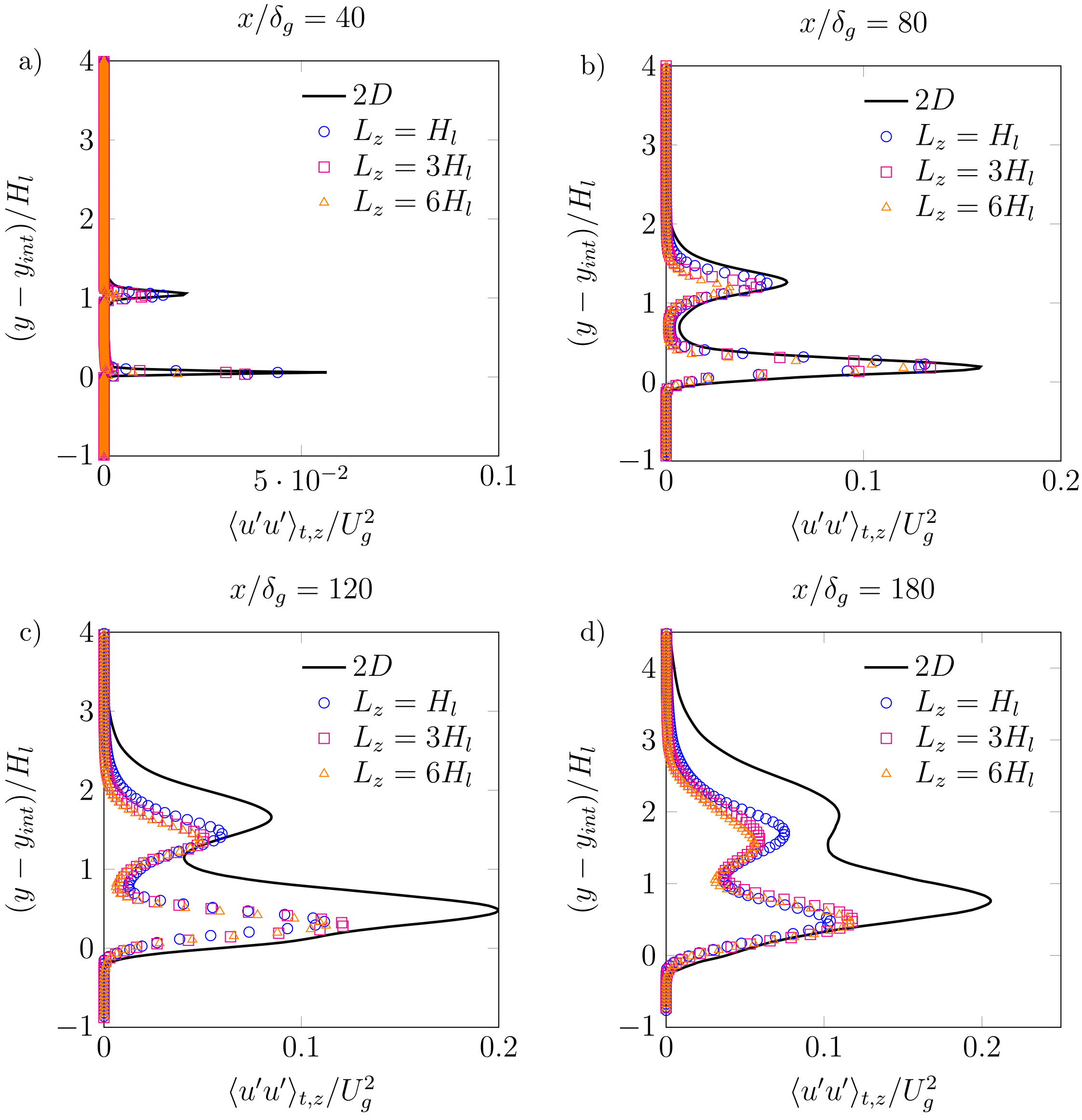

Fig. 3.25 – Evolution of $\langle u'u' \rangle$ profiles for different domain widths with downstream distance. The vertical axis is rescaled by mean interface location at each downstream position. a) $x/\delta_g = 40$, b) $x/\delta_g = 80$, c) $x/\delta_g = 120$, d) $x/\delta_g = 180$. $B1$ case, $\delta_d = 1$, $n = 2$, $H_g = H_l = 1$ cm. In b-c-d) only 1 data point every 2 is shown to enhance readability.

3.6 Conclusion

The confinement of the air-water mixing layer has previously been found to be the missing element allowing to reconcile experimental wave frequencies with viscous linear theory. In this work, we have shown for the first time the convergence between linear theory, experiments, and numerical simulations on the values of the wave frequency, in regimes where the absolute instability is predicted to be due to confinement. We have shown that, in those conditions, waves are self-similar in the downstream area. We proved that the confinement is indeed a mechanism for the transition between convective and absolute regimes. The gas and liquid streams thicknesses are found to have symmetric effects on wave frequency, as first suggested in Matas (2015), but not on wave amplitude. A symmetric confinement and a high dynamic pressure ratio can favour the triggering of an absolute instability, hence enlarging the range of validity of the scaling law given in Eq. (3.6). Finally, it seems that the most amplified frequency scales with the most restrictive confining length, i.e., the thinnest stream, in the absolute regime, which is different from what has been observed on a co-axial configuration.

These conclusions only focus on the transition between convective and confinement-induced absolute regimes. As shown in Otto et al. (2013); Fuster et al. (2013) and Matas et al. (2018), a surface tension-induced absolute regime is dominant as soon as the interfacial wave speed is low enough so that capillary waves are able to send information upstream. This transition is driven by δ_d, the deficit parameter, and *in fine* by the presence of the splitter plate between gas and liquid streams. The configuration we chose to simulate would allow a precise study of the impact of δ_d on the instability and on the flow statistics. This task would be an essential step to understand how the spatial development of the flow affects the instability regime, through the selection of δ_d. However, we have shown that this is a very expensive task, even in two dimensions, that we leave for future work. Our results also suggest that the use of fine meshes in 2D simulations can give rise to some unphysical effects due to two-dimensional turbulence. A 3D mesh convergence would be needed to study spatial frequency variations and to study the global, or not, nature of the instability, but this, again, is an highly expensive task that we leave to future work. The observed switch to low frequency far from the injector seems to appear in 3D as well, but this needs to be confirmed by mesh convergence.

We have then studied the transition between primary and secondary instability. In a first step, simulations of a canonical Rayleigh–Taylor instability and confrontation to linear theory allowed the definition of a minimal resolution for the simulation of such instability. In a second step, we measured wave acceleration in simulations of air-water mixing layers. Despite simplicity of measurement method, we obtained a good agreement between simulations and experiments. We evidenced the scaling of acceleration with liquid injector size, in agreement with the scaling of Eq. (3.6).

We have finally describe the impact of domain width on flow pictures, instability characteristics and mean flow statistics, which does not exist in the literature for the configuration under study. We confirmed that ligaments generation occurs due to a Rayleigh–Taylor instability induced by wave acceleration. We obtained the minimal domain width, $L_z = 3H_l$, that could be used for the DNS of primary wave formation. The observed discrepancy between 2D and 3D simulations for wave frequency value deserves further study. Growth and wave speed are not affected by domain width or two-dimensional nature of simulations.

Chapter 4

Traction open boundary condition for incompressible, turbulent, single- or multi-phase flows, and surface wave simulations

Abstract

The content of this chapter has been published in the *Journal of Computational Physics* (Bozonnet et al., 2021).

4.1 Motivations

This work started as a side project over the course of the present thesis, with the initial aim of reducing cost of simulation of air-water mixing layers by reducing computational domains, as well as improving the accuracy of such simulations. Even though this work is not connected anymore to the other three chapters, it is entirely part of the work done over the course of this thesis.

4.2 Introduction

Due to the finite nature of numerical simulations, it is often necessary to truncate computational domains. This requires imposing artificial boundaries along with the associated mathematical conditions that close the system of equations to be solved.

The primary goal of such boundaries is to restrict the computation to a given region of interest without perturbing the solution inside the domain, thereby limiting cost. In the case of outflow boundaries, the flow should be allowed to leave the computational domain in the most natural way possible without undergoing any perturbations that could propagate upstream and thus pollute the upstream solution. Moreover, complex dynamics may occur at the artificial boundary and the flow may contain regions of both outflow and backflow, i.e., regions of flow reversal where the outlet boundary acts as an inlet, potentially polluting the solution (Blayo and Debreu, 2005).

The definition of an ideal open boundary condition (OBC) for incompressible fluid dynamic simulations is still an unresolved topic, as demonstrated by Sani and Gresho after the "Open boundary condition minisymposium" (Sani and Gresho, 1994), or by other authors in recent reviews (Blayo and Debreu, 2005; Bertoglio et al., 2018). However, one can describe the effect of a non-ideal OBC on a simulation result. In wave-like simulations, the phenomena of wave reflection can create unrealistic flows, instabilities and prevent the flow from reaching a statistical equilibrium over a long computational time (Marchesiello et al., 2001). In turbulent flows, the presence of backflow can cause the system to experience an uncontrolled growth in kinetic energy, which has for example been evidenced in biofluids simulations (Moghadam et al., 2011).

More generally, the choice of OBC can severely influence the size of the computational domain due to the difficulty of finding a condition that does not durably affect the upstream flow, the most famous example being the impact of the outflow position on a cylinder drag and lift coefficients (Persillon and Braza, 1998). Indeed, the incompressibility constraint and the unphysical nature of domain truncations may prevent finding a perfect OBC. However, in this chapter, we endeavor to present a novel boundary treatment that reduces the error induced by outlet position on severely truncated domains and is stable to backflow, in addition to satisfying the incompressibility constraint.

In the next section, the main types of outflow treatments are discussed. The new proposed strategy is then presented. In section 3, the numerical implementations of these boundary conditions are presented in the context of a fractional step method with pressure projection method. Section 4 is devoted to single phase test cases, consisting of the Kovasznay flow for measuring spatial convergence, a time-dependent manufactured solution test for measuring temporal convergence, and a flow past a square and a turbulent plane jet to explore the stability and accuracy of the method. Finally, multiphase test cases are considered in section 5, with the convection of a high density droplet, a turbulent swirling liquid jet, and the transport of surface gravity waves. All of the work presented hereafter is applied to outlet boundary conditions where the flow is expected to be mostly leaving the computational domain, but it can be applied as well on lateral and inlet boundaries.

4.3 Existing methods and present work

Before giving a short review of existing methods we introduce here some useful notations. The computational domain will be refered to as Ω. This domain is bounded by real and artifical (open) boundaries. The firsts ones are denoted $\partial\Omega_d$ and the laters $\partial\Omega_o$. $\partial\Omega$ will refer to both types of boundaries, i.e., $\partial\Omega = \partial\Omega_d \cup \partial\Omega_o$. The vector $\mathbf{n}$ is defined as the unit normal to those boundaries, always oriented toward the exterior of the domain.

Existing methods

Apart from classical Dirichlet and Neumann conditions, one of the most widely used boundary conditions is the convective boundary condition,

$$\frac{\partial \phi}{\partial t} + c\frac{\partial \phi}{\partial n} = 0. \tag{4.1}$$

This equation represents the transport of a quantity ϕ through a boundary of normal $\mathbf{n}$ with a phase speed c, where n is the coordinate in the $\mathbf{n}$ direction. This condition, known as the Sommerfeld equation, or the radiation condition, is in fact an exact absorbing condition, i.e., specification of the incoming characteristic to zero, for a 1D wave equation with a constant wave speed (Blayo and Debreu, 2005). The most famous choice of phase speed comes from the work of Orlanski (Orlanski, 1976): c is computed locally based on known values of ϕ in the vicinity of the boundary. This solution has been shown to result in a phase velocity close to white noise (Durran, 2001). Despite some improvements of Orlanski's method (Raymond and Kuo, 1984), it seems that no satisfying method has emerged to obtain an accurate estimation of the phase velocity without *a priori* knowledge of it (Blayo and Debreu, 2005; Higdon, 1994).

A general mathematical approach to obtain exact absorbing boundary conditions has been derived (Engquist and Majda, 1977). However, to our knowledge, no applications of this method to Navier-Stokes equations have been presented, the closest being recent progress on shallow-water equations (Blayo and Debreu, 2005). It has been applied to a 2D wave equation whose coefficients are then identified using the Navier-Stokes equations (Jin and Braza, 1993). It results in a condition similar to Eq. (4.1) with the phase velocity evaluated as the local speed and the presence of a viscous term on the right hand side. More generally, a whole family of OBCs relies on the method of characteristics (Blayo and Debreu, 2005).

On the other hand, another type of boundary condition can be directly derived from the Navier-Stokes equation in its weak form (Taylor et al., 1985): the traction boundary condition. It consists of applying a condition on the normal stress at the artificial boundary,

$$\overline{\overline{\sigma}} \cdot \mathbf{n} = (-p\mathbf{I} + \mu(\nabla\mathbf{u} + \nabla\mathbf{u}^T)) \cdot \mathbf{n} = \mathbf{t}, \tag{4.2}$$

where $\overline{\overline{\sigma}}$, p, μ and $\mathbf{u}$ are the stress tensor, the pressure, the dynamic viscosity, and the velocity, respectively. $\mathbf{t}$ is a traction vector that must be prescribed. No clear guidelines exist for the choice of this vector. The most widespread choice is $\mathbf{t} = \mathbf{0}$, giving the well-known "traction-free" boundary condition (Liu, 2009; Hasan et al., 2005). The traction $\mathbf{t}$ has also been computed locally and iteratively (Taylor et al., 1985), based on previous runs on longer domains (Sani and Gresho, 1994), or defined analytically with a Stokes solution (Bruneau and Fabrie, 1994).

As stated previously, the presence of backflow at an outlet boundary could lead to an instability due to an uncontrolled growth of kinetic energy. To understand it, the energy balance in the overall computational domain, Ω, can be considered (Dong et al., 2014; Dong, 2014),

$$\begin{aligned}\frac{\partial}{\partial t}\int_\Omega \frac{1}{2}\rho|\mathbf{u}|^2 = &-\int_\Omega \frac{\mu}{2}\|\mathbf{D}(\mathbf{u})\|^2 + \int_\Omega (\rho\mathbf{g} + \mathbf{T}_\sigma)\cdot\mathbf{u} \\ &+ \int_{\partial\Omega_d}\left(\overline{\overline{\sigma}}\cdot\mathbf{n} - \frac{1}{2}\rho|\mathbf{u}|^2\mathbf{n}\right)\cdot\mathbf{u} \\ &+ \int_{\partial\Omega_o}\left(\overline{\overline{\sigma}}\cdot\mathbf{n} - \frac{1}{2}\rho|\mathbf{u}|^2\mathbf{n}\right)\cdot\mathbf{u},\end{aligned} \tag{4.3}$$

Where ρ is the density, $\mathbf{g}$ is the gravity vector, $\mathbf{D}(\mathbf{u})$ is the shear rate tensor and $\mathbf{T}_\sigma$ represents surface tension forces. It results that the rate of change of kinetic energy is controlled by viscous dissipation (exchange with internal energy), gravity (exchange with potential energy), surface tension (exchange with surface energy) and by two surface terms. The first one is expressed on $\partial\Omega_d$, the Dirichlet boundaries, where variables are known. The second surface term is expressed on $\partial\Omega_o$, the outflow boundary, where all variables have to be computed. In case of backflow, the convective part of this term becomes positive and can lead to a global increase of kinetic energy, leading to the instability of the system.

Following Eq. (4.3), one possible backflow treatment is to ensure that the last term is zero, preventing backflow from causing an unstable growth of kinetic energy.

It leads to the following OBC

$$\overline{\overline{\sigma}} \cdot \mathbf{n} = (-p\mathbf{I} + \mu(\nabla \mathbf{u} + \nabla \mathbf{u}^T)) \cdot \mathbf{n} = \frac{\rho}{2} f(\mathbf{u})\mathbf{n}, \tag{4.4}$$

with $f(\mathbf{u})$ chosen so that it cancels the last term of Eq. (4.3) in case of backflow, for example

$$f(\mathbf{u}) = \begin{cases} (\mathbf{u} \cdot \mathbf{n})^2 & \text{if } \mathbf{u} \cdot \mathbf{n} < 0, \\ 0 & \text{otherwise.} \end{cases} \tag{4.5}$$

This condition is similar to the stabilized traction-free condition used for single phase flows (Dong et al., 2014; Dong and Shen, 2015) and for multiphase flows (Dong, 2014; Dong and Wang, 2016). In case of backflow, the normal stress will compensate the normal influx of kinetic energy, whereas it will vanish in case of outflow. Different forms for $f(\mathbf{u})$ along with other types of backflow treatments have been reviewed (Bertoglio et al., 2018).

The traction boundary condition, when used as the stabilized traction-free condition as in Eq. (4.4), requires the flow to be well-developped before reaching the boundary (Taylor et al., 1985). Several methods have already been proposed to combine stability and accuracy even at high Reynolds number, such as the "convective-like" traction boundary condition (Dong, 2015),

$$\overline{\overline{\sigma}} \cdot \mathbf{n} = -\mu D_0 \frac{\partial \mathbf{u}}{\partial t} + \frac{\rho}{2} \Theta(\mathbf{u} \cdot \mathbf{n})((\mathbf{u} \cdot \mathbf{n})\mathbf{u} + |\mathbf{u}|^2 \mathbf{n}), \tag{4.6}$$

where D_0 is computed using a characteristic velocity, and the function $\Theta(x)$ is essentially equal to 1 for negative value of x and 0 otherwise, see Dong (2015) for more details. The value of D_0 is found to have little effect on the overall flow, except on the flow patterns near the outlet boundary. An earlier method developped by Bruneau and Fabrie (Bruneau and Fabrie, 1994) combines a stabilization to backflow and a non-zero traction,

$$\overline{\overline{\sigma}} \cdot \mathbf{n} = \overline{\overline{\sigma}}^{ref} \cdot \mathbf{n} + \frac{\rho}{2} (\mathbf{u} \cdot \mathbf{n})^- (\mathbf{u} - \mathbf{u}^{ref}), \tag{4.7}$$

where the reference values are computed using an analytical solution, or evaluated from known values inside the domain (Bruneau, 2000), and $(\mathbf{u} \cdot \mathbf{n})^- = \max(0, -\mathbf{u} \cdot \mathbf{n})$. Note that this condition leads to a well-posed problem (Bruneau and Fabrie, 1996). It has, to the best of our knowledge, not been applied to projection methods.

Another potential backflow treatment is to simply force all velocities such that $\mathbf{u} \cdot \mathbf{n} < 0$ to zero, thus preventing any influx of kinetic energy. This solution provides energy stability of the system, but we will show in section 4.6 that it can lead to severe inaccuracies in multiphase flows. In Marchesiello et al. (2001), when the phase velocity is computed as $\mathbf{u}\cdot\mathbf{n} < 0$, the use of external data allows to limit the occurence of the backflow instability.

As said in the introduction, the main difficulties encountered by outflow treatments are associated with the proper transmission of perturbations through the artificial boundary, and to the presence of inflow/backflow regions on it. One common way to overcome those issues is to try to dissipate, or damp, the fluctuating energy of the flow before the outlet using artificial zones called sponge layers or nudging layers. Sponge layers consist in the introduction of a dissipative source term in Navier-Stokes equations that becomes stronger when getting closer to the boundary (Clément, 1996). Nudging layers consist of the relaxation of the flow towards prescribed external data (Marchesiello et al., 2001). These solutions are intentionally excluded from our study to focus on the improvements of an accurate OBC.

Finally, most efforts to get non-reflective and accurate boundaries have been focused on convective-like OBCs, often requiring the use of external data that is consistent with the backflow treatment (Marchesiello et al., 2001), whereas traction boundary conditions present an easier way to deal with backflow without the need for external data. As said previously, the stabilized traction-free condition, Eq. (4.4), requires the flow to be well-developped before reaching the boundary (Taylor et al., 1985). Traction boundary conditions have, to our knowledge, never been applied to problems of wave reflections.

Generalized traction boundary condition

We propose a new traction boundary condition, inspired from the Bruneau and Fabrie condition Eq. (4.7), that combines the two following characteristics. Firstly, the flow will not be required to be well-developped at the boundary, which will be achieved by applying a non-zero traction at the boundary. Secondly, this OBC will be stable to influxes of kinetic energy due to backflow, which will be achieved by the inclusion of a stabilization term.

We express the traction at the boundary as

$$(-p\mathbf{I} + \mu(\nabla\mathbf{u} + \nabla\mathbf{u}^T)) \cdot \mathbf{n} = \mathbf{t}^{stab} + \theta\mathbf{t}^{est}. \tag{4.8}$$

$\mathbf{t}^{stab}$ is a numerical treatment to ensure stability to backflow. $\mathbf{t}^{est}$ is an estimation of the traction at the outlet boundary and $\theta = [0;1]$ is an adjustable parameter. The accuracy of the present boundary treatment will depend on the choice of the last two terms.

Following Eq. (4.3), the stabilization term is taken such that it cancels the term responsible for the backflow instability in case of backflow,

$$\mathbf{t}^{stab} = \frac{\rho}{2} f(\mathbf{u})\mathbf{n}, \tag{4.9}$$

with $f(\mathbf{u})$ defined as in Eq. (4.5). Thus, the kinetic energy variation at the open boundary is not equal to zero, as with Eq. (4.4), but depends on the value of $\theta \mathbf{t}^{est}$. The results presented in this chapter show that this novel boundary condition is sufficient to ensure the stability of the system in the presence of backflow at the open boundary. If θ is equal to zero, one can see that we recover the stabilized traction-free condition presented in Dong et al. (2014).

To obtain the best possible traction estimate we introduce here the general idea behind our work. We propose $\mathbf{t}^{est}$, the estimated traction at the boundary, to be considered as a Lagrangian quantity. Its value can therefore be evaluated using an advection equation,

$$\frac{\partial \mathbf{t}^{est}}{\partial t} + \mathbf{u}_{ad} \cdot \nabla \mathbf{t}^{est} = \mathbf{0}, \tag{4.10}$$

where $\mathbf{u}_{ad}$ is an advection velocity that can be computed using an analytical expression, an averaged or a local velocity.

Scope of this work

The previous method to estimate the traction is very general and studying all possible ways to resolve it is beyond the scope of the present chapter. Thus, we restrict our study to a few particular cases. We first assume a one dimensional advection velocity of the estimated traction in the outlet boundary normal direction. Then, we assume a first order explicit temporal resolution of Eq. (4.10) on a cartesian grid. The choice of an explicit resolution is a consequence of the algorithm used to solve the coupling between velocity and pressure, as we detail in the next section. Finally, we use a first order upwind discretization of the spatial term in order to use values inside the computational domain.

The traction estimation is therefore expressed as

$$\mathbf{t}^{est} = \left[\phi \overline{\overline{\sigma}}_{BC-1} \cdot \mathbf{n} + (1-\phi)\, \overline{\overline{\sigma}}_{BC} \cdot \mathbf{n}\right], \tag{4.11}$$

where the notations $BC-1$ and BC refer to the point just before the boundary and the boundary point, respectively. ϕ is an interpolation coefficient computed using numerical parameters and the one dimensional advection velocity. ϕ can be considered as a CFL condition and therefore has here to be kept in the range $[0;1]$ as the advection is only done between the boundary point and its closest neighbour.

The previous choices of resolution for Eq. (4.10) are not suitable in case of discontinuities in the traction field. This latter point is limiting in case of multiphase flows due to the effect of surface tension. The presence of a pressure jump can thus deteriorate the traction estimation and create unphysical velocities, or even stability issues. Therefore, in case of multiphase flows we limit our study to high Weber number. A way to get around that difficulty would be to use, for example, a semi-Lagrangian advection method (Owkes and Desjardins, 2014) for $\mathbf{t}^{est}$. Other aspects may have to be considered, such as the curvature computation in the vicinity of the open boundary, or the density boundary condition. Note that the use of multiphase traction-free condition in phase field method provides a natural way to get around that difficulty as a surface tension term appears in the outlet boundary energy flux (Dong, 2014).

For $\theta = 0$, the generalized traction boundary condition, Eq. (4.8), reduces to

$$(-p\mathbf{I} + \mu(\nabla\mathbf{u} + \nabla\mathbf{u}^T)) \cdot \mathbf{n} = \frac{\rho}{2} f(\mathbf{u})\mathbf{n}, \tag{4.12}$$

which will be refered to as the stabilized traction-free condition (TF) in the following. TF is the same condition as used in Dong et al. (2014). For $\theta = 1$ and $\phi = 1$, Eq. (4.8) reduces to

$$(-p\mathbf{I} + \mu(\nabla\mathbf{u} + \nabla\mathbf{u}^T)) \cdot \mathbf{n} = \frac{\rho}{2} f(\mathbf{u})\mathbf{n} + \overline{\overline{\sigma}}_{BC-1} \cdot \mathbf{n}, \tag{4.13}$$

which will be refered to as the estimated traction boundary condition (ET). This condition ressembles the Bruneau and Fabrie condition, Eq. (4.7). The choice $\phi = 1$ raises the question of the dependence of the accuracy to numerical parameters, as the traction at the point just before the boundary may not always be a good estimation. In the final part of the chapter, we will consider the $\phi \neq 1$ case, where Eq. (4.8) reduces to

$$(-p\mathbf{I} + \mu(\nabla\mathbf{u} + \nabla\mathbf{u}^T)) \cdot \mathbf{n} = \frac{\rho}{2} f(\mathbf{u})\mathbf{n} + \left[\phi\overline{\overline{\sigma}}_{BC-1} \cdot \mathbf{n} + (1-\phi)\,\overline{\overline{\sigma}}_{BC} \cdot \mathbf{n}\right], \tag{4.14}$$

which will be refered to as the convected traction boundary condition (CT). Note that in the previous three boundary conditions $f(\mathbf{u})$ is computed using Eq. (4.5).

In the rest of the chapter we also use classic OBCs, such as the Neumann boundary condition (NM),

$$\frac{\partial \mathbf{u}}{\partial n} = 0, \tag{4.15}$$

or the convective boundary condition (CV),

$$\frac{\partial \mathbf{u}}{\partial t} + c\frac{\partial \mathbf{u}}{\partial n} = 0. \tag{4.16}$$

As mentioned previously the performance of such condition will be strongly linked to the choice of the convective velocity, which will be detailed later.

Finally, the main objectives of the present chapter are, for each of the OBCs under consideration, to give a detailed description of the algorithm allowing to their use in the context of projection methods and VOF/Level Set methods, to demonstrate the importance of bakflow stabilization in single- or multiphase flows, and to demonstrate the stability and accuracy of the non-zero traction methods, such as ET or CT. CT will only be used in the end of the chapter, where the level of accuracy obtained with ET is not satisfactory.

4.4 Mathematical formulation and algorithms

General framework

The main elements of the solver have been described in chapter 2. We remind the reader that momentum conservation equation is solved in the framework of a pressure projection method formed by Eqs. (2.20), (2.22) and (2.23)-(2.24).

At all of these steps, boundary conditions have to be provided: velocity boundary condition after estimation and correction, and pressure boundary condition during projection. At the inflow and on the walls, those steps are straightforward and well documented (Gresho, 1991). For the velocity it simply consists of setting the corresponding values in the velocity vector. As these values will not change during estimation and correction, this step is only necessary after estimation, Eq. (2.20),

$$\mathbf{u}^*_{k+1}\big|_{\partial\Omega_d} = \mathbf{u}_D^{n+1}, \tag{4.17}$$

where $\mathbf{u}_D^{n+1}$ is an imposed velocity value given by the physics, i.e., inflow or walls. The definition of the pressure boundary condition is directly obtained from the application of Eq. (2.23) on those boundaries,

$$\left.\frac{\partial \Phi^{n+1}}{\partial n}\right|_{\partial\Omega_d} = 0. \tag{4.18}$$

The expression of outlet boundary conditions for velocities and pressure at each step of the projection algorithm, resulting in the application of the OBCs presented in section 4.3, is detailed in the next subsections.

Implementation of convective/Neumann OBC

Neumann (NM) and convective (CV) boundary conditions can be directly used to compute outlet velocities at the estimation step. In the CV boundary condition, Eq. (4.16), a wave velocity c has to be prescribed. In the present work, it is going to be taken as the maximal velocity in the plane just before the exit,

$$c = c_{max} = \max(\mathbf{u}^*_{k+1} \cdot \mathbf{n})_{BC-1}, \tag{4.19}$$

or as a theoretical wave speed, if available,

$$c = c_{th}. \tag{4.20}$$

The theoretical expression for the phase velocity will be detailed in the results when used. Except if otherwise stated, the phase velocity will be taken as $c = c_{max}$. What is of interest here is the definition of the pressure boundary condition that will allow to obtain a solution to the Poisson equation, Eq. (2.22). This comes from the integration of Eq. (2.22) over the computational domain:

$$\int_{\partial\Omega} \frac{\Delta t}{\rho^{n+1}} \nabla\Phi^{n+1} \cdot \mathbf{n} \mathrm{d}S = \int_{\partial\Omega} \mathbf{u}^*_{k+1} \cdot \mathbf{n} \mathrm{d}S \tag{4.21}$$

Applying Eq. (4.18) will directly lead to the following pressure outlet boundary condition,

$$\int_{\partial\Omega} \frac{\Delta t}{\rho^{n+1}} \left.\frac{\partial\Phi^{n+1}}{\partial n}\right|_{\partial\Omega_o} \mathrm{d}S = Q_{in} - Q_{out}, \tag{4.22}$$

where Q_{in} and Q_{out} are the inlet and outlet flow rates, respectively. Thus, if inlet and outlet flow rates are forced to be the same (including the clipping of negative velocities, as explained in section 4.3) when considering the application of the velocity OBC and the resolution of the Poisson equation, the pressure outlet boundary condition can simply be a Neumann BC,

$$\left.\frac{\partial\Phi^{n+1}}{\partial n}\right|_{\partial\Omega_o} = 0, \tag{4.23}$$

thus ensuring that the integral on the left hand side of Eq. (4.22) is equal to zero. Finally, as the gradient of pressure on all boundaries is equal to zero, there is no need to correct outlet velocities during the correction step. The overall algorithm is presented in algorithm 1.

Algorithm 1: Algorithm for Neumann and convective OBCs

```
Input: $\mathbf{u}^n$, $p^n$, $\rho^n$ in $\Omega$ and on $\partial\Omega$
Solve Eq. (2.7) using VOF advection $\rightarrow \kappa^{n+1}, \mu^{n+1}$ in $\Omega$
for $k = 0$ to $k_{max} - 1$ do
    Compute $\rho^{n+1}_{k+1}$
    Solve Eq. (2.20) $\rightarrow \mathbf{u}^*_{k+1}$ in $\Omega$
    Apply Eq. (4.17) and Neumann or convective OBC on $\mathbf{u}^*_{k+1}$
    Set all velocities such that $\mathbf{u}^*_{k+1} \cdot \mathbf{n} < 0$ to zero in the outlet section
    Correct outlet flow rate
    Solve Eq. (2.22) with Eq. (4.18) and Eq. (4.23) $\rightarrow \Phi^{n+1}$ in $\Omega$
    Correct velocities Eq. (2.23) and pressure Eq. (2.24) $\rightarrow \mathbf{u}^{n+1}_{k+1}$ and $p^{n+1}_{k+1}$ in $\Omega$
Output: $\mathbf{u}^{n+1}$, $p^{n+1}$, $\rho^{n+1}$ in $\Omega$ and on $\partial\Omega$
```

Implementation of traction-free and estimated traction OBC

The implementation of traction boundary conditions in pressure projection methods has been the subject of many publications in recent years (Poux et al., 2011; Liu, 2009; Dong and Shen, 2015; Guermond et al., 2005). See also Angot and Cheaytou (2012) in the context of vector penalty method and Bänsch (2014) for an extension to curved artificial boundaries. Note furthermore that all algorithms presented herein may be adapted to velocity correction methods starting from the work presented in Poux et al. (2012).

The main difficulty is to ensure the validity of the relation,

$$(-p^{n+1}_{k+1}\mathbf{I} + \mu^{n+1}(\nabla \mathbf{u}^{n+1}_{k+1} + \nabla \mathbf{u}^{n+1}_{k+1}{}^{T})) \cdot \mathbf{n} = \mathbf{t}^{n+1} \tag{4.24}$$

along with the incompressibility constraint at the end of the correction step. The form of the vector $\mathbf{t}^{n+1}$ will depend on the type of traction boundary condition (TF, ET, or CT, see section 4.3) and will be explained below. A first strategy consists in simply setting the pressure increment to zero at the outlet (Liu, 2009), but this strategy is known to limit the order of convergence of the overall method (Guermond et al., 2005). An improvement is found whith an update of the outlet pressure through a rotational pressure correction method (Dong et al., 2014; Dong, 2014; Dong and Shen, 2015). It is known with those methods that the use of a rotational pressure correction will significantly improve the convergence order of the overall algorithm. However, in multiphase flows, there is, to our knowledge, only one example of a rotational pressure-correction (Dong and Wang, 2016), which involves the resolution of a second linear system due to the absence of an analytical solution for the pressure increment. Thus, we choose to employ the method presented in Poux et al. (2011), extended for multiphase flow and non-zero traction.

The method presented in Poux et al. (2011) starts by applying the normal, i.e., perpendicular, projection of the traction boundary condition just after the estimation step, Eq. (2.20), using the available variables, namely p_k^{n+1} and $\mathbf{u}_{k+1}^*$. To simplify the understanding of the method, the coordinate system is taken to be cartesian (x, y, z) with an artificial boundary oriented along x. This first step is then,

$$-p_k^{n+1} + 2\mu^{n+1}\frac{\partial u_{k+1}^*}{\partial x} = t_x^{n+1}, \tag{4.25}$$

where t_x^{n+1} is assumed to be known. The final step will be the application of the traction outlet boundary condition on the new variables $\mathbf{u}_{k+1}^{n+1}$ and p_{k+1}^{n+1},

$$-p_{k+1}^{n+1} + 2\mu^{n+1}\frac{\partial u_{k+1}^{n+1}}{\partial x} = t_x^{n+1}. \tag{4.26}$$

We are then looking for the pressure increment that will ensure the validity of Eq. (4.26) as well as satisfy the incompressibility condition. We first take the incompressibility condition in the cell just before the boundary,

$$\nabla \cdot \mathbf{u}_{k+1}^{n+1} = \frac{\partial u_{k+1}^{n+1}}{\partial x} + \frac{\partial v_{k+1}^{n+1}}{\partial y} + \frac{\partial w_{k+1}^{n+1}}{\partial z} = 0, \tag{4.27}$$

where we express $\partial u_{k+1}^{n+1}/\partial x$ using Eq. (4.25) and Eq. (4.26), and $\partial v_{k+1}^{n+1}/\partial y$ and $\partial w_{k+1}^{n+1}/\partial z$ using Eq. (2.23). It leads to

$$\nabla\cdot\mathbf{u}_{k+1}^{n+1} = \frac{p_{k+1}^{n+1} - p_k^{n+1}}{2\mu^{n+1}} + \nabla\cdot\mathbf{u}_{k+1}^* - \frac{\partial}{\partial y}\left(\frac{\Delta t}{\rho_{k+1}^{n+1}}\frac{\partial}{\partial y}\Phi^{n+1}\right) - \frac{\partial}{\partial z}\left(\frac{\Delta t}{\rho_{k+1}^{n+1}}\frac{\partial}{\partial z}\Phi^{n+1}\right). \tag{4.28}$$

Finally, as the flow is incompressible, the pressure boundary condition is

$$\frac{\partial}{\partial y}\left(\frac{1}{\rho_{k+1}^{n+1}}\frac{\partial}{\partial y}\Phi^{n+1}\right) + \frac{\partial}{\partial z}\left(\frac{1}{\rho_{k+1}^{n+1}}\frac{\partial}{\partial z}\Phi^{n+1}\right) - \frac{1}{2\mu^{n+1}\Delta t}\Phi^{n+1} = \frac{\nabla\cdot\mathbf{u}_{k+1}^*}{\Delta t}, \tag{4.29}$$

which is the pressure boundary condition derived in Poux et al. (2011) adapted to a variable density flow. Previous equations are forming the algorithm used to compute and couple the x-velocity and the pressure at the outflow, and to satisfy exactly the relation Eq. (4.26) along with the incompressibility constraint. Concerning the tangential components of the velocity, the outflow condition is simply a Neumann condition,

$$\frac{\partial v_{k+1}^{*,n+1}}{\partial x} = \frac{\partial w_{k+1}^{*,n+1}}{\partial x} = 0. \tag{4.30}$$

This choice, rather than the use of a constraint on the tangential traction value, is motivated by the well-known fact that a tangential traction-free condition is not compatible with a parallel flow (Leone Jr and Gresho, 1981) and by the fact that several results are reported as better with a Neumann condition on tangential velocities rather than a tangential traction condition, even with non-zero traction (Gresho, 1991).

It should be noted that the pressure boundary condition, Eq. (4.29), is only valid if t_x^{n+1} does not change between the estimation and correction steps. Otherwise, any change will have to be taken into account into the pressure OBC, Eq. (4.29). Thus, the traction t_x^{n+1} can be given depending on the type of open boundary condition. For TF, it is

$$t_x^{n+1} = \frac{\rho^n}{2} f(\mathbf{u}^n), \tag{4.31}$$

and for non-zero traction conditions (ET and CT),

$$t_x^{n+1} = \frac{\rho^n}{2} f(\mathbf{u}^n) + t_x^{est,n+1}. \tag{4.32}$$

The density is taken at the previous time step to be coherent with the choice of the velocity. The backflow stabilization is thus not instantaneous but delayed by one time step. As stated previously, the estimated normal traction is computed using interior values and at the previous iteration to ensure the validity of the pressure boundary condition. For ET,

$$t_x^{est,n+1} = \left(-p + 2\mu\frac{\partial u}{\partial x}\right)_{BC-1}^{n}, \tag{4.33}$$

and for CT,

$$t_x^{est,n+1} = \phi\left(-p + 2\mu\frac{\partial u}{\partial x}\right)_{BC-1}^{n} + (1-\phi)\left(-p + 2\mu\frac{\partial u}{\partial x}\right)_{BC}^{n}, \tag{4.34}$$

with ϕ to be prescribed later. The overall algorithm is presented in algorithm 2.

4.5 Single phase test cases

The improvements obtained using our novel outlet treatment are first illustrated on single phase test cases. The first test case, the Kovasznay flow, allows to see

Algorithm 2: Algorithm for traction OBCs

```
Input: $\mathbf{u}^n$, $p^n$, $\rho^n$ in $\Omega$ and on $\partial\Omega$
Solve Eq. (2.7) using VOF advection $\rightarrow \kappa^{n+1}, \mu^{n+1}$ in $\Omega$
for $k = 0$ to $k_{max} - 1$ do
    Compute $\rho^{n+1}_{k+1}$
    Solve Eq. (2.20) $\rightarrow \mathbf{u}^*_{k+1}$ in $\Omega$
    Apply Eqs. (4.17)-(4.25) and (4.30) on $\mathbf{u}^*_{k+1}$
    Solve Eq. (2.22) with Eq. (4.18) and Eq. (4.29) $\rightarrow \Phi^{n+1}$ in $\Omega$
    Correct velocities Eq. (2.23) and pressure Eq. (2.24) $\rightarrow \mathbf{u}^{n+1}_{k+1}$ and $p^{n+1}_{k+1}$ in $\Omega$
    Apply Eqs. (4.26) and (4.30) on $\mathbf{u}^{n+1}_{k+1}$
Output: $\mathbf{u}^{n+1}$, $p^{n+1}$, $\rho^{n+1}$ in $\Omega$ and on $\partial\Omega$
```

the spatial order of convergence of the overall method, while the second test case, a time-dependent manufactured solution test, allows to study the temporal order of convergence of the present algorithm. The third test case, the flow around a square, shows both qualitative and quantitative improvements thanks to ET. The last case, a turbulent plane jet, shows the stability and accuracy of ET in the presence of a fully turbulent flow.

Kovasznay flow

The Kovasznay flow is a steady state flow used to mimic the flow behind a cylinder (Kovasznay, 1948). This configuration is a 2D domain, periodic along the vertical axis, with an inflow on its left boundary and an OBC on its right. The analytical solution of the Kovasznay flow is given by

$$u = 1 - e^{\lambda x}\cos(2\pi y), \tag{4.35}$$

$$v = \frac{\lambda}{2\pi} e^{\lambda x}\sin(2\pi y), \tag{4.36}$$

$$p = \frac{1}{2}\left(1 - e^{2\lambda x}\right), \tag{4.37}$$

where $\lambda = \frac{Re}{2} - \sqrt{\frac{Re^2}{4} + 4\pi^2}$. We choose here $Re = 1/40$. Thus, this test case can be used to study the effect of the type of OBC and its position on the error level compared to the analytical solution (Dong et al., 2014). The domain is a two-dimensional domain of size $-0.5 \leqslant x \leqslant L_x$ and $-0.5 \leqslant y \leqslant 0.5$, with L_x the position of the OBC. The mesh is uniform and Cartesian with a cell size Δ, with Δ to be

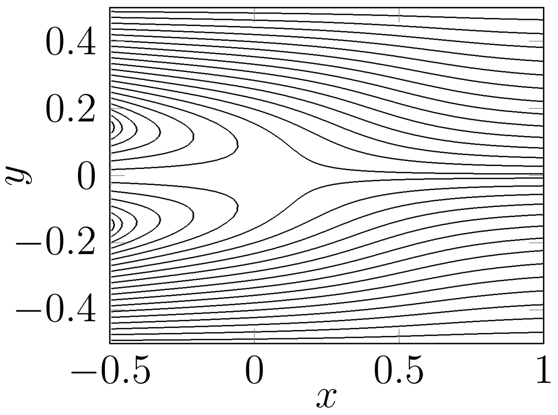

Fig. 4.1 – Streamlines of the Kovasznay flow

specified later. In all cases presented below, $\Delta t = 0.001$. The inflow is defined using the analytical solution in $x = -0.5$. The streamlines of this flow are shown in figure 4.1.

Hereafter we study the effect of the OBC choice on the error compared to the theoretical solution. Considered OBCs are NM, TF and ET. CV is intentionally excluded from this test case to avoid any discussion on the choice of the convective velocity at this point.

In a first comparative test, the domain length is kept constant with $L_x = 4.5$ and the mesh is progressively refined in order to check the convergence of the error depending on the type of OBC. In figure 4.2a) we show the evolution of the L_2 error norm of the x-velocity and the pressure, for differents OBCs and depending on mesh resolution. One can first observe two differents behaviors: for coarser meshes, the same level of error is obtained for all three OBCs, which decreases with mesh resolution (with order 2, i.e., the order of used numerical methods). For finer meshes, and for NM and TF OBCs, the error progressively saturates at a constant value, indicating that outflow error is dominating. Note that this deviation occurs later for TF than for NM and stabilizes also at a lower value, meaning that TF gives a lower error than NM on that test case. On the other hand, with ET, no deviation is observed from the second order slope, meaning that in that range of mesh resolutions, the error due to the outflow is never dominating. With finer meshes and ET, one will necessarily observe a saturation of the error as the choice of the estimated traction is not perfect. Note that one can also compute the estimated traction using the analytical solution (Dong et al., 2014), which is not possible in real flow simulations. For shorter domains, the spatial convergence study gives the same results but the

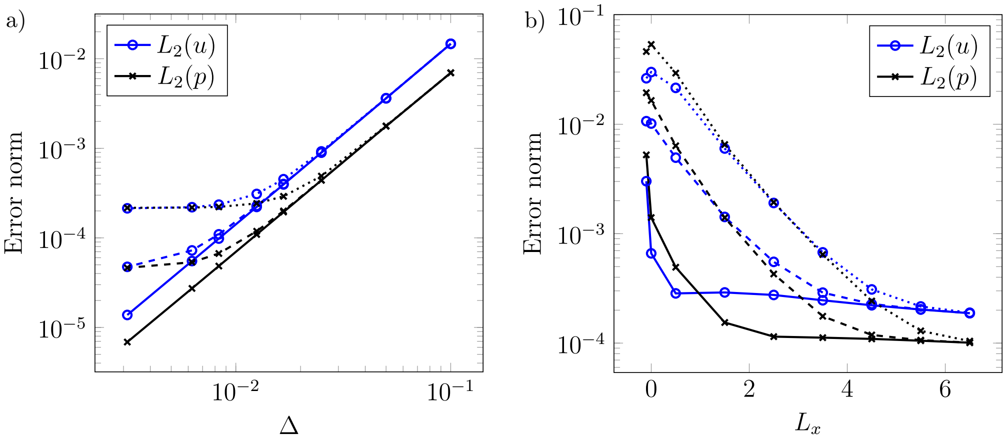

Fig. 4.2 – Error levels for different OBCs: a) Mesh convergence, b) Effect of domain truncation. Continuous line: ET - Dashed line: TF - Dotted line: NM

saturation of the error occurs for coarser meshes. Note that second order convergence is also obtained in L_{inf} error norm.

In a second comparative test, the mesh is kept constant ($\Delta = 1/80$) and the domain is progressively truncated. Similarly to the previous test, we show on figure 4.2b) the evolution of the L_2 error norm of the x-velocity and the pressure, for differents OBCs and depending on the position of the artificial boundary. It is seen in figure 4.2b) that on a sufficiently long domain all OBCs produce the same level of error. It is also seen that with NM the truncation of the domain has a much stronger effect than with other OBCs. The result is, for the range of L_x considered here, barely independent of the artifical boundary position. This point is improved with TF, which provides a better independence of the result with the position of the outlet. With ET the result is independent of L_x for a large range of domain size, even though a small increase of $L_2(u)$ is noticeable. Note that all OBCs are stable for the smallest domain ($L_x = -0.1$), where the outflow boundary is located in a recirculation zone, which is not possible without backflow treatment such as clipping or stabilization. But, in case of the durable presence of a backflow, even the traction condition will not provide a perfectly accurate solution as the stabilization term only makes sense in terms of kinetic energy conservation. Those tests demonstrate the interest of the non-zero traction OBC on a steady state problem in terms of error level and independence to outlet position.

Time-dependent manufactured solution

In order to study the temporal order of convergence of the proposed method, we use the time-dependent manufactured solution of Dong et al. (2014),

$$u = 2\cos(\pi y)\sin(\pi x)\sin(t), \tag{4.38}$$

$$v = -2\cos(\pi x)\sin(\pi y)\sin(t), \tag{4.39}$$

$$p = 2\sin(\pi x)\sin(\pi y)\cos(t), \tag{4.40}$$

which satisfies the incompressibility condition ($\nabla \cdot \mathbf{u} = 0$). In order to satisfy Eq. (2.15), unsteady body forces have to be added to the Navier-Stokes equations.

The computational domain is two-dimensional, of size $0 \leqslant x \leqslant 2$ and $-1 \leqslant y \leqslant 1$, with 256 uniform cells in both directions. Eqs. (4.38) and (4.39) are enforced as Dirichlet boundary conditions on three boundaries of the computational domain, whereas the traction condition Eq. (4.24) is used on the last one. Similarly to Dong et al. (2014); Dong and Wang (2016); Poux et al. (2011), the right hand side of Eq. (4.24) is computed using the manufactured solution. The initial velocity field is set to zero, in agreement with the manufactured solution. For this test case we use $\rho = 1$ and $\mu = 0.01$.

The simulation is advanced in time with a fixed time step, Δt, to be specified, until a fixed final time $t_f = 0.5$. The L_2 error norm on different flow variables at this final time is computed with respect to the manufactured solution. The test is then repeated with various time steps.

The results are shown on figure 4.3. One can see that the error norm convergence for all flow variables is approximately of second order until a progressive saturation of the temporal error by the spatial error. Note that the convergence of the error seems to be faster for the velocities than for the pressure, which may be due to the presence of splitting errors Poux et al. (2011). A rotational pressure correction would be a solution to resolve this discrepancy (Poux et al., 2011; Dong et al., 2014), but for the reason cited in section 9 we chose not to use this strategy. Note that the same results are obtained in L_{inf} error norm. In agreement with Poux et al. (2011), these results suggest that the present algorithm for the implementation of traction conditions does not deteriorate the order of temporal convergence.

Flow around a square

We now compare the different OBCs on an unsteady case: the flow over a two-dimensional square. This test case presents two main interests from the point of

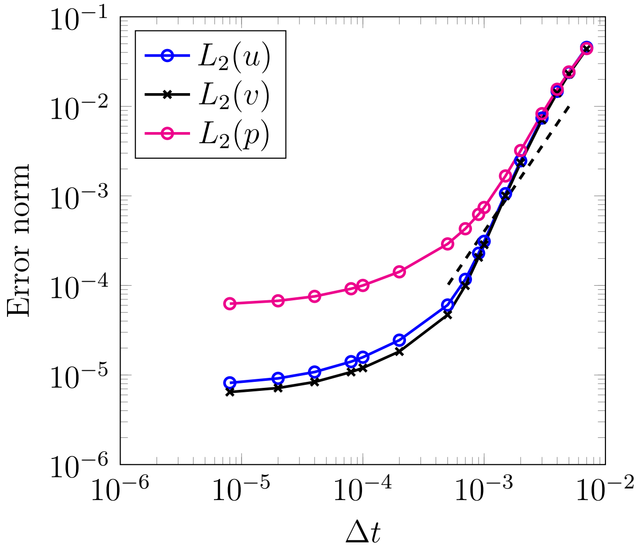

Fig. 4.3 – Method of manufactured solution. Convergence of the error level with respect to the time step. The dashed black line shows second order convergence.

view of OBC performance. Firstly, we study their ability to convect the vortices generated by the von Kármán instability through the artificial boundary. Secondly, we investigate the impact of the OBC position and type on aerodynamic quantities such as drag and lift coefficients and vortex shedding frequency

In a first test, we use the square as a vortex generator and we compare qualitatively TF and ET on their ability to properly convect vortices through the artificial boundary. The test case is a two dimensional domain of size $-5H \leqslant x \leqslant 5H$ and $-5H \leqslant y \leqslant 5H$ where H is the size of the square located in the middle of the domain. The Reynolds number $Re = \rho U H/\mu$ is equal to 1000. U is the velocity uniformely imposed at the inflow ($x = -5H$) and the outflow is located at $x = 5H$. Symmetry boundary conditions are used at $y = \pm 5H$ and the domain is uniformely discretized with a cell size $\Delta = H/40$. The time step is chosen such that the CFL number stays equal to 1. Under those conditions a strongly unsteady flow is generated downstream of the obstacle. It should be noted that this flow is unphysical given the three-dimensionality of a real flow at that Reynolds number, but this test case allows to assess the accuracy of outlet boundary conditions (Dong et al., 2014).

On figure 4.4 we show, through isocontours of z vorticity, the exit of several vortices through the outlet boundary. The top row of figures presents the result with TF, whereas the bottom row of figures presents the result using ET. On the top images, one can observe that the use of TF tends to flatten the vortices on

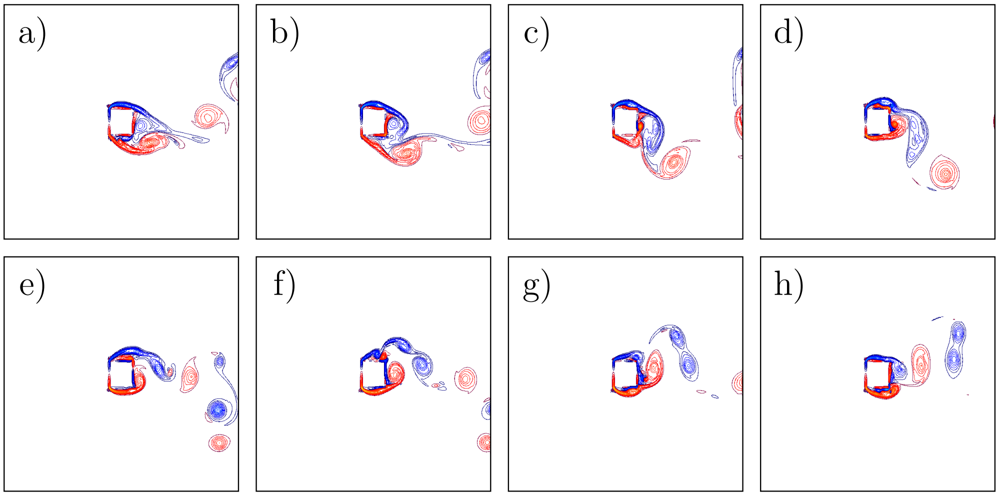

Fig. 4.4 – Isocontours of z vorticity. Top figures: TF; bottom figures: ET. From left to right, all figures are separated by a time interval of $0.5H/U$.

the outlet and to delay their complete exit through the open boundary. This can simply be explained by a balance of pressure: the pressure at the vortex center is balanced by the imposed outlet pressure through imposed traction and by inertial effects. As inertial effects are not strong enough to push out the vortex, it sticks to the boundary and is only slighty – and slowly – pulled out of the domain by the backflow stabilization term. We observed that if no backflow stabilization is taken into account, vortices were gathering on the artificial boundary, finally leading to the blow-up of the simulation due to the backflow instability. Note that, although the vortices exit seems unnatural, once the stabilization term is included the code remains perfectly stable to backflow at the outlet boundary. On the other hand, with ET, no vortex sticking is observed and vortices simply cross the boundary with barely any deformation.

We now propose a more quantitative comparison between different OBCs through the study of the aerodynamic quantities. To avoid any confinement effect and any impact of the inflow position, the domain is this time of size $-10H \leqslant x \leqslant L$ and $-10H \leqslant y \leqslant 10H$, with L the position of the outlet boundary and H the size of the square located at $(0, 0)$. The Reynolds number $Re = \rho UH/\mu$ is now equal to 100. The domain is discretized with a uniform cell size $\Delta = H/40$ in the sub-domain $-10H \leqslant x \leqslant L$ and $-4H \leqslant y \leqslant 4H$, to avoid any loss of resolution of the vortices in the wake of the obstacle, and is then progressively stretched up to the top and bottom boundaries with a constant stretching ratio of 1.05. The time step is chosen

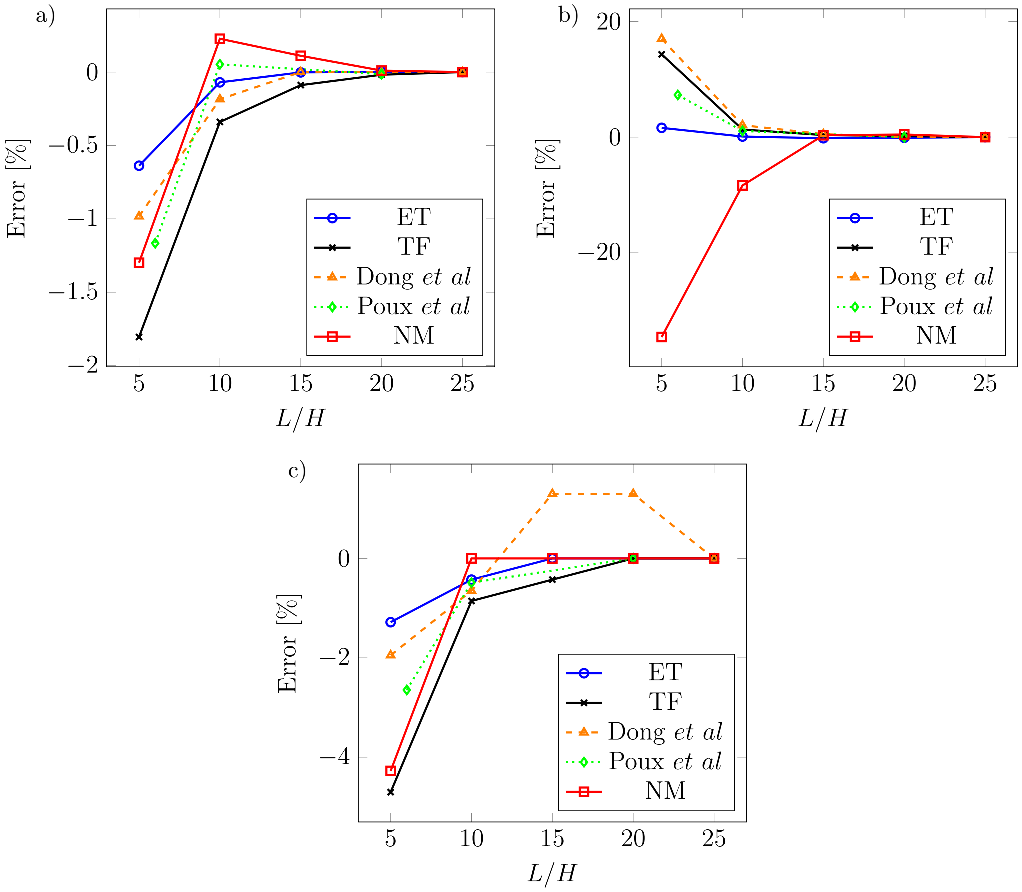

Fig. 4.5 – Impact of the outflow position and type on the aerodynamic quantities: a) mean drag coefficient, b) r.m.s lift coefficient, c) Strouhal number. On all plots, the vertical axis is the error compared to the value obtained on the longest domain, whereas the horizontal axis is the distance between the square and the outflow position L normalized by the size of the square H. The reference results included are the results from Dong et al. (2014) and Poux et al. (2011).

such that the CFL number stays equal to 1. The aerodynamic forces are directly integrated on the surface of the obstacle.

Figure 4.5 presents the evolution of differents aerodynamic quantities as a function of the position and the type of open boundary. We also included the results of two recent publications using the stabilized traction-free condition (Dong et al., 2014) and the traction-free condition (Poux et al., 2011). In order to simplify comparison with other publications, the evolution of the aerodynamic quantities is presented in terms of error relative to the value obtained on the longest domain. Figure 4.5a) shows the evolution of the mean drag coefficient, figure 4.5b) shows the evolution of the r.m.s lift coefficient and figure 4.5c) shows the evolution of the Strouhal number associated with the vortex shedding frequency. The results obtained with ET keep a correct behavior even on the smaller domains by exhibiting the lowest variation of aerodynamic quantities as a function of the outflow position. This improvement is largely explained by the fact that the underlying assumption of well-developped flow associated with the traction-free condition, stabilized or not, is no longer required with ET.

Turbulent plane jet

To finally assess the stability and the accuracy of the proposed boundary condition we study the spatial evolution of a turbulent plane jet. The configuration, the expression of the analytical inlet velocity profile and the choice of parameters are the same as in da Silva and Métais (2002a) (case refered to as “DNS2” in their original paper). The numerical domain is a 3D domain of size $0 \leqslant x \leqslant 12.4h$, $-6h \leqslant y \leqslant 6h$ and $-1.6h \leqslant z \leqslant 1.6h$, where h is the jet width. The inlet boundary is located at $x = 0$ and the outflow at $x = 12.4h$. The other boundaries are periodic. The domain is discretized with a uniform cell size $\Delta x = \Delta y = \Delta z = 0.04h$. The constant time step is $\Delta t = 0.02$.

In a first study the Reynolds number based on the jet width, $Re = (U_i - U_{ff})h/\nu$, is taken equal to 3000, with U_i the jet centerline inlet velocity and U_{ff} the inlet far-field velocity. The isocontours of positive Q-criterion (Dubief and Delcayre, 2000) are shown on figure 4.6, using TF (a) and ET (b). On both figures one can see the spatial development of the jet, initiated by the apparition of successive Kelvin-Helmholtz rolls that are then connected by the apparition of vortices in the streamwise direction. When reaching the outlet boundary the flow is fully tridimensional. On figure 4.6a) one can see the dramatic effect of TF on the exit of the vortices. A part of them sticks to the boundary and is prevented to leave the domain. On the other hand, using ET, no vortex sticking is observed and the vortices are crossing the boundary with barely any deformations, see figure 4.6b). With CV, the vortices exit looks very similar to the one seen using ET (results not shown). Note that using TF we had to reduce the time step size in order to obtain a stable simulation. This may be due to the vortex sticking phenomena coupled to the delayed backflow correction of one time step. Considering the poor qualitative result seen on figure 4.6a) and the need to decrease the time step size, we therefore exclude TF from the following analysis.

The jet exhibits a self-similar behaviour in its downstream region (da Silva and Métais, 2002a). In this region, several quantities computed from the time averaged velocity field are evolving linearly with the downstream distance. We choose here to use the centerline velocity, $U_c = \langle u(x, y = 0)\rangle$, and the jet half-width, $\delta_{1/2}$, defined as the $y-$location where the velocity is equal to half of the centerline velocity, i.e., $\langle u(x, y = \delta_{1/2})\rangle - U_{x,\infty} = 0.5\,(U_c - U_{x,\infty})$, with $U_{x,\infty} = \langle u(x, y = \infty)\rangle$, the far-field velocity. Those quantities follow the following relationships (Gutmark and Wygnanski, 1976):

$$\frac{\delta_{1/2}}{h} = K_{u1}\left[\frac{x}{h} + K_{u2}\right], \tag{4.41}$$

and

$$\left[\frac{U_i - U_{ff}}{U_c - U_{x,\infty}}\right]^2 = C_{u1}\left[\frac{x}{h} + C_{u2}\right]. \tag{4.42}$$

We plot those quantities, along with their linear relations, on figure 4.6c) and 4.6d) using ET and CV. Using ET, in addition to provide a natural exit of the vortices as well as the stability of the simulation, the self-similar region is barely disturbed by the presence of the open boundary. With CV both of the self-similar quantities are strongly affected by the presence of the outflow. Note that the slopes of the linear relations are the same as in da Silva and Métais (2002a).

To demonstrate that the proposed boundary treatment is stable for highly turbulent flows, we study the large eddy simulation of the turbulent plane jet at $Re = 30000$. The sub-grid stresses are estimated with a dynamic Smagorinsky eddy viscosity model using Lagrangian averaging to compute the dynamic coefficient (Meneveau et al., 1996). The computational domain is now larger in the vertical direction to account for the entrainment induced by the jet, i.e., $-8h \leqslant y \leqslant 8h$. The isocontours of positive Q-criterion are shown on figure 4.7a). One can see that there is no accumulation of vortices on the open boundary although the turbulence is fully developped when reaching the open boundary. To show the long-term stability of the proposed method even in the presence of a strong turbulent flow, we show the temporal evolution of the kinetic energy integrated over the computational domain on figure 4.7b). After an initial transient, the flow reaches a statistically stationary state that is not perturbed by the presence of backflow at the open boundary. As stated before, this result strongly suggests that a zero energy flux at the open boundary is not needed to ensure the stability of the simulation. The accuracy of the proposed boundary treatment could even be improved using a better estimation of the traction at the open boundary, for example with CT.

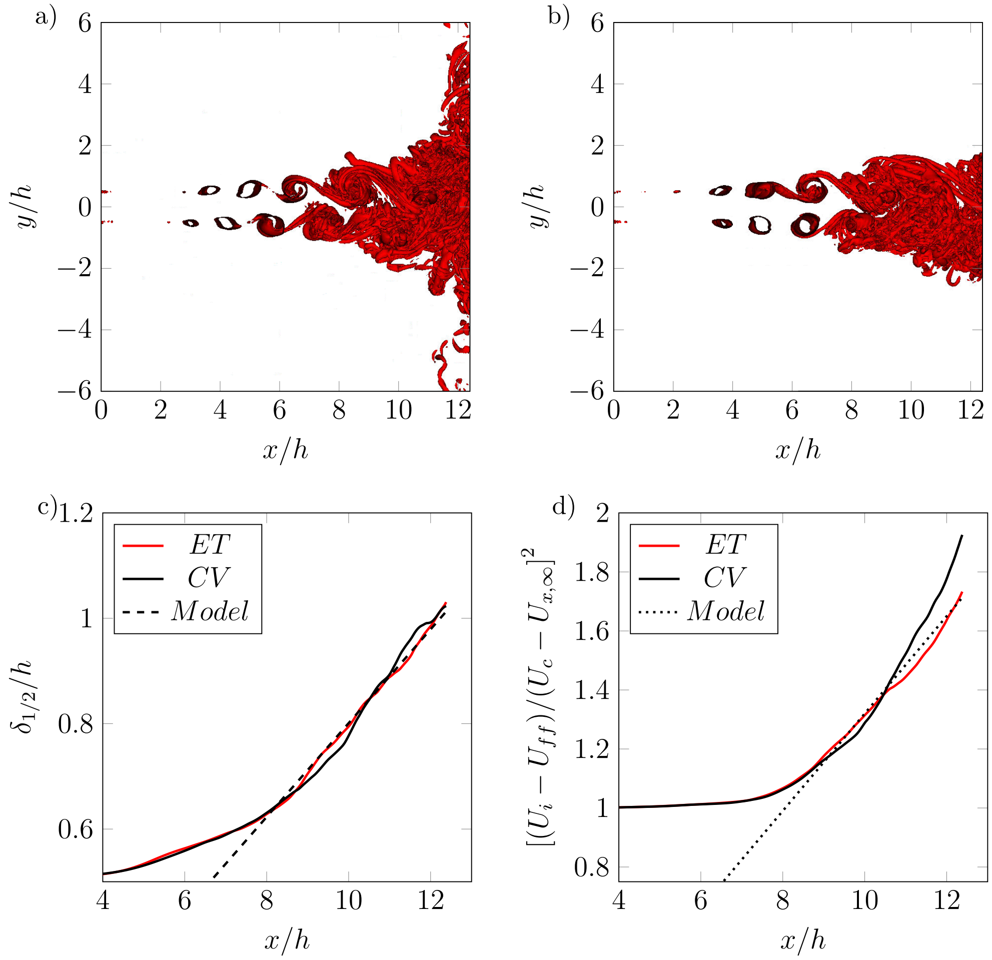

Fig. 4.6 – (Color online) Turbulent plane jet at $Re = 3000$. Positive Q-criterion isocontours (20 isocontours from $Q = 0.25$ to $Q = 100$) at $t(U_i - U_{ff})/h = 166$, using TF (a) and ET (b). c) Evolution of the jet half-width with downstream distance using ET and CV. Model computed using Eq. (4.41) with $K_{u1} = 0.089$ and $K_{u2} = -1$. d) Evolution of the centerline jet velocity with downstream distance using ET and CV. Model computed using Eq. (4.42) with $C_{u1} = 0.165$ and $C_{u2} = -2$.

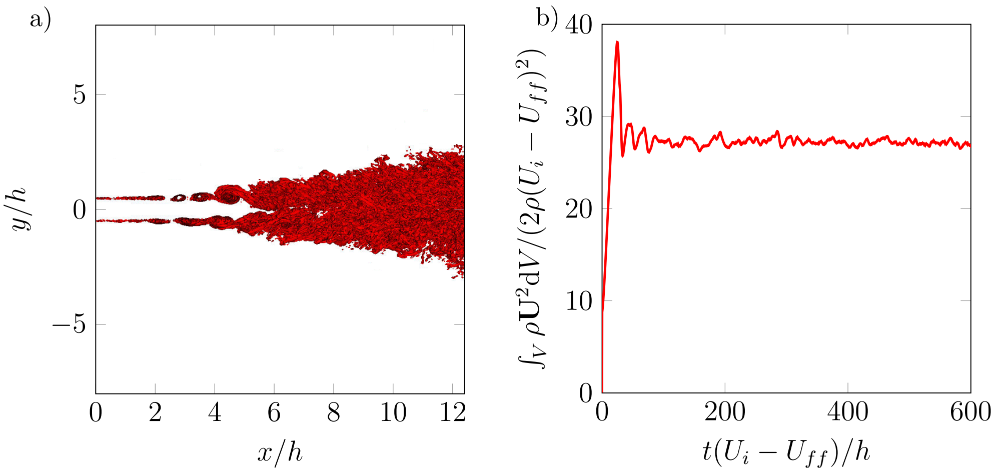

Fig. 4.7 – Large eddy simulation of a turbulent plane jet at $Re = 30000$. a) Positive Q-criterion isocontours (10 isocontours from $Q = 0.25$ to $Q = 100$) at $t(U_i - U_{ff})/h = 400$ using ET. b) Temporal evolution of the normalized kinetic energy integrated over the domain using ET.

4.6 Multiphase test cases

We now turn our attention to multiphase flows. In this section, the importance of backflow stabilization is demonstrated using first a single drop advection test case, then a turbulent swirling jet flow simulation. Finally, we demonstrate the improvements obtained using CT on a problem of surface waves reflection.

Drop convection

A water droplet of size $D = 0.1$ with initial velocity $U_l = 3$ is placed at the center a domain of size $-10D \leqslant x \leqslant 10D$ and $-10D \leqslant y \leqslant 10D$ and surrounded by quiescent air. The outflow is located at $x = 10D$, with periodic boundary conditions at $y = \pm 10D$. At $x = -10D$, a slip wall condition is used. The simulation is run on a 64×64 mesh with a timestep $\Delta t = 0.001$.

Figure 4.8 shows velocity vectors along with the liquid-gas interface during the advection of the drop towards the outlet for two types of boundary conditions. On the top row of images the result are obtain with the CV, and on the bottom row of images the result are obtained with ET. Note that, on this test case, one can replace CV by NM and ET by TF, for the same qualitative result.

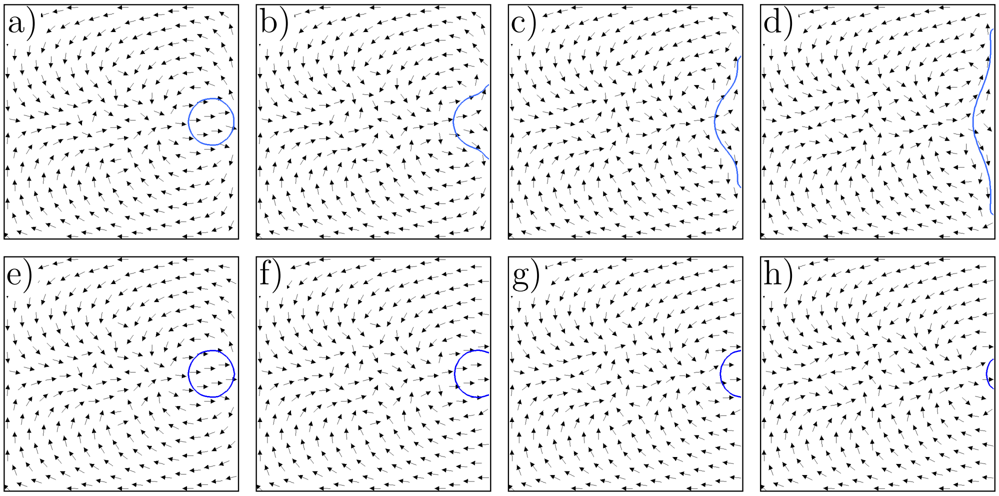

Fig. 4.8 – Water drop advection in a domain without inlet. a)-d) : CV ; e)-h) : ET. From left to right, all figures are separated by a time interval of $0.6D/U_l$.

On the top pictures of figure 4.8, one can observe that with CV OBC the drop is flattening on the boundary and no liquid is exiting the domain. On the other hand, using ET, the drop is completely going out with minimal deformation. The reason for these completely different behaviors lies in the fact that the incompressibility condition requires the outlet flow rate to be equal to the inlet flow rate, in this case zero. Thus, the only way for the drop to exit is to allow backflow. We see here one strong limitation of the clipping strategy, which severely affects the flow by preventing the drop from going out, though it provides unconditional stability. On the other hand, once the stabilization term is included, ET and TF are perfectly stable to backflow as can be seen in figures 4.8f-g-h).

Turbulent swirling jet

To show the importance of backflow stabilization in a more realistic case, we present a simulation of turbulent swirling jet. As shown in figure 4.9, a turbulent liquid jet exits from a nozzle located on the left of the domain. The jet then develops into a conical shape and becomes subject to different interfacial instabilities leading to its atomization. The outflow is located on the right of the domain (colored in pink), whereas all lateral boundary conditions are periodic. All physical properties, injection parameters and geometric characteristics are the same as in Evrard et al. (2019). The domain is discretized with a 200 × 400 × 400 cartesian grid and the

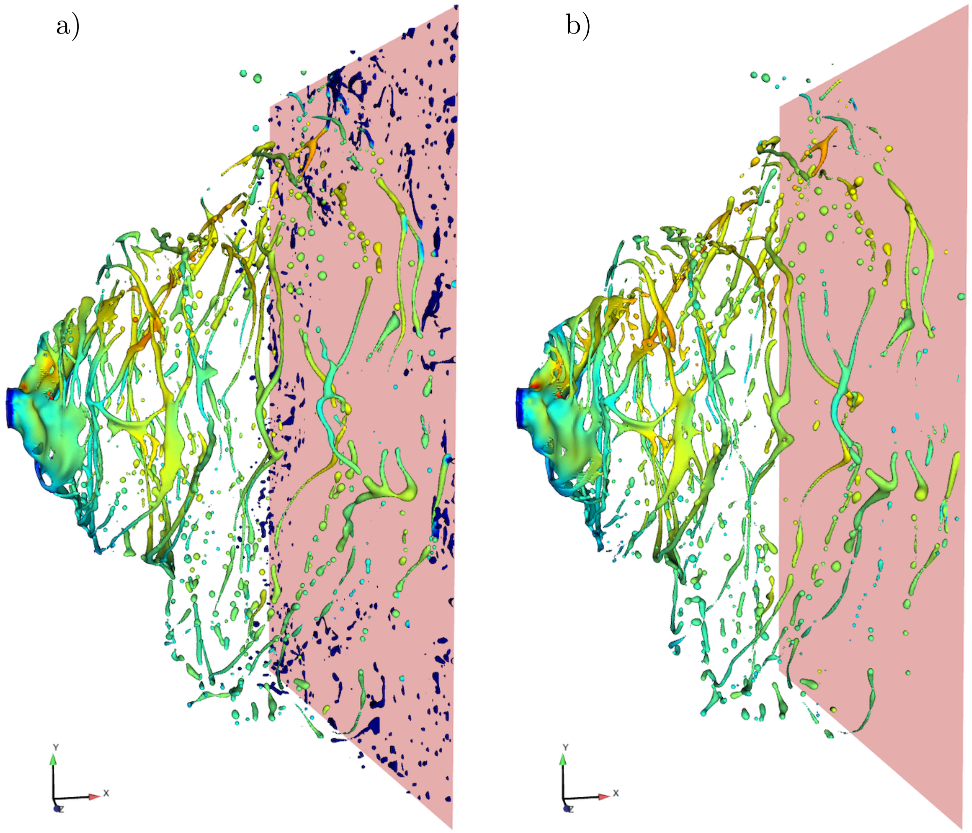

Fig. 4.9 – (Color online) Turbulent swirling jet test case. Liquid-gas interface colored by axial velocity shown at a time $tU/D = 11$ (dark blue: $u = 0$, dark red: $u = 3U$, with U the bulk injection velocity). a) result using CV, b) result using ET.

simulation is advanced with a CFL number of 0.8.

On figures 4.9a) and 4.9b), the liquid-gas interface colored by the axial velocity is shown after a simulation time $tU/D = 11$, where U is the bulk injection velocity, and D the external diameter of the injector. On figure 4.9a), the result with CV is shown, with the phase velocity computed using Eq. (4.19). One can see that since this outflow treatment does not allow backflow, some of the liquid is prevented from going out and “splashes” on the exit plane. Figure 4.9b) shows the result using the ET OBC, and in this case the liquid is not blocked on the exit plane. This obviously has a large impact on the capability to reach long term simulations of such atomizing liquid jets. With a boundary condition that does not allow backflow, the simulation time is obvisouly limited by the length of the domain, which is not the case with a stabilized traction boundary condition. It should be noted here that CV may be replaced by NM and ET by TF for the same results on the liquid exit. The difference between TF and ET will lie in the speed of the droplets in the vicinity of the outlet and in the behavior of the vortices exiting the domain, as already discussed using the test case of the flow around a square.

Although here traction conditions are used only as exit conditions, it should be noted that they may also be used as lateral boundary condition (Dong, 2015; Bruneau and Tancogne, 2018). One can also imagine replacing the wall used around the liquid injector by an open traction boundary condition in order to get a more realistic representation of such jets by allowing the development of a “natural” gas co-flow. We will investigate that point in future works.

Surface gravity waves

We finally evaluate the ability of the different OBCs to evacuate a surface wave without reflection. As said in the introduction, wave reflection is a problem of critical importance in ocean modeling as it prevents the convergence of flow statistics and may create unrealistic flows (Marchesiello et al., 2001).

The test case is set up using solitary wave theory (Munk, 1949). The interface height is defined as

$$\eta(x) = A_0 \mathrm{sech}^2\left(\sqrt{\frac{3A_0}{4{h_0}^3}}x\right), \tag{4.43}$$

with A_0 the initial height of the wave and h_0 the water depth. The initial velocity is defined as $\mathbf{u} = (u(x), 0, 0)$ where

$$u(x) = \eta(x)\frac{\sqrt{|g|\,(h_0 + A_0)}}{h_0 + \eta(x)} + U_{in}, \tag{4.44}$$

and U_{in} is the inflow velocity. The computational domain is two-dimensional, of size $-60h_0 \leqslant x \leqslant 20h_0$ and $-h_0 \leqslant y \leqslant 4h_0$ with symmetry boundary conditions along y, a constant velocity inflow $u = U_{in}$ at $x = -60h_0$ and the OBC at $x = 20h_0$. Air/water conditions are used for the choice of physical properties. This setup results in the transport of a soliton from the position $x = 0$ to the OBC at a constant phase velocity $c_{th} = \sqrt{|g|\,(h_0 + A_0)} + U_{in}$. For all cases presented below parameters are chosen as $A_0 = 0.005$, $h_0 = 0.01$, $U_{in} = 0.07$. The domain is discretized using a uniform Cartesian mesh with $\Delta x = \Delta y = 5 \times 10^{-4}$. The solution is advanced using a time step size $\Delta t = 1 \times 10^{-3}$.

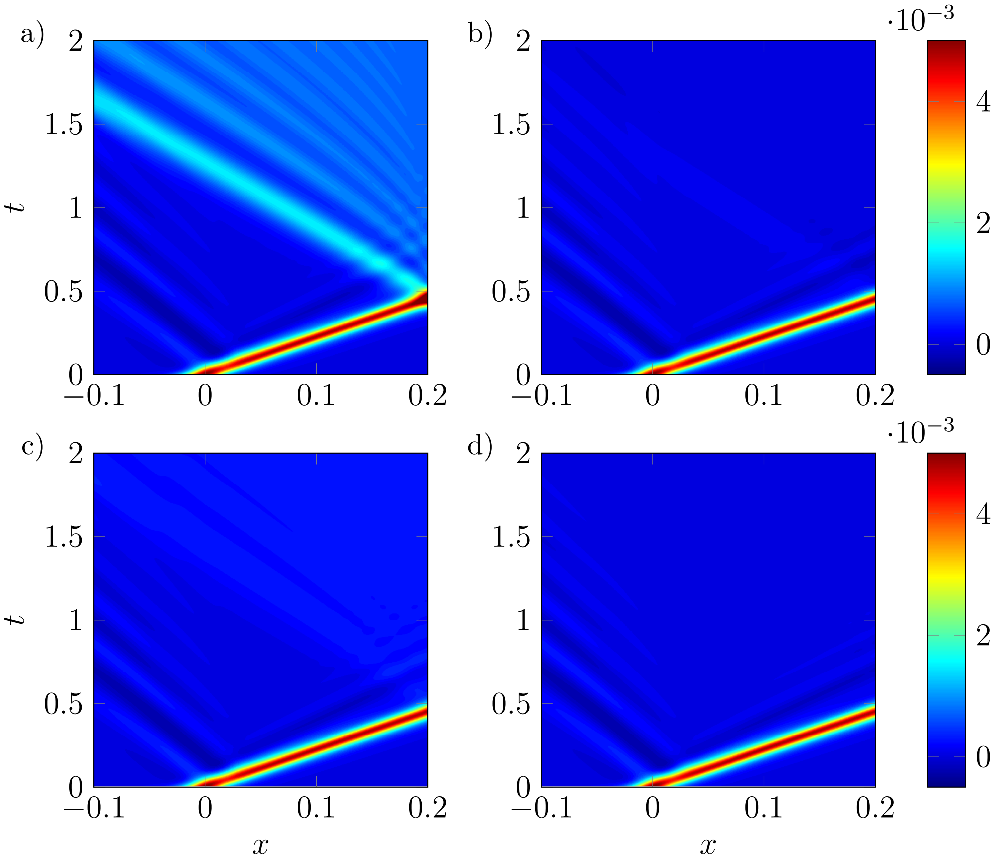

Fig. 4.10 – (Color online) Transport of a surface gravity waves through an OBC. a) CV with $c = c_{max}$, b) ET, c) CV with $c = c_{th}$, d) CT with $c = c_{th}$. The color indicates the liquid height.

On figure 4.10 are presented the space-time plots of the interface height for 4 different OBCs along with, on figure 4.11, the interface height signals at a position $x = 10h_0$. On figure 4.10a), the result with CV is shown. As in previous tests, the wave speed is taken as $c = c_{max}$. One can first see a transient phenomenon at the initialization which causes the emission of perturbations towards the left of the domain and the height of the wave to slightly decrease. Since the inflow is located at $x = -60h_0$, none of the results presented herein are affected by the reflexion of these initial perturbations on the inflow. The reason for these perturbations is an initial adjustment due to the discrete approximations of the continuous solution (Marchesiello et al., 2001). Following this initial transient, the soliton travels towards

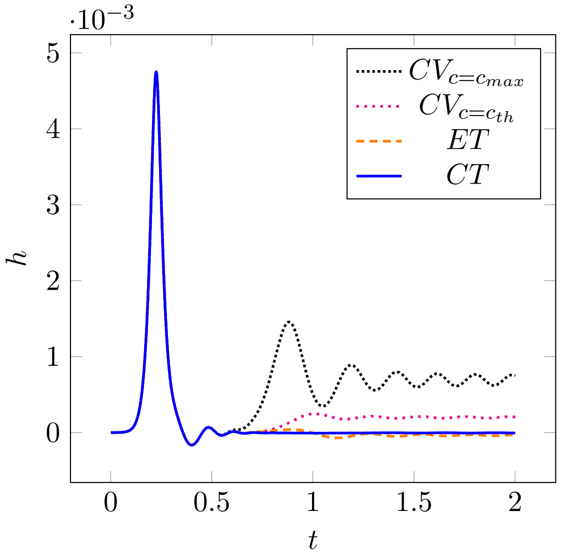

Fig. 4.11 – Interface height signals at a fixed position $x = 10h_0$ for 4 different OBCs.

the OBC at a constant speed c_{th}. Once the wave reaches the artificial boundary, it completely crashes on the boundary and a large part is reflected in the domain in a succession of smaller waves, forming a reflection cone. This result is not a surprise given the inapropriate choice of the convective velocity.

In figure 4.10c), we use the theoretical wave speed as the convective velocity in CV. One can see that the reflection is much lower in amplitude but creates an increase of the mean liquid level, seen also in figure 4.11. Thus, even with the best choice of the wave speed, a convective condition is not able to evacuate a soliton out of the domain without reflection.

We now focus our study on the use of a traction condition. First, it should be noted that the use of TF is impractical for such simulations. The pressure being hydrostatic in the domain, using a traction-free condition will impose a pressure close to zero at the outlet (velocity gradients being small far from the soliton), thus resulting in a strong suction of the flow which rapidly propagates up to the inlet. On figure 4.10b), we show the result using the ET. One can observe that the reflection is almost suppressed but that small waves propagate upstream. Thus, such an arbitrary choice of the estimated traction (computed at the point just before the boundary at the previous time step) is in fact even better than the best choice of a convective OBC. However, two points have to be emphasized. Firstly, ET is not perfectly non-reflective. Secondly, we have observed a dependence of its performance to numerical parameters such as the time step or cell sizes.

The reason for the last two points has in fact already been explained in section 4.3. Considering the estimated traction as a Lagrangian quantity, the present choice is not optimal. Indeed, taking the estimation of the traction at the point before the boundary and at the previous time step is not always a good choice depending on numerical parameters. A more accurate choice can be found considering the convected traction boundary condition (CT). The theoretical wave speed, c_{th}, is taken as the advection velocity. The interpolation coefficient used in Eq. (4.14) is therefore $\phi = c_{th}\Delta t/\Delta x$. The result using this approach is shown on figures 4.10d) and 4.11).

One can see that CT, our new OBC, is now perfectly non-reflective. It must be emphasized that this result is now independent of the time step, the mesh size, and is also independent of the OBC position.

Remark: extension to non-regular grids and domains

In most of the present chapter, we use an estimation of the traction at the point just before the boundary, which is easy to define on a structured mesh. The extension to fully unstructured meshes is possible thanks to the Lagrangian estimation of the traction introduced previously, as done in Eq. (4.14). On such meshes, one has to define an advection velocity and then perform a semi-Lagrangian interpolation of the traction field at the location of interest to obtain the traction estimate. In case of curved boundaries, one has to use differential geometry to complete the pressure boundary condition, Eq. (4.29), as done in Bänsch (2014).

Remark: use as inlet boundary condition

Eq. (4.10) is a general form of traction estimation and does not make any assumption on the sign of $\mathbf{u}_{ad}$. Several choices can be made for $\mathbf{u}_{ad}$: based on a local $CFL = 1$ condition, such as with ET, computed using an analytical expression, such as with the use we made of CT in section 4.6, or using a local velocity.

All of these choices are perfectly suited for the case of an outgoing flow but not to the case of an inflow: if $\mathbf{u}_{ad} \cdot \mathbf{n}$ is positive, traction estimation is made using interior values, whatever the orientation of the flow, if $\mathbf{u}_{ad} \cdot \mathbf{n}$ is negative, traction estimation has to be done using values outside of the domain, which are not known.

For $[\mathbf{u}_{ad} \cdot \mathbf{n} \geq 0; \mathbf{u} \cdot \mathbf{n} \leq 0]$, several cases can be distinguished regarding to the occurence of backflow. In case of local backflow induced by vortices passing through the outlet boundary, no blocking of the flow will be observed and the use of ET and CT will result in accurate and stable simulations, as demonstrated in previous sections. In case of durable backflow, i.e., use as an inlet or a far-field boundary condition, the use of ET or CT will result in unphysical flows, as $\mathbf{t}^{est}$ will keep increasing from one iteration to another, thus pulling the flow outside of the computational domain, eventually blocking the incoming flow (results not shown). In this case, an appropriate solution could be to control the value of $\mathbf{t}^{est}$ over time compared to interior values, in order to ensure that the flow is not over stabilized but is still compatible with the interior flow.

If $\mathbf{u}_{ad} \cdot \mathbf{n} < 0$, whatever the sign of $\mathbf{u} \cdot \mathbf{n}$, $\mathbf{t}^{est}$ has to be computed using external values. This is similar to the need for external data in convective conditions (Marchesiello et al., 2001). One could think that $\mathbf{t}^{est} = \mathbf{0}$ is an appropriate choice as the external traction values are not known, but if one combines this choice with a non-zero traction estimation where the flow is outgoing, some discontinuities in the traction field can occur, leading to unphysical flows and even numerical instabilities (results not shown). The use of TF in cases where the flow is mostly coming from the outside will be appropriate, though with the accuracy issues of TF. If one wants to obtain a flexible solution that would allow durable backflow, as well as the level of accuracy obtained using ET or CT, a strategy to estimate $\mathbf{t}^{est}$ in case of incoming flow has to be defined. One may start from the strategy developped by Bruneau and Creusé (2001) to evaluate incoming characteristics in compressible flows.

4.7 Conclusion

We have presented a comparison between several outlet boundary treatments on single and multiphase test cases along with their numerical implementation in the context of fractional step methods. One major difference between these open boundary conditions lies in the backflow treatment. The implementation of backflow clipping associated with Neumann or convective open boundary conditions, while providing unconditional stability, can have a strong effect in the simulation of multiphase flows. On the other hand, stabilized traction conditions are perfectly suited to resolve this issue. The main drawback of the traction-free condition lies in its underlying assumption of well-developed flow that is not suited for severely truncated domains or high Reynolds number flows. To overcome this issue, an open boundary condition combining stabilization to backflow and space and time varying estimated traction is proposed, allowing stable and accurate simulations for turbulent and multiphase flows. This estimated traction is considered as a Lagrangian quantity, which allows to use it as a non-reflective artifical boundary for surface waves simulations. This work shows that traction conditions have the potential to resolve most of issues related to outflow treatment. They might also be used as lateral or inlet boundary conditions, providing that an appropriate method to estimate the traction is found, and allow a considerable reduction in the cost of numerical simulations. The very general form under which the estimated traction is introduced also opens the way to a study of the effect of different advection methods on the accuracy of traction boundary conditions.

In section 4.2 we explained that convective boundary conditions were limited by their stability to backflow and the difficulty to evaluate a phase velocity. The treatment of these issues still deserve some improvements with traction boundary conditions. In case of backflow, one need to find a way to estimate the traction in a way that will not lower the accuracy of the boundary treatment and is able to sustain long term backflows. For the case of surface waves, traction estimation still requires the use of a phase velocity. No satisfying method exists in the literature to perform such computation, probably because all methods are too local in space and time.

Chapter 5

Conclusion and perspectives

The objectives of this work, initially centered on the stability of an air-water mixing layer, were focused on the role of confinement in primary wave formation. We have demonstrated the convergence between linear stability analysis, simulations, and experiments on instability characteristics in regimes where finite thicknesses of liquid and gas layers are predicted to trigger an absolute instability. We have then proved numerically that confinement is indeed a source of transition between convective and absolute regimes. These two studies definitely demonstrate that injector size selection has an effect on primary wave formation and that further study is needed to ease this choice.

We have thus explored in greater details, through simulations and linear stability analysis, the effect of confinement on flow stability. We have evidenced that in confinement-induced absolute regime wave frequency is inversely proportional to the smallest injector size (liquid or gas), and that both stream thicknesses have a symmetric effect on wave frequency but not on wave amplitude. A reduction of H_l, the liquid stream thickness, induces a global reduction of the amplitude, especially in the self-similar growth region, while a reduction of H_g, the gas stream thickness, seems to induce the departure from this self-similar growth. The range of validity of Eq. (3.6) will be favoured by high dynamic pressure ratio and symmetric confinement.

We lead the first study of wave acceleration, which gave results in agreement with recent drop sizes measurements and with the effect of confinement on primary wave formation.

Finally, we realized 3D simulations of air-water mixing layer. We evidenced that ligaments generation is triggered by wave acceleration, in agreement with the instability cascade described in the first chapter of this manuscript. The study of domain width effect gave the minimal requirement needed, in terms of computational domain size, to perform DNS of primary wave formation.

One natural extension of this work is to pursue the study of velocity deficit effect. This will require the use of locally refined meshes in the vicinity of the interface in order to precisely quantify the effect of δ_d on the instability characteristics, and, particularly, to confirm that its effect on wave frequency is indeed the one predicted by linear stability analysis. However, the use of extremely fine meshes in 2D may give rise to unphysical spatial frequency variation. The study of δ_d effect may have to be done in 3D, which will first require investigation of the observed discrepancy between 2D and 3D simulations for wave frequency value. One may first have to lead a 3D mesh convergence study. 3D mesh convergence will also allow wave acceleration and related quantities (e.g., the wave drag coefficient C_d) measurements.

The configuration we used to study the stability of an air-water mixing layer does not include a splitter plate between gas and liquid streams. In complement to the study of the effect of δ_d on the instability, one could actually verify the relevance of the inclusion of a deficit by performing resolved simulations of splitter plate wake. These simulations would allow the study of contact line dynamic at the splitter plate and the study of mean velocity profiles spatial variation in order to confirm, or not, the picture of figure 1.11. One already knows that splitter plate thickness has an effect on wave frequency selection (Ben Rayana, 2007; Fuster et al., 2013). This effect has been included into linear stability analysis through velocity deficit (Matas et al., 2011; Otto et al., 2013; Fuster et al., 2013), but this choice of modelisation has not been yet confirmed by experiments or numerical simulations. Such study already exists for single phase flows (Laizet et al., 2010), where the spatial evolution of a wake deficit parameter (similar to δ_d), vortex dynamics, and flow statistics are presented for three different splitter plate shapes. Some questions that could be answered are: does a change in injection conditions modify velocity profiles evolution or contact line dynamic? Does the shape of the splitter plate affect velocity profiles evolution or contact line dynamic? Does contact line dynamic affect velocity profiles evolution? This study will however require the use of very refined meshes around splitter plate and, probably, 3D simulations.

Finally, the scaling of Eq. (3.6) does include density ratio. However, density ratio has not been systematically varied in experiments and no stability studies including confinement have been led to study its impact. An important task would be to study precisely how density ratio impacts the borders between different instability regimes. Particularly, in the conditions of Ling et al. (2017, 2019), confinement is not found to have a destabilizing influence. It would be interesting to carry experiments, simulations and linear stability analysis for varying density ratio, in order to assess its influence on flow stability.

Over the course of this thesis we also developed a new traction open boundary condition for incompressible, turbulent, single- or multi-phase flows, and surface wave simulations, with the initial aim of improving accuracy of air-water mixing layers for shorter computational domains. We developed a generalized traction boundary condition that combines backflow stabilization and a Lagrangian traction estimate. This Lagrangian traction estimate has only been used under its most simple forms, but resulting boundary condition allows stable and acurate simulations of turbulent, high-Webernumber multiphase flows, as well as non-reflectivity for gravity wave transport through an open boundary.

A natural extension of the method to low-Weber numbers can be done by improving traction estimation. Resolving the choice of $\mathbf{t}^{est}$ in case of backflow will be a challenging step towards a flexible solution that allows accuracy and stability of boundary treatment for outgoing as well as incoming flows.

Similarly, accurate phase velocity measurement is a very challenging subject. An avenue to explore could be the use of mode decomposition techniques to phase velocity measurements.

Acknowledgements

This work was sponsored by the Office of Naval Research (ONR) as part of the Multidisciplinary University Research Initiatives (MURI) Program, under grant number N00014-16-1-2617, and by the IDEX UGA "International Strategic Partnerships" program. Additional fundings have been obtained thanks to the Fulbright office (Fulbright fellowship) and the French Academy (Jean-Walter Zellidja fellowship). A part of the simulations were performed using HPC resources from GENCI-CINES (Grant No. A0072A00611).

Bibliography

Agbaglah, G., R. Chiodi, and O. Desjardins
2017. Numerical simulation of the initial destabilization of an air-blasted liquid layer. *Journal of Fluid Mechanics*, 812:1024–1038.

Angot, P. and R. Cheaytou
2012. Vector penalty-projection method for incompressible fluid flows with open boundary conditions. In *Proceedings of Algoritmy*, Pp. 219–229.

Aulisa, E., S. Manservisi, R. Scardovelli, and S. Zaleski
2007. Interface reconstruction with least-squares fit and split advection in three-dimensional cartesian geometry. *Journal of Computational Physics*, 225(2):2301–2319.

Bachalo, W.
2000. Spray diagnostics for the twenty-first century. *Atomization and Sprays*, 10(3-5).

Bagué, A., D. Fuster, S. Popinet, R. Scardovelli, and S. Zaleski
2010. Instability growth rate of two-phase mixing layers from a linear eigenvalue problem and an initial-value problem. *Physics of Fluids*, 22(9):092104.

Bänsch, E.
2014. A finite element pressure correction scheme for the Navier-Stokes equations with traction boundary condition. *Computer Methods in Applied Mechanics and Engineering*, 279:198–211.

Ben Rayana, F.
2007. *Contribution à l'étude des instabilités interfaciales liquide-gaz en atomisation assistée et tailles de gouttes.* PhD thesis, Grenoble, INPG.

Bertoglio, C., A. Caiazzo, Y. Bazilevs, M. Braack, M. Esmaily, V. Gravemeier, A. L. Marsden, O. Pironneau, I. E. Vignon-Clementel, and W. A. Wall
2018. Benchmark problems for numerical treatment of backflow at open boundaries. *International Journal for Numerical Methods in Biomedical Engineering*, 34(2):e2918.

Biancofiore, L., F. Gallaire, and R. Pasquetti
2011. Influence of confinement on a two-dimensional wake. *Journal of Fluid Mechanics*, 688:297–320.

Blayo, E. and L. Debreu
2005. Revisiting open boundary conditions from the point of view of characteristic variables. *Ocean Modelling*, 9(3):231–252.

Boeck, T. and S. Zaleski
2005. Viscous versus inviscid instability of two-phase mixing layers with continuous velocity profile. *Physics of Fluids*, 17(3):032106.

Bozonnet, C., O. Desjardins, and G. Balarac
2021. Traction open boundary condition for incompressible, turbulent, single- or multi-phase flows, and surface wave simulations. *Journal of Computational Physics*, 443:110528.

Briggs, R. J.
1964. Electron-stream interaction with plasmas. *MIT press.*

Bruneau, C.-H.
2000. Boundary conditions on artificial frontiers for incompressible and compressible navier-stokes equations. *ESAIM: Mathematical Modelling and Numerical Analysis*, 34(2):303–314.

Bruneau, C.-H. and E. Creusé
2001. Towards a transparent boundary condition for compressible navier–stokes equations. *International Journal for Numerical Methods in Fluids*, 36(7):807–840.

Bruneau, C.-H. and P. Fabrie
1994. Effective downstream boundary conditions for incompressible Navier-Stokes equations. *International Journal for Numerical Methods in Fluids*, 19(8):693–705.

Bruneau, C.-H. and P. Fabrie
1996. New efficient boundary conditions for incompressible navier-stokes equations:

a well-posedness result. *ESAIM: Mathematical Modelling and Numerical Analysis*, 30(7):815–840.

Bruneau, C.-H. and S. Tancogne
2018. Far field boundary conditions for incompressible flows computation. *Journal of Applied Analysis and Computation*, 8(3):690–709.

Chandrasekhar, S.
1961. *Hydrodynamic and hydromagnetic stability.* Dover.

Charru, F.
2012. *Instabilités hydrodynamiques.* EDP Sciences.

Chigier, N. and Z. Farago
1992. Morphological classification of disintegration of round liquid jets in a coaxial air stream. *Atomization and Sprays*, 2(2).

Chiodi, R. and O. Desjardins
2018. Development of a multi-plane interface reconstruction to enable modeling of atomizing flows in volume of fluid simulations. *Bulletin of the American Physical Society*, 63.

Chiodi, R. M. and O. Desjardins
2017. A numerical parametric study on the air-blast atomization of a planar liquid layer. In *55th AIAA Aerospace Sciences Meeting*, P. 1702.

Chomaz, J.-M., P. Huerre, and L. G. Redekopp
1991. A frequency selection criterion in spatially developing flows. *Studies in applied mathematics*, 84(2):119–144.

Chorin, A.
1968. Numerical solution of the navier-stokes equations. *Mathematics of Computation*, 22:745–762.

Clanet, C. and J. C. Lasheras
1999. Transition from dripping to jetting. *Journal of Fluid Mechanics*, 383:307–326.

Clément, A.
1996. Coupling of two absorbing boundary conditions for 2D time-domain simulations of free surface gravity waves. *Journal of Computational Physics*, 126(1):139–151.

Comminal, R., J. Spangenberg, and J. H. Hattel
2015. Cellwise conservative unsplit advection for the volume of fluid method. *Journal of Computational Physics*, 283:582–608.

Cossu, C. and T. Loiseleux
1998. On the convective and absolute nature of instabilities in finite difference numerical simulations of open flows. *Journal of Computational Physics*, 144(1):98–108.

Cummins, S. J., M. M. Francois, and D. B. Kothe
2005. Estimating curvature from volume fractions. *Computers & structures*, 83(6-7):425–434.

da Silva, C. B. and O. Métais
2002a. On the influence of coherent structures upon interscale interactions in turbulent plane jets. *Journal of Fluid Mechanics*, 473:103–145.

da Silva, C. B. and O. Métais
2002b. Vortex control of bifurcating jets: a numerical study. *Physics of fluids*, 14(11):3798–3819.

Dagaut, J., M. Negretti, G. Balarac, and C. Brun
2021. Linear to turbulent görtler instability transition. *Physics of Fluids*, 33(1):014102.

Delon, A.
2016. *Instabilité de flapping: origine et effets sur la structure et le spray d'un jet atomisé*. PhD thesis, Université de Grenoble.

Delon, A., A. Cartellier, and J.-P. Matas
2018. Flapping instability of a liquid jet. *Physical Review Fluids*, 3(4):043901.

Desjardins, O., G. Blanquart, G. Balarac, and H. Pitsch
2008a. High order conservative finite difference scheme for variable density low Mach number turbulent flows. *Journal of Computational Physics*, 227(15):7125–7159.

Desjardins, O., J. McCaslin, M. Owkes, and P. Brady
2013. Direct numerical and large-eddy simulation of primary atomization in complex geometries. *Atomization and Sprays*, 23(11).

Desjardins, O. and V. Moureau
2010. Methods for multiphase flows with high density ratio. *Center for Turbulent Research, Summer Programm*, 2010:313–322.

Desjardins, O., V. Moureau, and H. Pitsch
2008b. An accurate conservative level set/ghost fluid method for simulating turbulent atomization. *Journal of Computational Physics*, 227(18):8395–8416.

Dimotakis, P. E.
1986. Two-dimensional shear-layer entrainment. *AIAA journal*, 24(11):1791–1796.

Dong, S.
2014. An outflow boundary condition and algorithm for incompressible two-phase flows with phase field approach. *Journal of Computational Physics*, 266:47–73.

Dong, S.
2015. A convective-like energy-stable open boundary condition for simulations of incompressible flows. *Journal of Computational Physics*, 302:300–328.

Dong, S., G. E. Karniadakis, and C. Chryssostomidis
2014. A robust and accurate outflow boundary condition for incompressible flow simulations on severely-truncated unbounded domains. *Journal of Computational Physics*, 261:83–105.

Dong, S. and J. Shen
2015. A pressure correction scheme for generalized form of energy-stable open boundary conditions for incompressible flows. *Journal of Computational Physics*, 291:254–278.

Dong, S. and X. Wang
2016. A rotational pressure-correction scheme for incompressible two-phase flows with open boundaries. *PloS one*, 11(5):e0154565.

Drazin, P. G. and W. H. Reid
2004. *Hydrodynamic stability.* Cambridge university press.

Dubief, Y. and F. Delcayre
2000. On coherent-vortex identification in turbulence. *Journal of turbulence*, 1(1):011–011.

Durran, D. R.
2001. Open boundary conditions: fact and fiction. In *IUTAM Symposium on*

Advances in Mathematical Modelling of Atmosphere and Ocean Dynamics, Pp. 1–18. Springer.

Dyadechko, V. and M. Shashkov
2008. Reconstruction of multi-material interfaces from moment data. *Journal of Computational Physics*, 227(11):5361–5384.

Engquist, B. and A. Majda
1977. Absorbing boundary conditions for numerical simulation of waves. *Proceedings of the National Academy of Sciences*, 74(5):1765–1766.

Evrard, F., F. Denner, and B. van Wachem
2019. A multi-scale approach to simulate atomization processes. *International Journal of Multiphase Flow*, 119:194–216.

Francois, M. M., S. J. Cummins, E. D. Dendy, D. B. Kothe, J. M. Sicilian, and M. W. Williams
2006. A balanced-force algorithm for continuous and sharp interfacial surface tension models within a volume tracking framework. *Journal of Computational Physics*, 213(1):141–173.

Fuster, D., A. Bagué, T. Boeck, L. Le Moyne, A. Leboissetier, S. Popinet, P. Ray, R. Scardovelli, and S. Zaleski
2009. Simulation of primary atomization with an octree adaptive mesh refinement and vof method. *International Journal of Multiphase Flow*, 35(6):550–565.

Fuster, D., J.-P. Matas, S. Marty, S. Popinet, J. Hoepffner, A. Cartellier, and S. Zaleski
2013. Instability regimes in the primary breakup region of planar coflowing sheets. *Journal of Fluid Mechanics*, 736:150–176.

Goda, K.
1979. A multistep technique with implicit difference schemes for calculating two or three-dimensional cavity flows. *Journal of Computational Physics*, 30(1):76–95.

Gresho, P. M.
1991. Incompressible fluid dynamics: some fundamental formulation issues. *Annual Review of Fluid Mechanics*, 23(1):413–453.

Guermond, J.-L., P. Minev, and J. Shen
2005. Error analysis of pressure-correction schemes for the time-dependent Stokes

equations with open boundary conditions. *SIAM Journal on Numerical Analysis*, 43(1):239–258.

Gutmark, E. and I. Wygnanski
1976. The planar turbulent jet. *Journal of Fluid Mechanics*, 73(3):465–495.

Harlow, F. H. and J. E. Welch
1965. Numerical calculation of time-dependent viscous incompressible flow of fluid with free surface. *The Physics of Fluids*, 8(12):2182–2189.

Hasan, N., S. F. Anwer, and S. Sanghi
2005. On the outflow boundary condition for external incompressible flows: A new approach. *Journal of computational physics*, 206(2):661–683.

Healey, J.
2007. Enhancing the absolute instability of a boundary layer by adding a far-away plate. *Journal of Fluid Mechanics*, 579:29.

Healey, J.
2009. Destabilizing effects of confinement on homogeneous mixing layers. *Journal of Fluid Mechanics*, 623:241.

Helmholtz, H.
1868. *The London, Edinburgh, and Dublin Philosophical Magazine and Journal of Science*, 36.

Higdon, R. L.
1994. Radiation boundary conditions for dispersive waves. *SIAM Journal on Numerical Analysis*, 31(1):64–100.

Hinch, E. J.
1984. A note on the mechanism of the instability at the interface between two shearing fluids. *Journal of Fluid Mechanics*, 144:463–465.

Hirt, C. W. and B. D. Nichols
1981. Volume of fluid (vof) method for the dynamics of free boundaries. *Journal of computational physics*, 39(1):201–225.

Hoepffner, J., R. Blumenthal, and S. Zaleski
2011. Self-similar wave produced by local perturbation of the kelvin-helmholtz shear-layer instability. *Physical Review Letters*, 106(10):104502.

Hong, M., A. Cartellier, and E. Hopfinger
2003. Atomisation mechanism in coaxial injectors. In *5th Euromech Fluid Mechanics Conference*, Pp. 64–84.

Hooper, A. and W. Boyd
1983. Shear-flow instability at the interface between two viscous fluids. *Journal of Fluid Mechanics*, 128:507–528.

Huerre, P. and P. A. Monkewitz
1990. Local and global instabilities in spatially developing flows. *Annual Review of Fluid Mechanics*, 22(1):473–537.

Ivey, C. B. and P. Moin
2017. Conservative and bounded volume-of-fluid advection on unstructured grids. *Journal of Computational Physics*, 350:387–419.

Jerome, J. J. S., S. Marty, J.-P. Matas, S. Zaleski, and J. Hoepffner
2013. Vortices catapult droplets in atomization. *Physics of Fluids*, 25(11):112109.

Jiang, D. and Y. Ling
2020. Destabilization of a planar liquid stream by a co-flowing turbulent gas stream. *International Journal of Multiphase Flow*, 122:103121.

Jin, G. and M. Braza
1993. A nonreflecting outlet boundary condition for incompressible unsteady Navier-Stokes calculations. *Journal of Computational Physics*, 107(2):239–253.

Juniper, M., O. Tammisola, and F. Lundell
2011. The local and global stability of confined planar wakes at intermediate reynolds number. *Journal of Fluid Mechanics*, 686:218.

Juniper, M. P. and S. M. Candel
2003. The stability of ducted compound flows and consequences for the geometry of coaxial injectors. *Journal of Fluid Mechanics*, 482:257.

Kelvin
1871. Xlvi. hydrokinetic solutions and observations. *The London, Edinburgh, and Dublin Philosophical Magazine and Journal of Science*, 42(281):362–377.

Kovasznay, L.
1948. Laminar flow behind a two-dimensional grid. In *Mathematical Proceedings of the Cambridge Philosophical Society*, volume 44, Pp. 58–62. Cambridge University Press.

Laizet, S., S. Lardeau, and E. Lamballais
2010. Direct numerical simulation of a mixing layer downstream a thick splitter plate. *Physics of Fluids*, 22(1):015104.

Lefebvre, A.
1989. *Atomization and sprays.* Hemisphere Publishing, New York (United States).

Leone Jr, J. M. and P. M. Gresho
1981. Finite element simulations of steady, two-dimensional, viscous incompressible flow over a step. *Journal of computational physics*, 41(1):167–191.

Ling, Y., D. Fuster, G. Tryggvason, and S. Zaleski
2019. A two-phase mixing layer between parallel gas and liquid streams: multiphase turbulence statistics and influence of interfacial instability. *Journal of Fluid Mechanics*, 859:268–307.

Ling, Y., D. Fuster, S. Zaleski, and G. Tryggvason
2017. Spray formation in a quasiplanar gas-liquid mixing layer at moderate density ratios: a numerical closeup. *Physical Review Fluids*, 2(1):014005.

Liu, J.
2009. Open and traction boundary conditions for the incompressible Navier–Stokes equations. *Journal of Computational Physics*, 228(19):7250–7267.

López-Pagés, E., C. Dopazo, and N. Fueyo
2004. Very-near-field dynamics in the injection of two-dimensional gas jets and thin liquid sheets between two parallel high-speed gas streams. *Journal of Fluid Mechanics.*

Lozano, A. and F. Barreras
2001. Experimental study of the gas flow in an air-blasted liquid sheet. *Experiments in fluids*, 31(4):367–376.

Marchesiello, P., J. C. McWilliams, and A. Shchepetkin
2001. Open boundary conditions for long-term integration of regional oceanic models. *Ocean Modelling*, 3(1-2):1–20.

Marmottant, P. and E. Villermaux
2004. On spray formation. *Journal of Fluid Mechanics*, 498:73–111.

Marty, S.
2015. *Contribution to the study of liquid assisted atomization: shear instability and spray generation.* PhD thesis, Grenoble University.

Matas, J.-P.
2015. Inviscid versus viscous instability mechanism of an air–water mixing layer. *Journal of Fluid Mechanics*, 768:375–387.

Matas, J.-P., A. Delon, and A. Cartellier
2018. Shear instability of an axisymmetric air–water coaxial jet. *Journal of Fluid Mechanics*, 843:575–600.

Matas, J.-P., S. Marty, and A. Cartellier
2011. Experimental and analytical study of the shear instability of a gas-liquid mixing layer. *Physics of Fluids*, 23(9):094112.

Matas, J.-P., S. Marty, M. S. Dem, and A. Cartellier
2015. Influence of gas turbulence on the instability of an air-water mixing layer. *Physical Review Letters*, 115(7):074501.

McCaslin, J. O. and O. Desjardins
2014. A localized re-initialization equation for the conservative level set method. *Journal of Computational Physics*, 262:408–426.

Meneveau, C., T. S. Lund, and W. H. Cabot
1996. A lagrangian dynamic subgrid-scale model of turbulence. *Journal of fluid mechanics*, 319:353–385.

Mer, S., O. Praud, H. Neau, N. Merigoux, J. Magnaudet, and V. Roig
2018. The emptying of a bottle as a test case for assessing interfacial momentum exchange models for euler–euler simulations of multi-scale gas-liquid flows. *International Journal of Multiphase Flow*, 106:109–124.

Mirjalili, S., S. S. Jain, and M. Dodd
2017. Interface-capturing methods for two-phase flows: An overview and recent developments. *Center for Turbulence Research Annual Research Briefs*, 2017:117–135.

Moghadam, M. E., Y. Bazilevs, T.-Y. Hsia, I. E. Vignon-Clementel, A. L. Marsden, et al.
2011. A comparison of outlet boundary treatments for prevention of backflow divergence with relevance to blood flow simulations. *Computational Mechanics*, 48(3):277–291.

Monaghan, J. J.
1992. Smoothed particle hydrodynamics. *Annual review of astronomy and astrophysics*, 30(1):543–574.

Monkewitz, P. A.
1988. The absolute and convective nature of instability in two-dimensional wakes at low reynolds numbers. *Physics of Fluids*, 31(5):999–1006.

Mukundan, A. A., T. Ménard, J. C. B. de Motta, and A. Berlemont
2020. A 3d moment of fluid method for simulating complex turbulent multiphase flows. *Computers & Fluids*, 198:104364.

Munk, W. H.
1949. The solitary wave theory and its application to surf problems. *Annals of the New York Academy of Sciences*, 51(3):376–424.

Odier, N., G. Balarac, and C. Corre
2018. Numerical analysis of the flapping mechanism for a two-phase coaxial jet. *International Journal of Multiphase Flow*, 106:164–178.

Odier, N., G. Balarac, C. Corre, and V. Moureau
2015. Numerical study of a flapping liquid sheet sheared by a high-speed stream. *International Journal of Multiphase Flow*, 77:196–208.

Olsson, E. and G. Kreiss
2005. A conservative level set method for two phase flow. *Journal of Computational Physics*, 210(1):225–246.

Orazzo, A. and J. Hoepffner
2012. The evolution of a localized nonlinear wave of the kelvin–helmholtz instability with gravity. *Physics of Fluids*, 24(11):112106.

Orlanski, I.
1976. A simple boundary condition for unbounded hyperbolic flows. *Journal of Computational Physics*, 21(3):251–269.

Osher, S. and J. A. Sethian
1988. Fronts propagating with curvature-dependent speed: Algorithms based on hamilton-jacobi formulations. *Journal of Computational Physics*, 79(1):12–49.

Otto, T., M. Rossi, and T. Boeck
2013. Viscous instability of a sheared liquid-gas interface: Dependence on fluid properties and basic velocity profile. *Physics of Fluids*, 25(3):032103.

Owkes, M., E. Cauble, J. Senecal, and R. A. Currie
2018. Importance of curvature evaluation scale for predictive simulations of dynamic gas–liquid interfaces. *Journal of Computational Physics*, 365:37–55.

Owkes, M. and O. Desjardins
2014. A computational framework for conservative, three-dimensional, unsplit, geometric transport with application to the volume-of-fluid (VOF) method. *Journal of Computational Physics*, 270:587–612.

Pal, S., D. Fuster, and S. Zaleski
2021. A novel momentum-conserving, mass-momentum consistent method for interfacial flows involving large density contrasts. *arXiv preprint arXiv:2101.04142*.

Palmore, J. and O. Desjardins
2019. A volume of fluid framework for interface-resolved simulations of vaporizing liquid-gas flows. *Journal of Computational Physics*, 399:108954.

Patouillet, K.
2020. *Caractérisation d'une surface oxydée de métal fondu: effet de courbure, comportement non-Newtonien et bienfaits de la magnétohydrodynamique*. PhD thesis, Université Grenoble Alpes.

Persillon, H. and M. Braza
1998. Physical analysis of the transition to turbulence in the wake of a circular cylinder by three-dimensional Navier-Stokes simulation. *Journal of Fluid Mechanics*, 365:23–88.

Pilliod Jr, J. E. and E. G. Puckett
2004. Second-order accurate volume-of-fluid algorithms for tracking material interfaces. *Journal of Computational Physics*, 199(2):465–502.

Poo, J. and N. Ashgriz
1989. A computational method for determining curvatures. *Journal of Computational Physics*, 84(2):483–491.

Popinet, S.
2009. An accurate adaptive solver for surface-tension-driven interfacial flows. *Journal of Computational Physics*, 228(16):5838–5866.

Popinet, S.
2018. Numerical models of surface tension. *Annual Review of Fluid Mechanics*, 50:49–75.

Poux, A., S. Glockner, E. Ahusborde, and M. Azaïez
2012. Open boundary conditions for the velocity-correction scheme of the Navier-Stokes equations. *Computers & Fluids*, 70:29–43.

Poux, A., S. Glockner, and M. Azaïez
2011. Improvements on open and traction boundary conditions for Navier-Stokes time-splitting methods. *Journal of Computational Physics*, 230(10):4011–4027.

Puckett, E. G., A. S. Almgren, J. B. Bell, D. L. Marcus, and W. J. Rider
1997. A high-order projection method for tracking fluid interfaces in variable density incompressible flows. *Journal of Computational Physics*, 130(2):269–282.

Rayleigh, L.
1879. On the stability, or instability, of certain fluid motions. *Proc. Lond. Math. Soc.*, 1:57.

Raymond, W. H. and H. Kuo
1984. A radiation boundary condition for multi-dimensional flows. *Quarterly Journal of the Royal Meteorological Society*, 110(464):535–551.

Raynal, L.
1997. *Instabilite et entrainement à l'interface d'une couche de melange liquide-gaz.* PhD thesis, Grenoble University.

Renardy, Y. and M. Renardy
2002. Prost: a parabolic reconstruction of surface tension for the volume-of-fluid method. *Journal of Computational Physics*, 183(2):400–421.

Rider, W. J. and D. B. Kothe
1998. Reconstructing volume tracking. *Journal of Computational physics*, 141(2):112–152.

Rudman, M.
1998. A volume-tracking method for incompressible multifluid flows with large density variations. *International Journal for Numerical Methods in Fluids*, 28(2):357–378.

Sani, R. L. and P. M. Gresho
1994. Resumé and remarks on the open boundary condition minisymposium. *International Journal for Numerical Methods in Fluids*, 18(10):983–1008.

Schmid, P. J.
2007. Nonmodal stability theory. *Annu. Rev. Fluid Mech.*, 39:129–162.

Singh, G., A. Kourmatzis, A. Gutteridge, and A. Masri
2020. Instability growth and fragment formation in air assisted atomization. *Journal of Fluid Mechanics*, 892.

Sussman, M.
2003. A second order coupled level set and volume-of-fluid method for computing growth and collapse of vapor bubbles. *Journal of Computational Physics*, 187(1):110–136.

Taylor, C., J. Rance, and J. Medwell
1985. A note on the imposition of traction boundary conditions when using the FEM for solving incompressible flow problems. *Communications in Applied Numerical Methods*, 1(3):113–121.

Teukolsky, S. A.
2000. Stability of the iterated Crank-Nicholson method in numerical relativity. *Physical Review D*, 61(8):087501.

Thiria, B. and J. Wesfreid
2007. Stability properties of forced wakes. *Journal of Fluid Mechanics*, 579:137.

Tryggvason, G., R. Scardovelli, and S. Zaleski
2011. *Direct numerical simulations of gas–liquid multiphase flows*. Cambridge University Press.

Unverdi, S. O. and G. Tryggvason
1992. A front-tracking method for viscous, incompressible, multi-fluid flows. *Journal of Computational Physics*, 100(1):25–37.

Valluri, P., L. Naraigh, H. Ding, and P. Spelt
2010. Linear and nonlinear spatio-temporal instability in laminar two-layer flows. *Journal of Fluid Mechanics*, 656:458–480.

Varga, C. M., J. C. Lasheras, and E. J. Hopfinger
2003. Initial breakup of a small-diameter liquid jet by a high-speed gas stream. *Journal of Fluid Mechanics*, 497:405–434.

Vaudor, G., T. Ménard, W. Aniszewski, M. Doring, and A. Berlemont
2017. A consistent mass and momentum flux computation method for two phase flows. application to atomization process. *Computers & Fluids*, 152:204–216.

Villermaux, E.
2007. Fragmentation. *Annu. Rev. Fluid Mech.*, 39:419–446.

Villermaux, E.
2020. Fragmentation versus cohesion. *Journal of Fluid Mechanics*, 898.

Villermaux, E. and B. Bossa
2009. Single-drop fragmentation determines size distribution of raindrops. *Nature Physics*, 5(9):697–702.

Welch, P.
1967. The use of fast fourier transform for the estimation of power spectra: a method based on time averaging over short, modified periodograms. *IEEE Transactions on audio and electroacoustics*, 15(2):70–73.

Weymouth, G. D. and D. K.-P. Yue
2010. Conservative volume-of-fluid method for free-surface simulations on cartesian-grids. *Journal of Computational Physics*, 229(8):2853–2865.

Xiao, F., Y. Honma, and T. Kono
2005. A simple algebraic interface capturing scheme using hyperbolic tangent function. *International Journal for Numerical Methods in Fluids*, 48(9):1023–1040.

Yih, C.-S.
1967. Instability due to viscosity stratification. *Journal of Fluid Mechanics*, 27(2):337–352.

Youngs, D. L.
1982. Time-dependent multi-material flow with large fluid distortion. *Numerical Methods for Fluid Dynamics*.

Zandian, A., W. Sirignano, and F. Hussain
2017. Planar liquid jet: Early deformation and atomization cascades. *Physics of Fluids*, 29(6):062109.

Zandian, A., W. Sirignano, and F. Hussain
2019. Vorticity dynamics in a spatially developing liquid jet inside a co-flowing gas. *Journal of Fluid Mechanics*, 877:429–470.

Zhao, H., H. F. Liu, J. L. Xu, and W. F. Li
2011. Experimental study of drop size distribution in the bag breakup regime. *Industrial & engineering chemistry research*, 50(16):9767–9773.

Abstract

The shear instability occuring at the interface between a slow water layer and a fast air stream is a complex phenomenon driven by momentum and viscosity differences across the interface, velocity gradients, as well as by injector geometries. Simulating such an instability in the conditions of experiments is numerically challenging and few studies exist in the literature. This work aims at filling a part of this gap by presenting a study of the convergence between two-dimensional simulations, linear theory, and experiments, in regimes where the instability is triggered by confinement, i.e., the finite thicknesses of the gas and liquid streams. Very good agreement between the three approaches is obtained. Moreover, using simulations and linear theory, we explore in details the effects of confinement on the stability of the flow and on the transition between absolute and convective instability regimes, which is shown to depend on the lengthscale of confinement as well as on dynamic pressure ratio. In the absolute regime under study, interfacial wave frequency is found to be inversely proportional to the smallest injector size (liquid or gas). We then study the transition between primary and secondary instability through wave acceleration. In additional, we explore the impact of three-dimensional effects on the flow. Finally, we present the development of an open boundary condition for turbulent multiphase flows and surface waves simulations. Initially thought as a way to improve accuracy and lower needed computational ressources of air-water mixing layer simulations, this work leads to improvements in the use of traction boundary conditions. Particularly, this novel boundary treatment couples Lagrangian traction estimation to backflow stabilization which provides stability, accuracy and non-reflectivity of artificial boundaries.

Keywords: atomization, shear instability, confinement, open boundary condition

Résumé

L'instabilité de cisaillement se produisant à l'interface entre une couche d'eau lente et un courant d'air rapide est un phénomène complexe induit par des différences de quantité de mouvement et de viscosité à travers l'interface, de forts gradients de vitesse, et par la géométrie des injecteurs. Simuler numériquement une telle instabilité dans les conditions expérimentales est difficile et peu d'études existent dans la littérature. Ce travail a pour objectif de combler une partie de cette lacune en présentant une étude de la convergence entre simulations à deux dimensions, théorie linéaire et expériences, dans des régimes où l'instabilité est déclenchée par le confinement de l'écoulement. Un très bon accord entre les différentes approches est obtenu. De plus, via des simulations et la théorie linaire, nous explorons les effets du confinement sur la stabilité de l'écoulement et sur la transition entre régimes d'instabilité absolus et convectifs. Cette transition est trouvée comme dépendante de la longueur caractéristique du confinement et du ratio de pression dynamique. Dans le régime absolu étudié, la fréquence des vagues interfaciales est trouvée comme étant inversement proportionnelle à la plus petite taille d'injecteur (liquide ou gaz). Nous étudions ensuite la transition entre les instabilités primaires et secondaires à travers l'accélération de la vague. Nous étudions par la suite l'impact des effets tri-dimensionnels sur l'écoulement. Enfin, nous présentons le développement d'une condition de frontière ouverte pour des écoulements turbulents, multiphasiques et des simulations d'ondes de surface. Initialement pensé comme un moyen d'améliorer la précision et de diminuer les ressources informatiques nécessaires aux simulations de couches de mélange eau-air, ce travail mène à des améliorations dans l'utilisation des conditions de traction. Plus particulièrement, cette nouvelle condition aux limites couple une estimation Lagrangienne de la traction à une stabilisation aux écoulements rentrants, ce qui permet la stabilité, la précision et la non-reflectivité des frontières artificielles.

Mots clés: atomisation, instabilité de cisaillement, confinement, condition de frontière ouverte